NOVA SCHOOL OF SCIENCE & TECHNOLOGY

DEPARTMENT OF ELECTRICAL
AND COMPUTER ENGINEERING

FRANCISCO CORREIA DE BERQUÓ FIGUEIRA

Licenciado em Ciências da Engenharia Eletrotécnica e de Computadores

USE OF COMPUTER VISION AND MACHINE LEARNING FOR THE ANALYSIS OF SOLAR ROTATION PROFILE

MASTER IN ELECTRICAL AND COMPUTER ENGINEERING

NOVA University Lisbon
March, 2024

NOVA SCHOOL OF
SCIENCE & TECHNOLOGY

DEPARTMENT OF ELECTRICAL
AND COMPUTER ENGINEERING

USE OF COMPUTER VISION AND MACHINE LEARNING FOR THE ANALYSIS OF SOLAR ROTATION PROFILE

FRANCISCO CORREIA DE BERQUÓ FIGUEIRA

Licenciado em Ciências da Engenharia Eletrotécnica e de Computadores

Adviser: André Teixeira Bento Damas Mora
Assistant Professor, FCT-UNL

Examination Committee

Chair: Luís Augusto Bica Gomes de Oliveira
Associate Professor with Aggregation, FCT-UNL

Rapporteur: Filipe de Carvalho Moutinho
Asssistant Professor, FCT-UNL

Member: André Teixeira Bento Damas Mora
Assistant Professor, FCT-UNL

MASTER IN ELECTRICAL AND COMPUTER ENGINEERING

NOVA University Lisbon
March, 2024

Use of computer vision and machine learning for the analysis of solar rotation profile

This document was created with the (pdf/Xe/Lua)LaTeX processor and the NOVAthesis template (v6.10.18) (Lourenço, 2021).

To my family, friends and all people that supported me throughout this journey.

Acknowledgements

I would like to thank professor André Mora for providing me with this thesis subject as well as his time and support during its development. I would also like to extend my gratitude to the CA3 research group at UNINOVA for their availability to help me in any way.

To NOVA School of Science and Technology (FCT), for the kind memories that were provided while studying here. From new friends to all the achievements made, this place was where I learnt how to believe in myself and become a better person socially and academically.

I want to give a huge thank you to my parents, for believing in me since the day I enrolled in this new adventure that was University. Without your support, I could not have pushed myself so hard through the less good times. I hope I am making you both proud.

A special thank you to my sister Catarina, for providing me such good laughs and fun moments. Thank you for bringing me joy whenever I had a bad day. Even though I could not chose you, luck was on my side when it made me your brother.

To you, Miriam, the person that accompanied me closely during these years. Meeting you at the University was the last thing I expected to happen and for that I am truly grateful. Your love was the thing I never knew I needed to endure the challenges that I was faced with. Thank you for always believing that I was capable to do whatever I wanted to and for encouraging me to do so.

I would like to mention the endless support that I received from my family. To my uncle and aunt, to my cousins, Miguel and Patrícia, Filipe and Ana, thank you for the emotional support and the good times that we shared as a family. To my grandma, your love for me is indeed something I can not describe. To my grandpa, that could not see me finish this big step in my life. I will remember all your efforts to make me a successful person, since I was a little boy. I know you are proud of who I became, this one is for you.

Unfortunately, I can not mention everybody, however this message of gratitude is for all of you that supported me throughout this journey.

"The secret of success is to do the common thing uncommonly well."

— John D. Rockefeller Jr.

Abstract

With the unprecedented growth of solar images provided by recent missions, there is a growing necessity to harness the benefits they may offer. Using images from the Solar Dynamics Observatory (SDO)/Atmospheric Imaging Assembly (AIA) instrument, this project employs state-of-the-art computer vision techniques to study solar differential rotation.

Coronal Bright Points (CBPs), identified as small bright spots in the solar corona, serve as tracers across multiple images due to their distribution across all latitudes, independence from the solar cycle, and distinctiveness compared to other solar activities. Moreover, all CBPs share a similar shape, facilitating their detection and tracking.

In the detection process, an image matching algorithm was employed, proving its reliability across various stages of the solar cycle. In the future, this tool could be improved by integrating Machine Learning, as post-processing method, to eliminate false positive CBP identifications. Computer vision techniques were also utilised to discern whether a CBP is inside or outside a Coronal Hole. Solar rotation values were calculated based on the movements of CBPs during their lifetime as a result of the performed tracking.

Given the importance of this topic, it was created a website to display the information about the solar differential rotation, as well as data on the CBPs and Coronal Holes. This website is supported by a robust database where processed image data is stored, acting as a bridge between the detection and tracking tools and the user interface. This infrastructure enables the presentation of information to the user in near real-time.

This tool's performance results are also showcased, including its outcomes at various stages of the solar cycle. Specifically, these results are highlighted during periods of both low solar activity and high solar activity.

Keywords: Computer vision, Image processing, Match Template, Coronal Bright Points, Solar differential rotation, Solar cycle, Website

Resumo

Com o aumento sem precedentes de imagens solares fornecidas por missões recentes, há uma necessidade crescente de aproveitar os benefícios que elas podem oferecer. Utilizando imagens do instrumento *Solar Dynamics Observatory (SDO)*/*Atmospheric Imaging Assembly (AIA)*, este trabalho empregatécnicas de *Computer Vision* para estudar a rotação diferencial solar, com o objetivo de obter resultados mais precisos.

Os *Coronal Bright Points (CBPs)*, identificados como pequenos pontos brilhantes na coroa solar, servem como pontos de referência nas imagens devido à sua distribuição em todas as latitudes, independência do ciclo solar e distinção em relação a outras actividades solares. Além disso, todos os CBPs partilham uma forma semelhante, facilitando a sua deteção e seguimento.

No processo de deteção dos CBPs, foi utilizado um algoritmo de correspondência de padrões (*Match Template*) em imagens, que mostrou a sua fiabilidade em várias fases do ciclo solar. No futuro, este processo pode ser melhorado integrando *Machine Learning* como um método de eliminação de deteções falsas positivas. Também foram utilizadas técnicas de processamento de imagem para discernir se um CBP está dentro ou fora de um Buraco Coronal. Os valores de rotação solar foram calculados com base nos movimentos de CBPs durante o seu tempo de vida, como resultado do rastreio efectuado.

Dada a importância deste tema, foi criado um *website* para apresentar a informação sobre a rotação diferencial solar, bem como dados sobre os CBPs e os Buracos Coronais. Este site é suportado por uma base de dados onde são armazenados os dados das imagens processadas, servindo de ponte entre as ferramentas de deteção e rastreio e a interface com o utilizador. Esta infraestrutura permite a apresentação da informação ao utilizador quase em tempo real.

São também apresentados os resultados da deteção e do rastreio desta ferramenta, incluindo os seus resultados em várias fases do ciclo solar. Especificamente, estes resultados são destacados durante os períodos de baixa atividade solar e de alta atividade solar.

Palavras-chave: Processamento de imagem, Correspondência de padrões, Coronal Bright Points, Rotação diferencial solar, Ciclo solar, Website

Contents

List of Figures x

List of Tables xii

Acronyms xiii

1 Introduction 1
- 1.1 Motivation . . . 1
- 1.2 Goals . . . 3
- 1.3 Contributions . . . 3
- 1.4 Document Structure . . . 4

2 State of the Art 5
- 2.1 Solar Profile Rotation . . . 5
- 2.2 Satellite and Telescopes Images . . . 6
  - 2.2.1 Telescopes . . . 6
  - 2.2.2 Satellites . . . 7
- 2.3 Sun's Feature Selection . . . 9
  - 2.3.1 Coronal Mass Ejections . . . 9
  - 2.3.2 Solar Prominences and Filaments . . . 10
  - 2.3.3 Sunspots . . . 11
  - 2.3.4 Coronal Bright Points (Coronal Bright Points (CBPs)) . . . 11
- 2.4 Detection Algorithms . . . 13
  - 2.4.1 BP-Finder Algorithm . . . 14
  - 2.4.2 Gradient Path Labelling (GPL) . . . 15
  - 2.4.3 PSO/Snake Hybrid Algorithm . . . 18
- 2.5 Tracking Methods . . . 19
  - 2.5.1 Feature-Based . . . 19
  - 2.5.2 PSO/Snake Algorithm . . . 20
  - 2.5.3 Optical Flow . . . 20
  - 2.5.4 Deep SORT . . . 21
- 2.6 Space Data Websites . . . 22
  - 2.6.1 Space Weather Live . . . 22

2.6.2 Helioviewer 22
2.6.3 Solar Influences Data Analysis Center (SIDC) 23
2.6.4 SPINLab 24
2.7 Final Considerations 24

3 Methods **25**
3.1 Image Dataset 25
3.2 System Overview 27
3.2.1 Image Acquisition 27
3.2.2 Pre-Processing 28
3.2.3 Coronal Holes Mask 30
3.2.4 CBP Detection 31
3.2.5 Solar Rotation Calculations 34
3.2.6 CBP Tracking 35
3.2.7 Database Structure 37
3.2.8 Website Content and Development 37

4 Results Assessment **45**
4.1 Detection Results 45
4.1.1 Template Selection 45
4.1.2 Comparison between Match Template and GPL 49
4.1.3 Results in a solar cycle 52
4.2 Tracking and Solar Rotation Results 52
4.2.1 Tracking results in a solar cycle 52
4.2.2 Solar Rotation profile in a solar cycle 55
4.2.3 Impact of detection results on the tracking process 58
4.2.4 Analysis of the results in a solar cycle 61
4.2.5 Comparison with other works 62

5 Conclusions and Future Work **64**
5.1 Conclusions 64
5.2 Future Work 65

Bibliography **66**

List of Figures

1.1 The structure of the sun 2

2.1 The Sun's differential rotation 6
2.2 Images captured from ground telescopes 7
2.3 Images captured from Satellites that observe the Sun. 9
2.4 Examples of solar prominences and filaments. 10
2.5 Sunspot distribution over the solar cycle. 12
2.6 Full Sun disk image with close up of two CBPs. 12
2.7 Image Segmentation categories and methods. 13
2.8 SOHO/EIT 195 Å image from January 1, 1997. 14
2.9 Full disk SDO/AIA images with the detected CBPs highlighted. 15
2.10 Comparison between the Watershed Transform and the GPL method. 16
2.11 GPL Labelling Process. 17
2.12 GPL final labels result image. 17
2.13 Evolution of the contour using the PSO/Snake Algorithm 19
2.14 Visual example of how the Optical Flow tracking a car in a video. 21
2.15 Solar activity page of the Space Weather Live website. 22
2.16 Screenshot of the Helioviewer website. 23
2.17 Screenshot of the SIDC website. 23
2.18 CBPs tracking page in SPINLab website. 24

3.1 Architecture of the VSO. 26
3.2 Example of a Flexible Image Transport System (FITS) file header 26
3.3 Example of an original image and a FITS image converted to PNG. 27
3.4 Flowchart of the tool's sequential behaviour 28
3.5 Example of an Active Regions mask. 29
3.6 Image intensity normalisation. 30
3.7 Example of a Coronal Holes mask. 31
3.8 Template used for template matching. 32
3.9 CBPs tracking flowchart. 36
3.10 Structure of the Database. 37
3.11 Last image results and scatter plot of the rotational speed over the latitude. 38

3.12 Scatter plot of the location of the CBPs on the solar corona. 39
3.13 Coronal Holes image, lifetime and individual detections histograms. 39
3.14 Date form to chose a time interval and first info table. 41
3.15 Second info table that allows download. 42
3.16 Coronal Holes page previewing the slideshow. 43
3.17 Solar image obtained using the clickable link. 43
3.18 Contents of the *About* page. 44

4.1 Templates used for CBPs detection. 46
4.2 Results of the different templates in a high solar activity image. 47
4.3 Results of the different templates in a low solar activity image. 48
4.4 Comparison between GPL and Match Template in a 2023 image. 50
4.5 Comparison between GPL and Match Template in a 2019 image. 51
4.6 Total individual identifications location on the Suns corona. 52
4.7 Initial and final location of tracked CBPs on the Suns corona, in 2019. 53
4.8 Lifetime histogram of the tracked CBPs, in 2019. 54
4.9 Initial and final location of tracked CBPs on the Suns corona, in 2023. 54
4.10 Lifetime histogram of the tracked CBPs, in 2023. 55
4.11 Scatter plot depicting the correlation between rotational speed and the sine of latitude for 2019 CBPs. 56
4.12 Scatter plot illustrating the association between rotational speed and latitude for 2019 CBPs, complemented by the best-fitting curve. 56
4.13 Scatter plot illustrating the relationship between rotation speed and the sine of latitude for 2023 CBPs. 57
4.14 Scatter plot depicting the relationship between rotation speed and latitude for 2023 CBPs, accompanied by the best-fitting curve. 58
4.15 Colour-coded plot illustrating the correlation between individual detection count and the relationship between rotation speed and latitude. 59
4.16 Colour coded scatter plot illustrating the position of the tracked CBPs in one image, based on their speed. 60
4.17 Colour coded scatter plot illustrating the position of the tracked CBPs in one image, based on their speed and number of detections. 60
4.18 Comparison of solar rotation profiles between 2019 and 2023 by the representation of the best-fitting curves. 61
4.19 Comparison of the best-fitting curves of this and previous works. 63

List of Tables

3.1 Comparison of the different thresholds performances on CBPs detection. . . 33

4.1 Average detection time and individual detections: Match Template vs. GPL 49
4.2 Results of this work's fitting parameters in comparison to other authors' works. 62

Acronyms

AIA	Atmospheric Imaging Assembly *(pp. vi, vii, 8, 9, 12, 15, 23, 24, 26, 27, 64)*
BBSO	Big Bear Solar Observatory *(pp. 6, 7, 67)*
CBP	Coronal Bright Point *(pp. vi–viii, xi, 2, 3, 9, 11–15, 18–20, 22, 24, 27–41, 45, 46, 49–62, 64, 65)*
CC	Cross Correlation *(pp. 31, 32)*
CCOEFF	Mean Shifted Cross Correlation *(pp. 31, 32)*
CMD	Central Meridian Distance *(p. 34)*
CME	Coronal Mass Ejection *(pp. 9–11, 22)*
DKIST	Daniel K. Inouye Solar Telescope *(p. 7)*
EIT	Extreme ultraviolet Imaging Telescope *(pp. 8, 9, 14)*
ESA	European Space Agency *(pp. 8, 9, 67)*
EUV	Extreme Ultraviolet *(pp. xiii, 3, 8, 11, 12, 14, 64)*
EVE	EUV Variability Experiment *(p. 8)*
FCT	NOVA School of Science and Technology *(p. iv)*
FITS	Flexible Image Transport System *(pp. x, 14, 25–27)*
GPL	Gradient Path Labelling *(pp. 15–17, 19, 45, 49–51, 62)*
HDU	Header/Data Unit *(p. 26)*
HMI	Helioseismic and Magnetic Imager *(p. 8)*
IDL	Interactive Data Language *(p. 14)*
NASA	National Aeronautics and Space Administration *(pp. 8, 12, 22, 42, 65)*
NMS	Non Maximum Suppression *(p. 33)*
NOVA	NOVA University Lisbon *(p. 38)*

NSO National Solar Observatory *(pp. 7, 25, 67)*

PSF Point Spread Function *(p. 28)*
PSO Particle Swarm Optimization *(pp. 13, 18–20)*

RIM regional intensity maximum *(pp. 16, 17)*

SDO Solar Dynamics Observatory *(pp. vi, vii, 8, 9, 12, 15, 22–24, 27, 30, 42, 43, 64, 65, 67)*
SIDC Solar Influences Data Analysis Center *(p. 23)*
SOHO Solar and Heliospheric Observatory *(pp. 8, 9, 14, 67)*
SPINLab Space-Planetary Interactions monitoring and forecasting Laboratory *(p. 24)*
SSD Sum of Square Differences *(pp. 31, 32)*

VSO Virtual Solar Observatory *(pp. 25–27)*

1 Introduction

This chapter discusses the key topics that inspired the study of the Sun and its behaviour. The chapter outlines the primary objectives for developing a new tool, to study the Sun, and highlights the significant contributions this work makes to the field of engineering. By examining these elements, readers will gain a deeper understanding of the motivations behind this study, the goals set, and the potential impact on future engineering applications.

1.1 Motivation

The fascination with space and its behaviour dates back to ancient societies where most of their study was done by monitoring what they could see with the naked eye. However, as the centuries went on telescopes became prevalent, which gave a better understanding of what was being observed. More recently, it developed to satellite images, which can be saved and accessed nearly whenever it is wanted, giving an even better assessment of what is being studied.

Given the advance in space image acquisition technology, researchers found that using computer vision and image processing could automate and reinvent the study of space as we know it, as well as the growth of machine learning could motivate to achieve better results.

Continuing with this technological advancement, one of the crucial research areas that needs to be enhanced is the examination of the behaviour of the greatest star in the solar system. The Sun is a fundamental component in our galaxy, as it is the main actor in the solar system that Earth belongs to. It is known that its behaviour can affect every planet in the solar system, as it plays a critical role shaping the planetary Dynamics including the orbits of the planets. Furthermore, the Sun's energy output can cause space weather storms that can impact Earth, as seen in a number of events such as in 1989, when a solar flare caused geomagnetic storms that disrupted electric power transmission from the Hydro Québec generating station in Canada, plunging 6 million people into darkness for 9 hours, or even more recently, in 2005, when X-rays from a solar storm disrupted satellite-to-ground communications and Global Positioning System (NASA, 2021).

The Sun, in contrast to the Earth, is not solid and is divided into many different regions, beginning with the interior regions, which include the core, the radioactive zone, and the convection zone. Moving outward, it can be recognized the photosphere, the chromosphere, followed by the transition zone, and finally, the corona, which is the Sun's vast outer atmosphere. Some solar key features, such as sunspots, CBPs, solar flares, solar prominence, and even spicules, can be seen in these regions. Sunspots are dark areas on the photosphere caused by magnetic activity, while CBPs are bright regions in the corona that indicate active magnetic fields. Solar flares and prominences are explosive events that release energy and material into space, while spicules are small, jet-like structures that protrude from the chromosphere. Figure 1.1 presents a visual representation of the structure that was described.

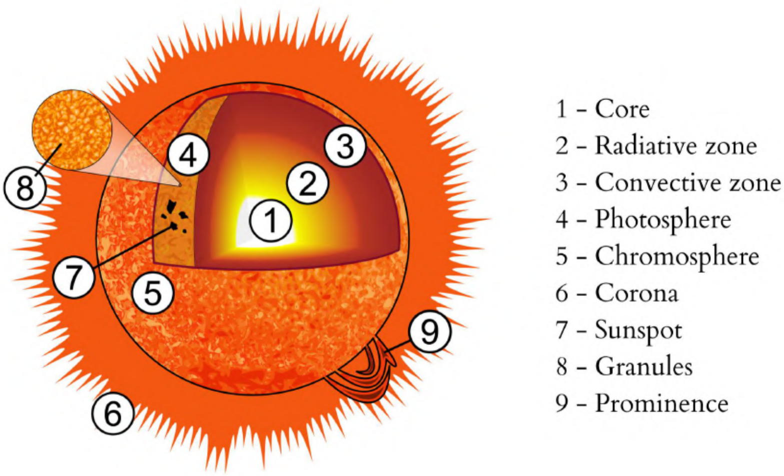

Figure 1.1: The structure of the sun. Adapted from "Sun diagram - Wikimedia Commons" (2008)

As was briefly mentioned in the previous paragraph, the Sun is not solid, so it is known that it has a differential rotation, which means that the velocity rotation is not equal throughout every latitude. As it is believed to play a critical role in the development and maintenance of solar magnetic fields as well as the Sun's overall activity (Brajša et al., 2001), the rotation of the Sun is an essential aspect of its activity and can shed light on the mechanics of the Sun's atmosphere and interior. It may also provide significant data on forecasting space weather.

This dissertation focuses on using computer vision as the main tool to detect and track solar features that will offer the necessary data to complete the computations in order to understand the solar differential rotation.

When deciding which feature to use for the image processing, Dorotovič et al. (2018) and Brajša et al. (2001) point out that sunspots were previously used to estimate the solar rotation profile because they were simpler to detect than other solar features using ground-based telescopes. However, with the arrival of satellites, CBPs can now be observed in the EUV of the solar spectrum and offer a better trace of the rotation of the Sun. In contrast to sunspots, which are known to be found near the equator and are frequently not observed during the minimum of the cycle, CBPs have been regarded as excellent for tracking because they emerge at considerably higher latitudes and in high abundance. Section 2.3 will provide better explanation of each feature.

1.2 Goals

This dissertation aims to investigate the solar rotation profile using computer vision, in order to provide better quality data for the study of the Milky Way's most important star. To achieve this purpose, it is necessary to develop an automated system that will, given the provided dataset, offer reliable estimations and publish them on a web interface.

The first stage of developing this dissertation is to collect and analyse the features that are characteristic of the Sun. This step is of tremendous importance as it will determine the feature that will be used for the tracking and, therefore, the calculations.

The following step is to determine which are the best methods available and that were already used for the detection of objects in images, as well as the methods that were used for tracking objects.

The third step is to apply all of what was mentioned above in order to achieve the result of the velocity of the Sun's differential rotation.

Lastly, after obtaining the results, these will be published and made available through a web portal for anyone curious about this topic.

1.3 Contributions

To better understand the work developed during this dissertation, the main contributions can be summarised as follows:

- Use a new image processing algorithm for the detection of CBPs based on the template matching technique.
- Improvements to the tracking algorithm from Pires (2018)
- Integration of the detection of Coronal Holes, proposed by Carreira (2020).
- Website performance update and new layout for better user experience
- Enhanced plots and best-fitting curves depicting solar rotation velocity are now available on the website, featuring near real-time updates.
- New website page related to the Coronal Holes information, offering an interactive slideshow about their position in the solar corona.

1.4 Document Structure

The next chapters are organised in the following way:

Chapter 2 presents the state of the art, where some of the related works and subjects pertinent to this dissertation are examined and studied. It includes some topics such as how the solar rotation works, imaging of the sun using ground telescopes and satellites, solar features, some feature detection algorithms and tracking methods and Space Weather Websites that are currently available. The development of the web tool, including the employed methods, is detailed in **Chapter 3**. This chapter provides an overview of the datasets and algorithms created for this thesis. **Chapter 4** reveals the outcomes of the study conducted with the developed tool. It examines two distinct time frames, comparing them internally and against other relevant works. The report is concluded and summarised in **Chapter 5**.

2 State of the Art

In order to perform a better work on understanding and calculating the Sun's rotation, it is important to delve into some other previous research involving this subject and other subjects revolving the matter.

This chapter serves as a comprehensive overview of the advancements made in understanding and analysing the dynamic nature of the Sun's surface as well as the advancements made in the technology utilised for that effect. It will cover the study of the solar profile rotation (2.1), some of the current Sun imaging using telescopes and satellites (2.2), features of the Sun (2.3) and some State of the Art techniques and methodologies in the field of features detection algorithms (2.4) and tracking methods (2.5). Some of the existing websites on space weather forecasting (2.6) will also be presented.

2.1 Solar Profile Rotation

Since the sixteenth century there has been research about the sun's rotation, when it was announced the discovery of the sunspots and their movement over the solar surface was noticed. In those early studies, Scheiner (1630) noted that the sun rotated at different velocities at different latitudes, therefore the name "differential rotation". This particularity of the Sun was later proved by the fact of it not being a solid star but instead being composed mainly of gases.

The calculations of the time that it takes the Sun to do a full revolution were made trough some theoretical methods as well as some methods involving the track of solar features. It was concluded that it take approximately 25 days near the equator and about 33 days near the poles (Thompson et al., 1996). Figure 2.1 illustrates how the the Sun's rotation varies by latitude.

An important aspect to take in consideration when talking about this topic, is that the Sun's rotation is dependent on the solar activities, meaning that the calculations can be affected given what type of activity is occurring during the period of time used for it.

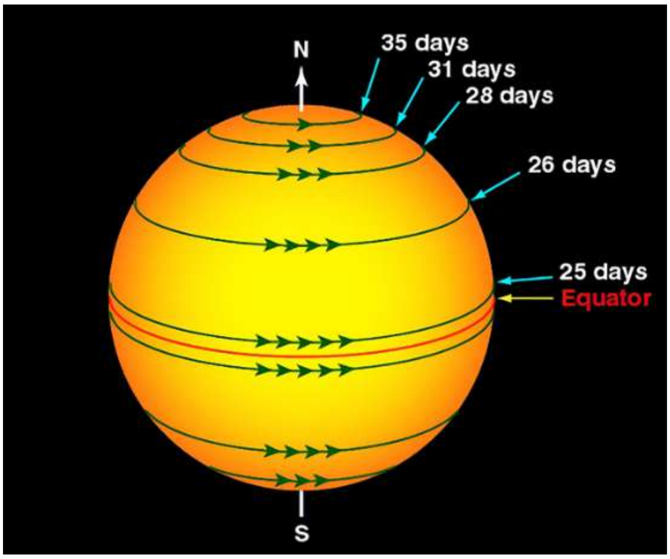

Figure 2.1: The Sun's differential rotation. (NASA, 2017)

For example, Imada and Fujiyama (2018) confirmed that Sun features with strong (weak) magnetic fields result in a faster (slower) differential rotation.

The continuous study of the rotation of this star is of great importance as it will contribute to a better understanding of astrophysics and cosmology. By better understanding the intricacies of the Sun's rotation, scientists can gain valuable insights into the fundamental processes occurring within stars and further enhance our knowledge of the broader universe. Through ongoing research, scientists aim to unravel the complex mechanisms driving the Sun's differential rotation, contributing to advancements in our understanding of astrophysical phenomena.

2.2 Satellite and Telescopes Images

Sun images can be obtained using a variety of instruments and techniques, each with their unique strengths and limitations. In this section, we will explore some of the techniques used to capture high-resolution images of the Sun from space and ground-based observatories.

2.2.1 Telescopes

The first images of the Sun were seen and captured with the help of telescopes dating back to the year 1845 taken by French physicists Louis Fizeau (NASA, 2006). Now, with the evolution of technology, the most recent telescopes in use can capture even more stunning images of the Sun. A few examples of telescopes in use are:

Big Bear Solar Observatory (BBSO) - Constructed in 1970, this ground-based observatory in California uses optical and infrared instruments to observe the Sun and provides photos and data about the planet's surface and magnetic activity (BBSO, 2023b). The New Jersey Institute of Technology is presently in charge of it.

GREGOR solar telescope - This ground-based telescope is situated in the Canary Islands, Spain, and is intended to observe the Sun's photosphere and chromosphere with high spatial and temporal resolution. Adaptive optics are used to correct atmospheric distortion and take high-resolution pictures of the Sun's surface, providing information on the Sun's magnetic fields and other features. It was built by a German consortium and it is the largest European solar telescope for the visible and near IR spectral regime ("GREGOR Solar Telescope", 2023).

Daniel K. Inouye Solar Telescope (DKIST) - It is currently one of the most sophisticated telescopes, it is situated in Hawaii and currently managed by the National Solar Observatory (NSO). It has a four-meter primary mirror and is capable of capturing high-resolution images of the Sun's surface and magnetic fields. It also has spectrographs that can analyze the light emitted by the Sun in detail, revealing information about the temperature, density, and velocity of the solar atmosphere. Its construction began in 2010 and the first solar images were captured in late 2019 (NSO, 2022).

In figure 2.2, it can be seen some of the images that were captured by the telescopes that were mentioned previously.

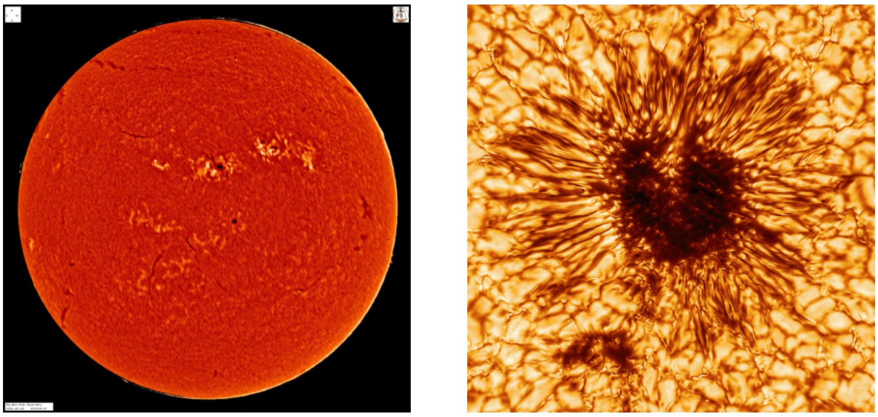

(a) H-alpha image taken from BBSO (May 08, 2023 at 22:50:33 UT) (BBSO, 2023a)

(b) First sunspot image taken with DKIST (January 28, 2020) (NSO, 2023)

Figure 2.2: Images captured from ground telescopes

2.2.2 Satellites

Satellite sun images offer a fascinating glimpse into the dynamic and amazing nature of our nearest star. These remarkable images are captured by specialized satellites that are specifically designed to observe and study the Sun from space. By utilising advanced instruments and imaging techniques, these satellites provide us with a unique perspective on solar phenomena. Some instances of satellites that are essential in revealing the secrets of our extraordinary Sun include:

Solar and Heliospheric Observatory (SOHO) - This observatory is a international collaboration between National Aeronautics and Space Administration (NASA) and European Space Agency (ESA) that launched on December 2 , 1995. In order to monitor the impacts of space weather on Earth and predict potentially severe solar storms, it is primarily focused on observing the Sun's inner structure, corona, and the solar wind that continuously streams out into space. This satellite is equipped with twelve different instruments, all with different purposes, such as the Extreme ultraviolet Imaging Telescope (EIT), and it was the first solar observatory providing an uninterrupted view of the Sun as it does not orbit around the Earth (NASA, 2019). Although SOHO was intended to last for only two years, it is still operating through the year 2023 due to its extraordinary results.

Solar Dynamics Observatory (SDO) - This satellite was put into orbit on February 11 of the year 2010 with the objective of improving the understanding of how the Sun's magnetic field is generated, structured, and how it influences the solar atmosphere and heliosphere. This spacecraft is equipped with three advanced instruments that perform different measures of various properties of the Sun. These instruments consist of the following:

- Atmospheric Imaging Assembly (AIA) - observes the Sun's atmosphere in multiple wavelengths, allowing the study of temperature, density, and dynamics of different layers. The images of this instrument are the ones that this masters dissertation will be focusing on.
- Helioseismic and Magnetic Imager (HMI) - offers information on the Sun's magnetic field, enabling the research of solar activity and the dynamics of solar surface oscillations.
- EUV Variability Experiment (EVE) - measures the EUV irradiance in order to to comprehend variations on the timescales that affect Earth's climate and near-Earth space.

The observatory's chosen orbit has the drawback of being interrupted twice by Earthly eclipses and three times by lunar eclipses, yet it is essential for the nearly continuous and high-data-rate images because it allows images to be made available with such a fast cadence (SDO, 2023a).

Solar Orbiter - As the SOHO, this satellite is also a collaboration between ESA and NASA that was launch in February of 2020. What sets apart this particular observatory is its unique and challenging orbit, which travels toward the sun every five months, passing within 42 million kilometres of it ("Solar Orbiter", 2023). Compared to the maximum latitude that can be observed from Earth, which is seven degrees, this orbit enables the observatory to retrieve images from latitudes up to 24 degrees, and after eight years, up to 30 degrees. This will deliver groundbreaking images of the

Sun's polar regions, revealing important details about the region's little understood magnetic environment, which contributes to the Sun's 11-year solar cycle and its recurrent outburst of solar storms. To be able to measure solar wind plasma, fields, waves, and energetic particles when they are still relatively pure and close to the Sun, it is equipped with ten instruments. These measurements provide insight into what is actually streaming off the Sun before it evolves in interplanetary space (NASA, 2023).

Figure 2.3 shows some images that were taken with the satellites that were mentioned before.

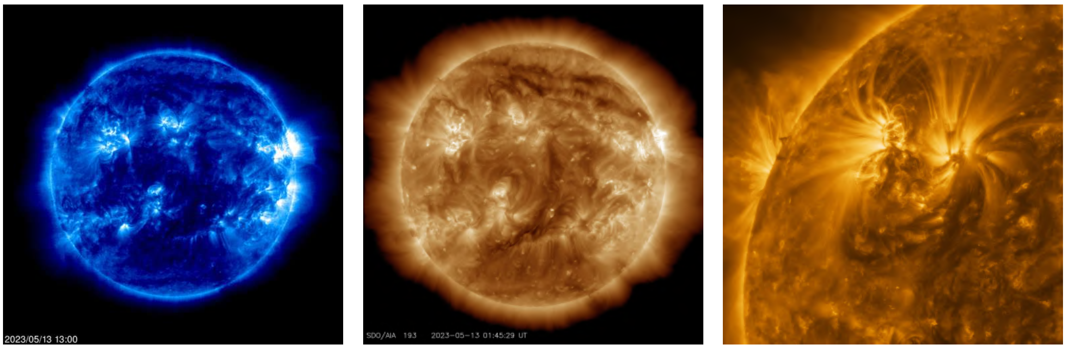

(a) Sun image taken from SOHO/EIT (May 13, 2023 at 13:00 UT) (SOHO, 2023)

(b) Sun image taken from SDO/AIA (May 13, 2023 at 01:45:29 UT) (SDO, 2023b)

(c) Close up from image taken with the Solar Orbiter (March 7, 2022) (ESA, 2023)

Figure 2.3: Images captured from Satellites that observe the Sun. The color of the images are a result of the channel wavelength of the instrument.

2.3 Sun's Feature Selection

In order to calculate the differential rotation using a tracer method, it's crucial to decide which solar attributes are best for the particular study. A few of the primary solar features, such as sunspots and CBPs, will be discussed, along with some benefits, drawbacks and interesting facts.

2.3.1 Coronal Mass Ejections

These solar features, known as Coronal Mass Ejections (CMEs), were discovered very recently at the beginning of the seventies and they are colossal eruptions of magnetized plasma from the Sun's corona, being prominences (see Solar Prominences and Filaments) one responsible factor of their formation (Gopalswamy, 2016; Webb & Howard, 2012). These explosive events release a tremendous amount of energy and magnetic fields into space, propelling billions of tons of charged particles into the solar system, being responsible for space weather effects on Earth.

The most noticeable consequence is the disruption of geomagnetic activity, resulting in vivid auroras visible at high latitudes on Earth. However, CMEs also possess the potential to disrupt satellite operations, interfere with communication and navigation systems, and induce electrical currents in power grids, leading to blackouts. That is why it is so important to understand and try to predict their behaviour.

Even though this feature can be used to study the solar rotation, it is not the first choice as it is not possible to do so directly, which suggests that other types of understanding, such as knowledge of the Sun's magnetic fields, are required to deduce the time that it takes to perform a full revolution.

2.3.2 Solar Prominences and Filaments

Solar prominences (or filaments) are captivating and dynamic features of the Sun's atmosphere that exhibit large-scale eruptions of plasma. They are composed of dense, cool gas suspended in the Sun's hot and tenuous corona. Although prominences and filaments refer to the same solar phenomena, filaments are found on the solar disk (fig. 2.4b) while prominences are visible near the solar limb (fig. 2.4a) (D. S. Mackay et al., 2010), so as the Sun rotates the filaments will turn into prominences as they will appear at the extremity.

One key characteristic of this solar feature is their association with the Sun's magnetic field, as they occur along regions of extreme magnetic activity, which are often found near sunspots or active regions on the solar surface. As a result, filaments can be noticed throughout the Sun's disk during times of intense sunspot activity, just like illustrated in figure 2.4b.

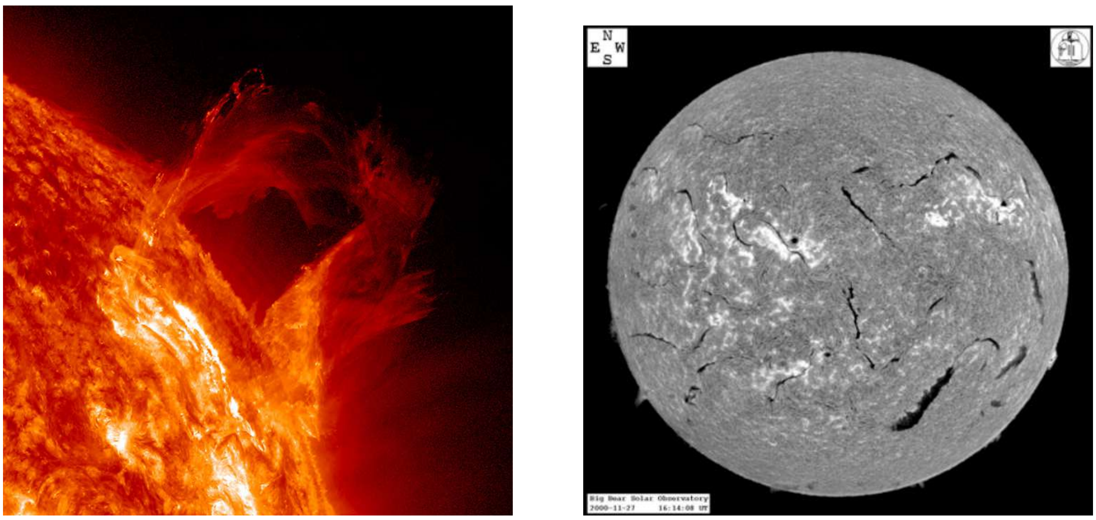

(a) Still from a video of a solar prominence erupting. Retrieved from Addison (2023)

(b) H-alpha image containing solar filaments over the solar disk. (D. H. Mackay, 2021)

Figure 2.4: Examples of solar prominences and filaments.

They are known to be generally stable with lifetimes that may exceed a solar revolution, yet they show rapidly developing small structures as well as a diverse range of flows and oscillations. Both filaments and prominences regularly erupt from the Sun where they and their surrounding magnetic field combine to form a CME which can lead to Space Weather (D. H. Mackay, 2021).

The best way to use this feature for differential rotation research is to study its helio-seismology. This implies that it is difficult to use them as tracking features and therefore not suitable for the methods that are aimed to be used in this dissertation. Nonetheless, they remain to be of great interest in discovering the mysteries of the Sun's intricacies and dynamics.

2.3.3 Sunspots

As demonstrated in earlier research, such as Balthasar et al. (1986) and Kambry and Nishikawa (1990), sunspots were utilised as the first primary tracer features for determining the solar differential rotation as they were easier to distinguish among all the manifestations of solar activity. However, sunspots are not evenly distributed across the Sun's latitude. During the solar maximum, they are more frequent between 30ºN and 30ºS, during the minimum they tend to appear more close to the equator, as it is depicted in figure 2.5. It is also important to note that the amount of active sunspots vary during the solar cycle and that they have a complex and evolving structure (Dobrijevic, 2022).

Potential effects of magnetic fields linked to sunspots on the measurements of the solar differential rotation are also a crucial factor to take into consideration. The movement of plasma within the Sun's core may be influenced by magnetic fields, which in turn may alter the pace at which the Sun's surface is observed to rotate (Jones et al., 2009).

An interesting observation about sunspots is that they are classified in different kinds of classes based on their size and distribution inside a group. Sunspot classification was invented with the objective to report sunspot data rapidly and consistently (P. S. McIntosh, 1990), however it is frequent for sunspots groups to change or evolve with time, meaning they can be classified in a incorrect way ending up undermining the data, given the fact that researchers use only a particular set of sunspots that have a greater intensity.

Sunspots have already been proven to be effective tracking features throughout prior research studies.

2.3.4 Coronal Bright Points (CBPs)

CBPs are small-scale, ball-shaped structures (see figure 2.6) observed in the solar corona that exhibit a strong correlation with magnetic flux concentrations on the solar surface. These bright points often coincide with the footpoints of coronal loops and are typically found in proximity to active zones. It is widely believed that CBPs result from magnetic reconnection events that release energy in the form of heating, causing the coronal plasma to emit radiation at EUV wavelengths (Bose et al., 2023).

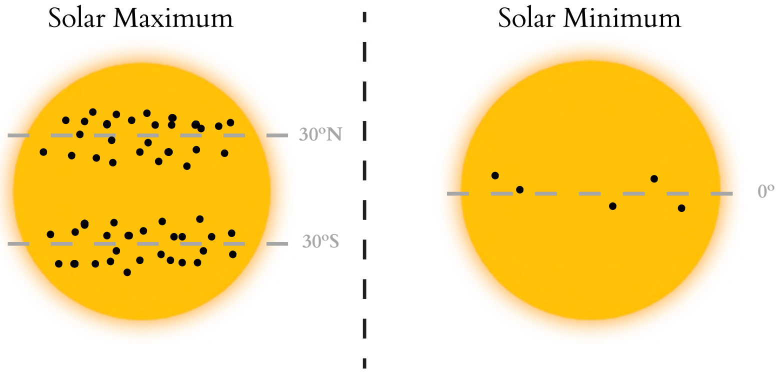

Figure 2.5: Sunspot distribution over the solar cycle.

One remarkable characteristic of CBPs is their abundance, as they appear in large quantities and are distributed throughout the entire surface of the solar corona (Sudar et al., 2015). Additionally, CBPs share a similar shape, which simplifies their detection and tracking. However, tracking them over an extended period can pose challenges due to the variability in their lifespan, which can range from a few hours to a few days. This variability necessitates continuous monitoring and analysis to capture their dynamic behavior accurately.

EUV imaging instruments, such as the AIA on board NASA's SDO, provide the means to observe these small bright spots. These images can be accessed through the SDO website, offering researchers valuable data for studying CBPs and their associated solar phenomena.

Considering the advantages and disadvantages discussed, it is evident that CBPs serve as excellent tracer features and can present more valuable results for the study of the solar rotation.

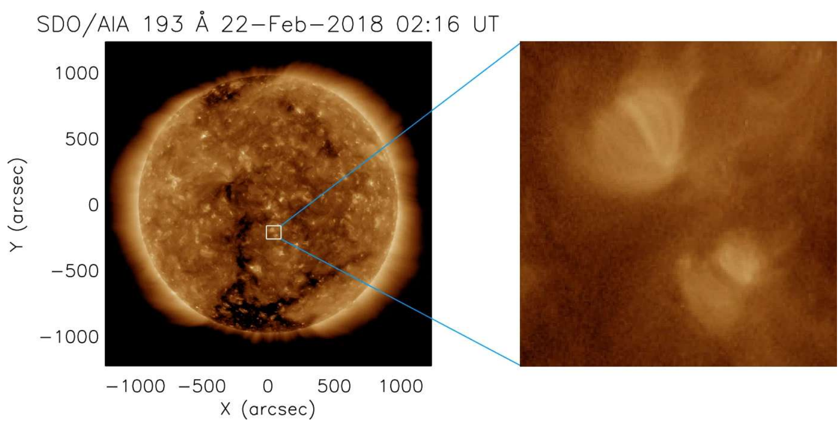

Figure 2.6: Full disk SDO/AIA image in the Fe XII 193 Å channel with a close up of two CBPs. Image from Madjarska (2019).

2.4 Detection Algorithms

The identification of the chosen features can be done manually, as it was done in a study conducted by Lorenc et al. (2012); however, this would be a lengthy work given the enormous set of images and becoming almost impossible to perform. The reasonable method to use is an automatic one, that is when computer vision comes in handy.

Image segmentation is a fundamental process in computer vision that involves partitioning an image into meaningful regions or sections based on specific criteria and, ideally, correlating to actual objects in the scene (Abdulateef & Salman, 2021).

Segmentation techniques in solar observations enable the extraction and delineation of various solar phenomena, facilitating their study and offering important insights into the dynamics of the sun, the behavior of the magnetic field, and space weather forecasting. The traits, sizes, positions, and changes of features can be quantified by segmenting solar images, aiding in the comprehension of their formation and evolution. The main objective is to utilise a specific method to detect and locate CBPs that will allow our study to be successful.

As it is shown in figure 2.7, there are several different categories and methods of image segmentation, on which we will rely on for the implementation of this dissertation. Previous works done on this subject, have already demonstrated that the application of this methods combined with other post-segmentation processes are successful in identifying and detecting solar features. For instance, in the work of Dorotovič et al. (2007), it was applied a watershed software tool to accurately detect sunspots and in the work of Shahamatnia et al. (2013) an algorithm called PSO/Snake Hybrid — which uses the Snake model/active contour of the energy-based category — was employed to detect CBPs.

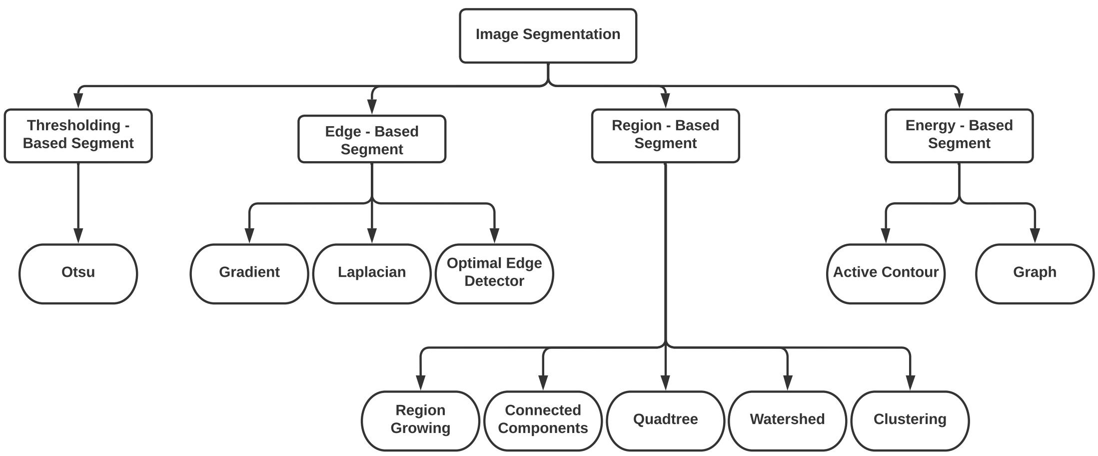

Figure 2.7: Image Segmentation categories and methods based on Abdulateef and Salman (2021)

In this chapter, it will be discussed some detection methods that were successful detecting solar features.

2.4.1 BP-Finder Algorithm

This detection algorithm was proposed by Mcintosh and Gurman (2004) as an adaptation of a previous algorithm written in Interactive Data Language (IDL), benefiting from certain aspects from the latter.

The BP-Finder algorithm works by getting the EIT FITS file and performing the standard steps gathered in the EIT User Guide. This process involves several procedures. First, dark current subtraction, degridding, filter normalization, exposure normalization, response correction, and removal of vignetting and stray light are performed. Following that, an additional step is taken to reduce the visibility of the grid pattern and associated artifact bright points. Bright spikes, predominantly cosmic rays, are removed using a two-dimensional median filter. An image of the EUV background intensity is formed through boxcar smoothing, and the enhanced EUV regions are obtained by subtracting the background intensity from the original image. The noise level of the background data is calculated by considering photon statistical noise, dark noise, and stray light noise. The deviation image is then computed to estimate the significance of the enhanced EUV regions, and regions with a deviation exceeding a certain threshold are identified as bright point candidates. To differentiate between neighboring pixels satisfying the criteria, shape selection rules are applied, including restrictions on the horizontal-to-vertical width ratio and the occupied area. Finally, the detected bright points are numbered and stored in a database with relevant information such as location, area, and integrated intensity. See Mcintosh and Gurman (2004) for a more detailed explanation of the algorithm.

The results of the presented method can be observed in figure 2.8, where it is shown the CBPs identified on the SOHO/EIT image on the 195Å channel as black asterisks.

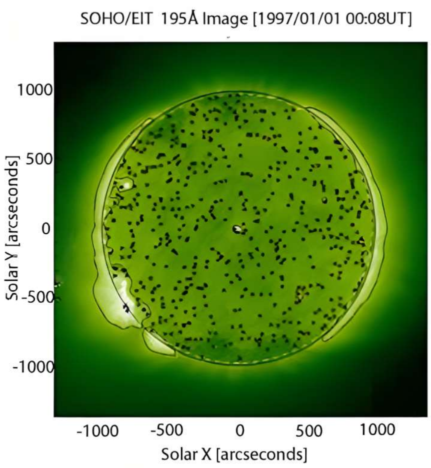

Figure 2.8: SOHO/EIT 195Å image from January 1, 1997. Image taken from Mcintosh and Gurman (2004).

Since the first paper containing this method was published, the algorithm has undergone some improvements throughout the years, either by the same author, S. W. McIntosh and Gurman (2005), or other researchers such as Martens et al. (2012) and Sudar et al.

(2015). Some of the improvements done were include size limits adjusted by limb angle, merging of spatially close CBPs to reveal underlying structures, and constraints to avoid the detection of quiet Sun patches and long ribbon-like structures (Martens et al., 2012).

The results of those upgrades are presented in figure 2.9, where image 2.9a displays the result of the algorithm presented by S. W. McIntosh and Gurman (2005) in which the detected CBPs are highlighted in a black contour, and image 2.9b exhibits the result of the algorithm presented by Martens et al. (2012) that was used in the work of Sudar et al. (2015).

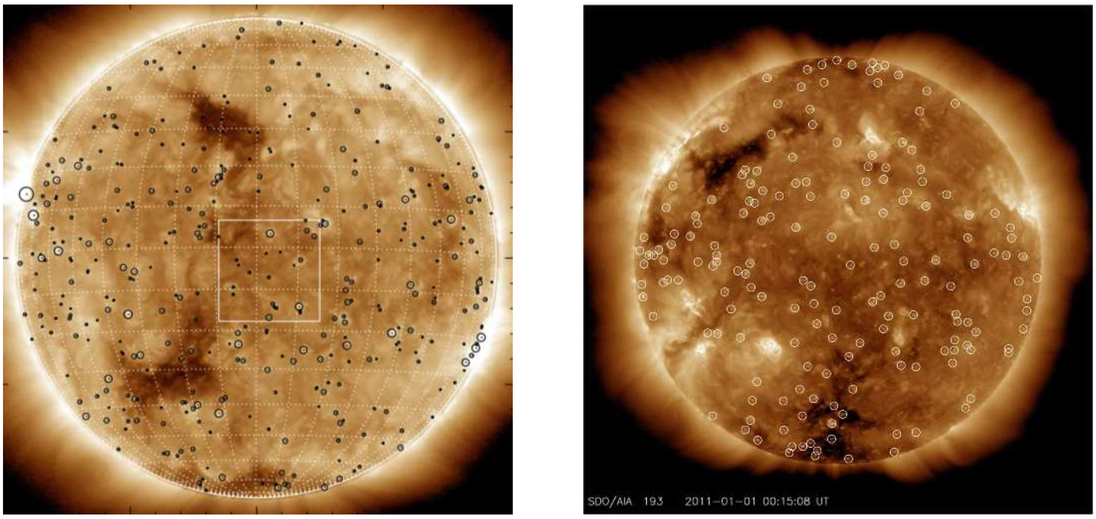

(a) Retrieved from S. W. McIntosh et al. (2014). CBPs highlighted in black.

(b) Retrieved from Sudar et al. (2015). CBPs highlighted with a circle.

Figure 2.9: Full disk SDO/AIA images with the detected CBPs highlighted.

The BP-Finder method was concluded to be successful for the purpose of detecting CBPs as Sudar et al. (2015) said in its conclusions: *"The segmentation algorithm used here proved to be completely adequate for the task"*.

2.4.2 Gradient Path Labelling (GPL)

The Gradient Path Labelling (GPL) was originally created to identify Drusen, which is a feature that indicates an eye disease, in retinal images proposed by Mora (2010), however it has already been used to detect CBPs in previous works such as the ones performed by Dorotovič et al. (2018) and Shahamatnia et al. (2016). The latter defended that it was a promising domain, given that the CBPs are higher intensity regions.

This segmentation method has some resemblances to the connected components algorithm, yet its purpose is to isolate objects from each other and the background. The output produced can be compared to the Watershed algorithm, although the GPL is faster and more optimized. The comparison between the segmentation performed on a image of rice by the Watershed method and the one performed by the GPL is presented in figure 2.10.

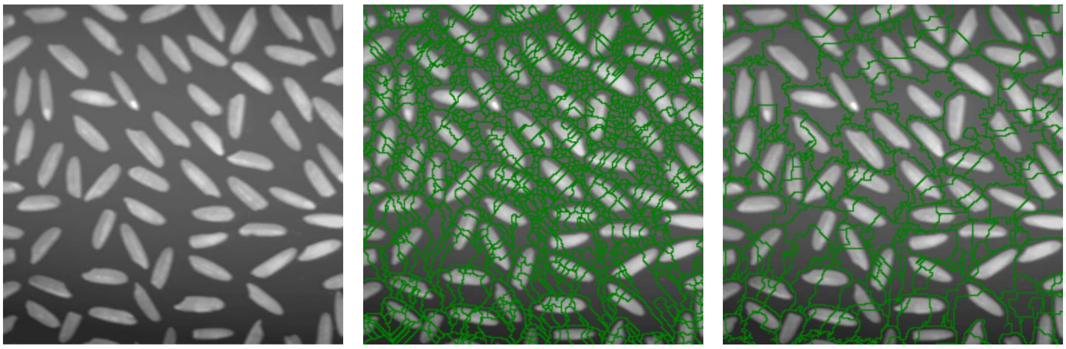

(a) Original (b) Watershed (c) GPL

Figure 2.10: Comparison between the Watershed Transform and the GPL method. Retrieved from Mora (2010)

It is a maximum intensity algorithm based on the labelling of gradient paths and its principle is that one or more paths reach the same maximum intensity so, the convergence of numerous significant ascending paths indicates the presence of a regional intensity maximum (RIM). The algorithm discovers RIM and regions of influence, which are formed by pixels belonging to the feature ascending path, followed by a grouping of those paths belonging to the same RIM. The outcome is a segmented image in which the features are separated from each other.

There are two main processes in this method, with the first being the labelling and the second the labels merging.

2.4.2.1 Labelling

This process is designed to aggregate groups of pixels with similarities by assigning them with common labels. As the GPL utilises the gradient image to evaluate the ascending paths, this image is obtained by calculating the first derivative of the image intensity relying on the use of edge detection methods, such as Roberts or Sobel filters, with Sobel being the filter chosen by Mora (2010), justifying that it presents better results.

After the application of the filter, it is possible to determine the angle between the horizontal and the vertical derivatives (gradient angle), which will provide the direction to the ascending intensity path. Assuming the 8-connectivity (horizontal, vertical and diagonal connectivity), the gradient angle is rounded to one of the possible directions (figure 2.11a).

The next step to perform is the label propagation, where the label is propagated to the pixel pointed by the gradient angle, continuing to be propagated until the next pixel is already marked or out of bounds. There is a equivalence table that stores all the label equivalences in order achieve the final image labelling map. There will be as many labels as RIMs detected. Both the label propagation and the equivalence table are shown in figure 2.11b and 2.11c, respectively.

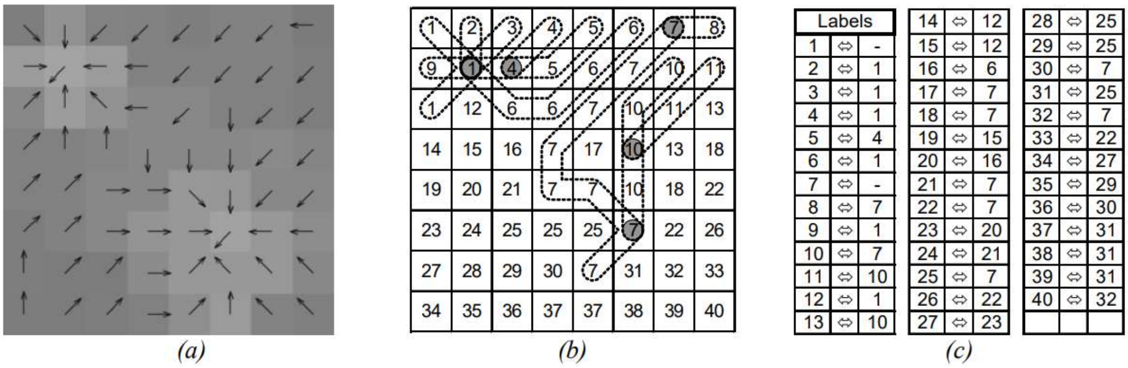

Figure 2.11: GPL Labelling Process. a) Pixel propagation directions; b) Initial label propagation and label propagation of the two upper rows; c) Labels equivalence table. Courtesy of Mora (2010).

The result o f the labelling process is illustrated in figure 2.12, where it is clear that there were two RIMs.

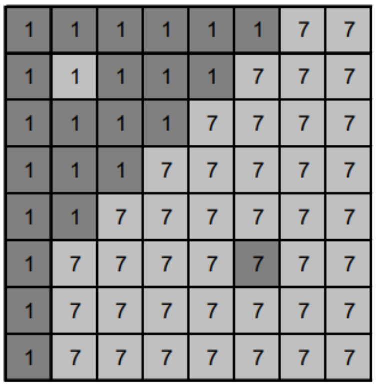

Figure 2.12: GPL final labels result image. Courtesy of Mora (2010).

2.4.2.2 Labels Merge

When in the presence of *plateaus* (flat hills) not all gradient paths end on the same RIM pixel so, this process appears in order to address over-segmentation that occurs in the image.

The merging technique is based on a connectivity graph analysis to detect and merge valid paths based on certain conditions. The graph represents labels as nodes and their relationships as links, with link intensities reflecting the strength of the connections. By sequentially evaluating each node and its neighbours, the algorithm searches for links that satisfy the merging condition. The search process is optimized by sorting the neighbours' list in descending order of link intensity. Once a suitable link is found, the merging operation takes place, updating labels, maintaining equivalences, and merging neighbours' lists. The algorithm iteratively reevaluates the graph after each merge, ultimately resulting in an updated connectivity graph with merged paths.

The application of the merging algorithm results in a less segmented image, presenting a better precision on delimiting the image's features.

2.4.3 PSO/Snake Hybrid Algorithm

As it was mentioned in the introduction of this chapter, the PSO/Snake Hybrid is an algorithm developed by Shahamatnia and Ebadzadeh (2011), initially with the purpose of being used in medical imaging, such as CT scans or MRIs, being then applied on the study of the solar rotation by detecting CBPs. This algorithm is called Hybrid due to its approach, which combines an image segmentation active contour method known as Snake model and a optimization algorithm called Particle Swarm Optimization (PSO).

The PSO algorithm is a population-based stochastic optimization technique inspired by the social behaviour of bird flocking. A population of potential solutions, known as particles, travel the search space in pursuit of the optimal solution to a particular problem. Each particle in the search space is a possible solution. The particles in the population can adjust themselves based on the experiences of other particles' in the area they explored, with the goal of converging to the most favourable search area, which is the solution to the given problem (Shahamatnia et al., 2016).

The Snake method is a popular image segmentation technique used to extract and track the boundaries or contours of objects in an image. It gets its name from the way the shapes move and slither while conserving energy, mimicking the behavior of a snake. The energy-minimising splines known as contours (or snakes) are driven by both internal and external forces that induce the snake's energy. The snake is pushed toward salient image features like lines, edges, object size or shape by the external energy while the internal energy encourages the contour smoothness and regularity (Shahamatnia et al., 2013). During the iterative process, the contour evolves under the influence of these forces, seeking the balance between fitting the contour to the desired object boundaries and minimizing the internal energy. This approach has a major drawback as it requires adequate initialisation in order to be effective, since it is extremely sensitive to the position of the first contour.

Therefore, the PSO algorithm is applied to improve the snake's energy equations while also helping resolve the previously mentioned problem, upgrading the traditional Snake approach into a more accurate one.

An example of the PSO/Snake Hybrid being used to identify CBPs can be seen in figure 2.13, where it is presented the evolution of the contours since the initialisation on the top panel to the correct final contour on the bottom panel. It is noticeable how the contour deforms itself in order to achieve the best contour.

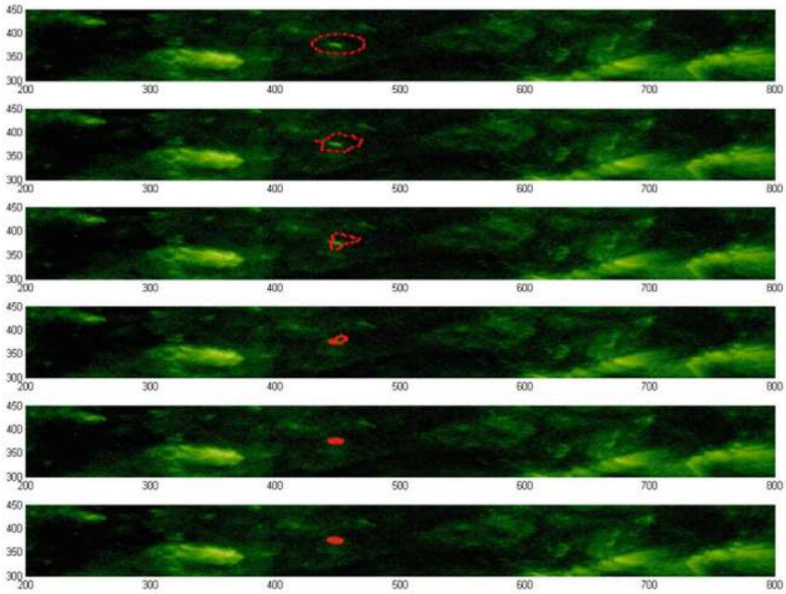

Figure 2.13: Evolution of the contour using the PSO/Snake Algorithm. Image borrowed from Shahamatnia et al. (2016)

With regard to the detection of CBPs, Shahamatnia et al. (2016) notes that the GPL method outperforms the PSO/Snake Hybrid in calculation speed due to its low computational complexity.

2.5 Tracking Methods

In order to calculate the differential rotation of the Sun, after detecting the selected solar feature, it is necessary to follow the progress of the path that it carries out. For that matter, in other words, it is needed to track the CBPs using an automated method.

In this section some of those methods will be discussed considering the algorithms used in previous works.

2.5.1 Feature-Based

One way of tracking an object is to use feature extraction as a way to compare the features that were detected throughout the different images. There is a model known as the Similarity Model in which defines the space of the feature so that the similarity between two or more images can be compared (Curiale et al., 2018). It is in this model that the feature-based image comparison method can be found.

The feature-based method is useful when it is known what kind of object is being tracked, such as CBPs, and it is possible to compare its features. The similarity measure can be defined as something like the spatial distance between the two objects.

This kind of tracking is the one used in the work of Dorotovič et al. (2018), where the CBPs were tracked by searching in the previous three images using the (x, y) pixel locations and the Euclidean distance according to a maximum range, with this range being 5, 8 and 12 pixels for the last first, second and third image respectively. If no CBPs are detected, a new unique identifier is assigned, otherwise, the identifier of the closest CBP is assigned. The search up to the previous three images was chosen due to inconsistencies in the detection and activity of CBPs, which cause detection gaps on certain snapshots.

This kind of tracking method has proven to be successful in previous works, and it is known to be more successful when the image cadence is lower, for example, it will provide better results if the cadence of the images is a new image every 5 minutes instead of 10 minutes.

2.5.2 PSO/Snake Algorithm

This algorithm is used both for detection, as it was explained in 2.4.3, and tracking. When it comes to tracking, the algorithm utilises the next image as an input, sending information about the feature profile and its contour, and applies the PSO to recalculate the social and cognitive parts of each particle and to move the contours until they converge to the correspondent feature of the new image (Shahamatnia et al., 2013). In other words, this method is constantly tracking features by detecting them, based on their information from the previous image, in the following images.

One significant disadvantage of adopting this method as a tracking tool is that, given it is an iterative process, the execution time could prove to be very lengthy (Shahamatnia et al., 2016).

2.5.3 Optical Flow

The apparent motion of image elements between two successive frames produced by object or camera movement is referred to as Optical Flow. This method works by assuming that the pixel intensities of a feature do not change between images and that the neighbour pixels have a similar motion. It utilises a small window around the given feature to restrict the motion estimation to a local region so that, after, it can calculate the spatial gradient of the intensity values and the temporal gradient within the window. After obtaining the gradients, it is necessary to apply a mathematical method in order to achieve the motion vector that represents the movement prediction. One of the most common methods to be used is the Lucas-Kanade method, which employs a least squares estimation approach and iteratively refines the solution until convergence, improving the accuracy of the optical flow estimation. The Lucas-Kanade method may not be appropriate for large motions, however, that is not the case in this dissertation.

It can be seen in figure 2.14 how the optical flow traces the movement of the points that are given. Here, the lines were traced given the result of the function *calcOpticalFlowPyrLK()* from OpenCV.

(a) Frame in the start of the video. (b) Frame of the video after a few seconds.

Figure 2.14: Visual example of how the Optical Flow tracking a car in a video. Image borrowed from www.nanonets.com/blog/optical-flow

2.5.4 Deep SORT

Deep SORT (Simple Online and Realtime Tracking with a Deep Association Metric) is an object tracking algorithm that combines object detection with a sophisticated data association technique. It is widely used in scenarios where multiple objects need to be tracked over time in real-time systems.

The first step of Deep SORT is to detect objects. These detections are then fed into a deep appearance descriptor network, which generates a high-dimensional embedding for each detected object. This embedding encodes the appearance information of the object and serves as a feature representation for subsequent data association.

In the data association step, Deep SORT utilizes a combination of motion and appearance information to associate detections across frames and assign unique track IDs. It employs a Kalman filter-based tracking framework to predict the object's state in the next frame and uses a Hungarian algorithm to optimize the assignment of detections to existing tracks. The deep appearance descriptors play a crucial role in calculating the similarity between detections and existing tracks, enabling robust association even in challenging scenarios with occlusions or appearance changes (Wojke et al., 2017).

This algorithm has already been used by Bo et al. (2022) as a method to track active solar regions throughout a series of full solar disk images and, overall, it is a very powerful tracking tool that can handle complex scenarios, maintaining consistent and reliable tracks of objects overtime.

2.6 Space Data Websites

There are already a few real-time solar tools providing space weather information online, mainly about solar radiation, wind, magnetic field and activity. However there is one website designed to make available information about CBPs and the velocity of the Sun's rotation that was created by Pires (2018).

In this section some of those websites will be presented.

2.6.1 Space Weather Live

The Space Weather Live website (www.spaceweatherlive.com) was established in 2003 by Parsec vzw, a non-profit organization based in Belgium, as part of a broader initiative promoting scientific knowledge in fields such as Astronomy, Space, Space Weather, and aurora-related subjects.

The website offers vital information about global geomagnetic activity as well as current measurements of the Solar Wind, Flares, and CMEs, providing means to monitor the dynamic conditions of the Sun. The page that presents the solar activity can be seen in figure 2.15.

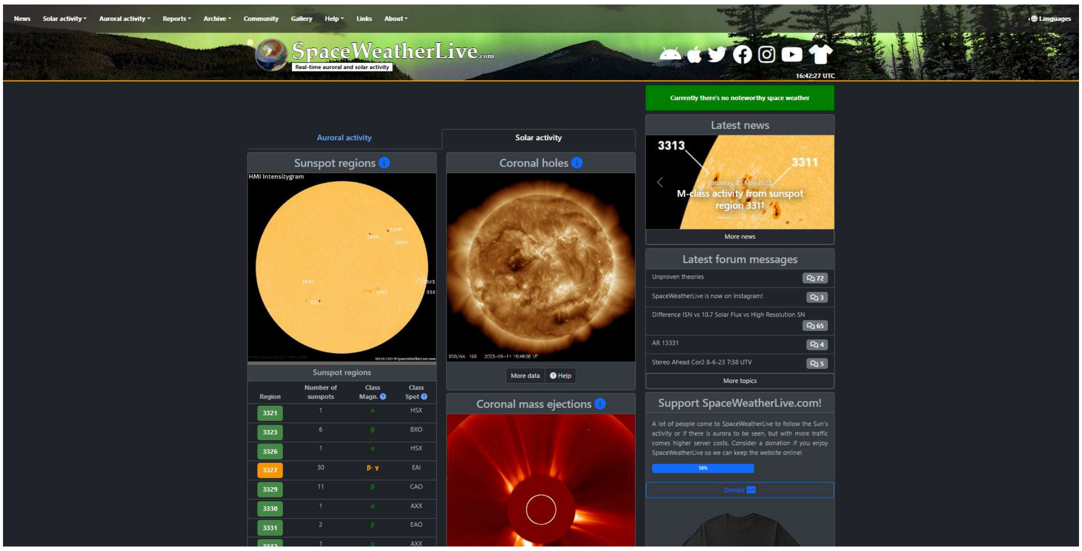

Figure 2.15: Solar activity page of the Space Weather Live website.

2.6.2 Helioviewer

Helioviewer (www.helioviewer.org) is a website that provides a captivating and interactive experience for exploring the Sun's dynamic behavior. It has a user-friendly interface and vast collection of high-resolution solar images and videos from multiple solar missions and observatories, including NASA's SDO, to present its users with real-time and archived solar imagery to showcase solar phenomena such as solar flares, coronal mass ejections, and sunspots.

In figure 2.16, it is possible to see the Helioviewer page showcasing an image captured from the SDO/AIA in the 193 Å channel, pinpointing the active regions in there present.

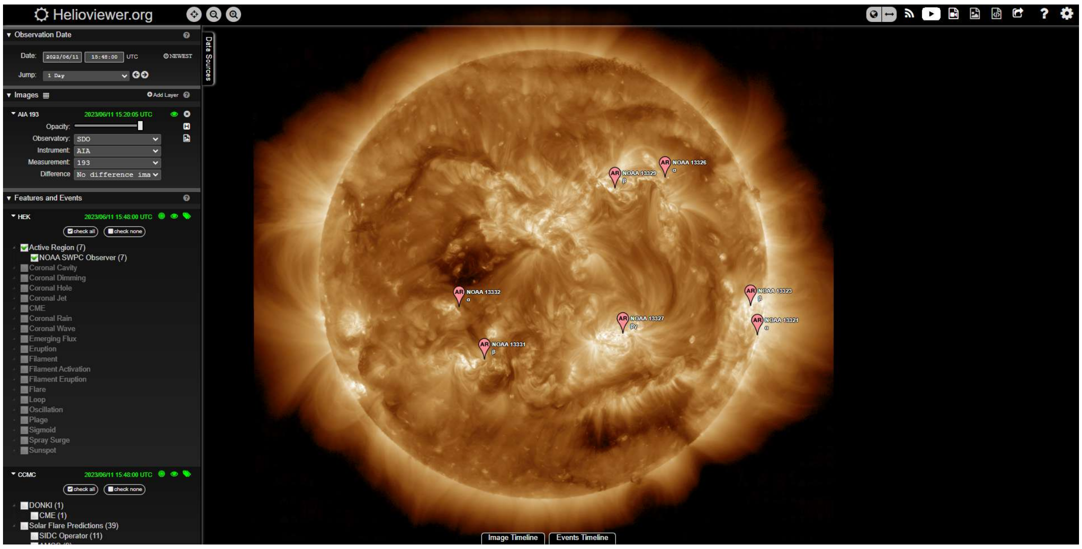

Figure 2.16: Screenshot of the Helioviewer website.

2.6.3 Solar Influences Data Analysis Center (SIDC)

The Solar Influences Data Analysis Center (SIDC) (www.sidc.be) is a renowned institution, situated at the Royal Observatory of Belgium, that specializes in the analysis and monitoring of solar activity and its impacts on Earth.

It provides regular updates on solar activity through its website and publications, ensuring that users stay informed about the latest developments in solar research (figure 2.17). SIDC's expertise also extends to forecasting space weather, which involves predicting the conditions in space based on solar activity.

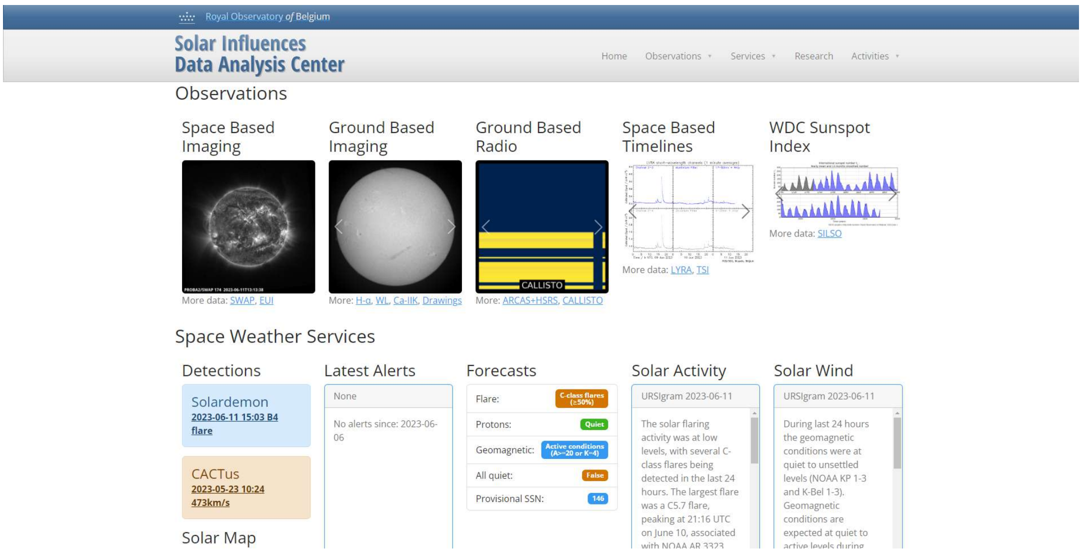

Figure 2.17: Screenshot of the SIDC website.

2.6.4 SPINLab

SPINLab's website is dedicated to space weather having access to 150 years of continuous observations of the geomagnetic field and the Sun acquired by University of Coimbra. It is in this web portal where Pires (2018) made available the results of his work on the Sun's differential rotation and the tracking of CBPs (figure 2.18).

To access this website, it is necessary to navigate to this URL *www.mat.uc.pt/~obsv/SPINLab/SPINLab_home.php* and select the "Solar data"and "UNINOVA"options from the menu.

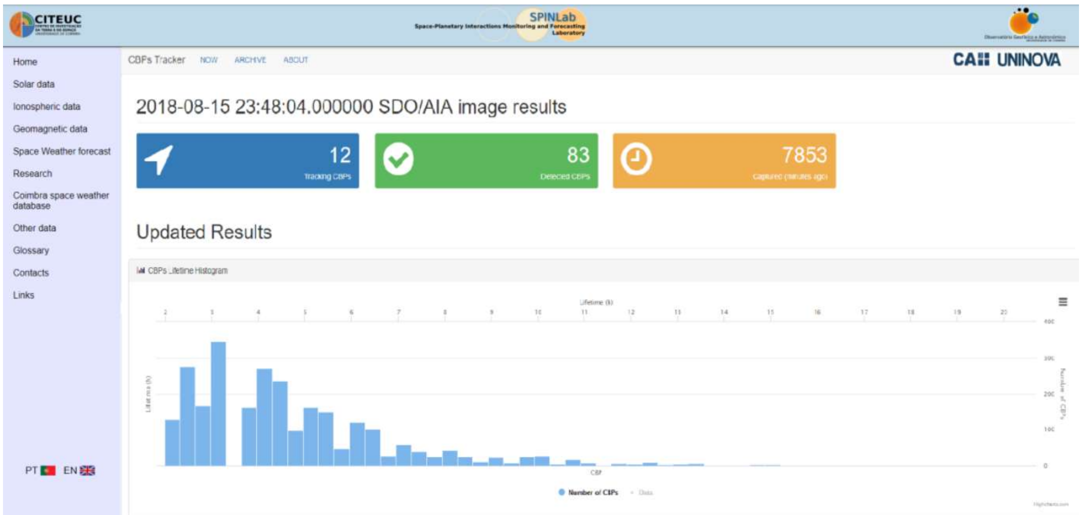

Figure 2.18: CBPs tracking page in SPINLab website (www.mat.uc.pt/~obsv/SPINLab/SPINLab_solSDO.php). Image borrowed from Pires (2018)

2.7 Final Considerations

After the research about state of the art methods and relevant information about the topic of this dissertation, it was possible to have a better idea of what kind of approach should be applied.

Firstly, it was decided that the solar feature that better suits the need of the tool were the CBPs. Given that, the better images to use for the CBPs detection as well as their easy accessibility were the images from the SDO satellite obtained with the AIA instrument. Secondly, it was understood that it was necessary to create a new detection method that could improve the detection and tracking accuracy. When it came to the tracking process, it was decided to use the feature based tracking as it is described in this chapter. Lastly, the website that will provide the information about the CBPs will be an upgrade and extension of the SPINLab website.

3 Methods

This chapter details the implementation procedures, thought processes, challenges, and corresponding solutions. As the foundation of this dissertation, it provides a comprehensive depiction of the entire process, facilitating an easier understanding for the reader and introducing the scientific and technical approach to the research problem and proposed solutions.

3.1 Image Dataset

The images used during the implementation of this tool were retrieved from the Virtual Solar Observatory (VSO) with a specific file format known as FITS. In this section, it will be addressed what is the FITS file format, what kind of images are being downloaded and it will be explained their acquisition source.

VSO (Virtual Solar Observatory)

VSO is a research tool that provides an easy-to-use query interface for accessing solar data and images from a variety of sources, while removing elements that are not considered critical for the user to know (NSO, 2020).

The architecture of the VSO shown in figure 3.1, where it can be seen all the hidden elements that compose this search engine.

A user can perform a query/search for data using the attributes desired such as time, instrument, wavelength, sample time and more receiving the result in a structured response.

Looking at the access options available, the primary user interface available is a web page, however, for this work, an alternative interface was used in order to blend the image retrieval and its processing in just one place. The interface adopted was the one made available by the SunPy python package (SunPy, 2024), which makes an efficient use out of the API made available.

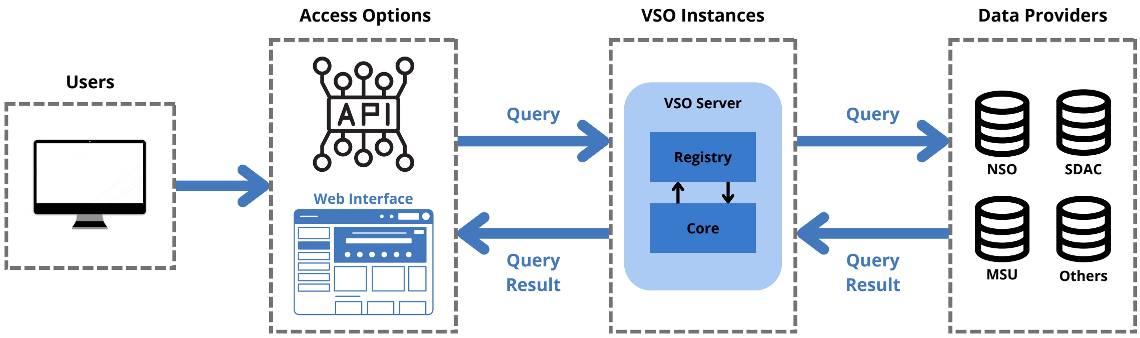

Figure 3.1: Architecture of the VSO. Based on Hill et al. (2009)

FITS File Format

This file format is the most widely used in the astronomy branch for transporting, processing and storing scientific data files.

It consists of one or more Header/Data Units (HDUs) with the first one being known as the primary array. A typical primary array could contain a 1-D spectrum, a 2-D image, or a 3-D data cube and supports different data types such as 1, 2 or 4 byte integers or 4 or 8 byte floating point numbers according to the IEEE representations (NASA, 2014).

In this work the retrieved FITS files contain a primary two dimensional array, given their nature as images.. An example of a file header can be seen in figure 3.2, containing the primary array in the variable named *NAXIS*

```
XTENSION= 'BINTABLE'           / binary table extension
BITPIX  =                    8 / 8-bit bytes
NAXIS   =                    2 / 2-dimensional binary table
NAXIS1  =                    8 / width of table in bytes
NAXIS2  =                 1024 / number of rows in table
PCOUNT  =              1216235 / size of special data area
GCOUNT  =                    1 / one data group (required keyword)
ORIGIN  = 'SDO/JSOC-SDP'       / ORIGIN Location where file made
DATE    = '2023-07-11T15:47:21.000' / [ISO] Date_time of processing; ISO 8601
TELESCOP= 'SDO/AIA '           / For AIA: SDO/AIA
INSTRUME= 'AIA_2   '           / For AIA: AIA_ATA1, AIA_ATA2, AIA_ATA3 or
```

Figure 3.2: Example of a FITS file header

Images

The images are automatically acquired after making a request to the VSO web service with the appropriate parameters, as was indicated in the introduction to this section. They display the entire disk of the Sun captured by the AIA instrument in the 193Å channel, with a resolution of 1024x1024 pixels on the AIA level 1.5, and with a cadence of 12 minutes in between them.

When it comes to the image level, there are three different levels to an AIA image. A level 0 image consists of the raw image. Level 1 means that it was converted from level 0 through processing, removing bad pixels, despiking and flat-fielding. Level 1.5 indicates that the level image was adjusted and centered as well as the limb position established (DeRosa & Slater, 2010).

Figure 3.3 presents an example of a downloaded image, with the 3.3a being the original image and the 3.3b being the content of the FITS file converted directly to a PNG file format.

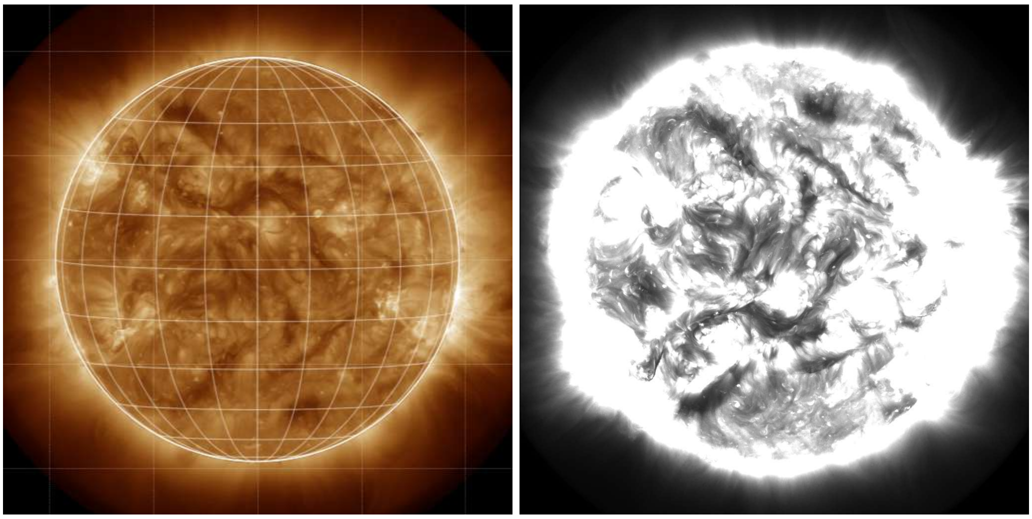

(a) Original image. (b) Image obtained from the FITS file.

Figure 3.3: Example of an original image and a FITS image converted to PNG.

3.2 System Overview

The proposed tool was elaborated with the architecture that is depicted in figure 3.4. This part of the tool was developed using python and runs continuously in the background. It starts by downloading the latest available SDO/AIA images available using the VSO, together with the pre-processing necessary and the retrieval of the Coronal Holes mask. As soon as this step is finished, the images are ready to be used in the CBPs detection phase, where they are detected and classified inside or outside a Coronal Hole, having their data stored in a database. After all CBPs in that image have been detected, they are evaluated so that they can be tracked over various images. Lastly, the rotation of the Sun is calculated, with the aid of the information stored in the database, and the results are displayed in a nearly real-time website.

3.2.1 Image Acquisition

The image acquisition is rather straight forward as the SunPy python library (SunPy, 2024) already offers intuitive functions that can search and download solar images from VSO.

The method used to search for the images is *Fido.search()* where it is necessary to define the start and end time for the search, the instrument that captured the images,

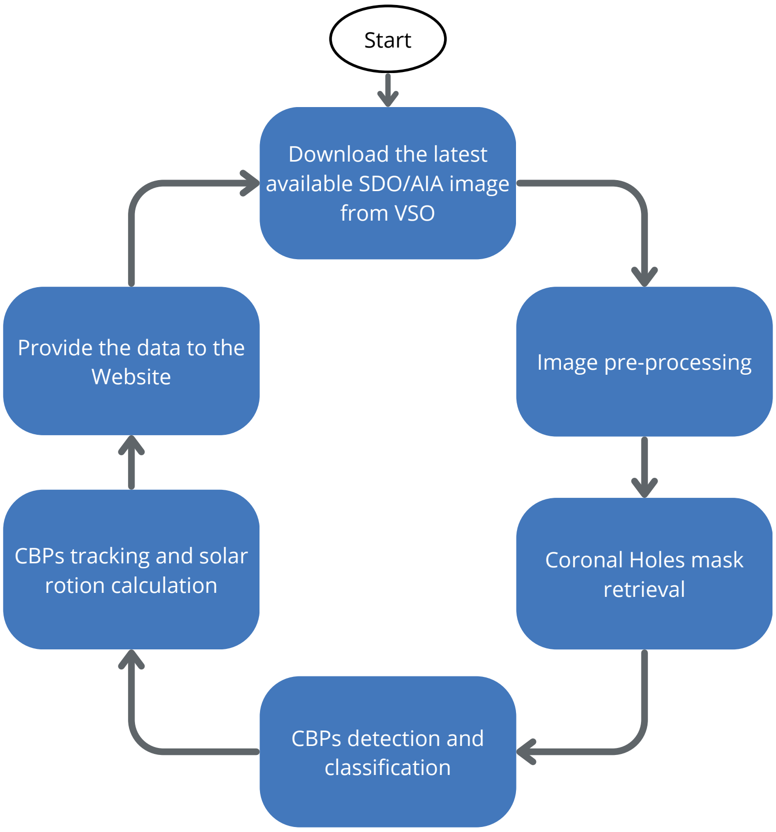

Figure 3.4: Flowchart of the tool's sequential behaviour

the wavelength of the images and the sampling time. That method then returns a list of images that were found and, with that, it is possible to download them to a specified path using the *Fido.fetch()* method. The downloaded images come in a 1024x1024 pixels low resolution as these are the ones that are made available one to two hours after the capture. The high resolution images (4096x4096) are only available 4 to 5 days after the capture.

To avoid overloading the servers with too many requests, each image is only downloaded after the previous one has finished being processed and used for detection and tracking.

3.2.2 Pre-Processing

In order to achieve optimal results, it was necessary to process the images so that the CBPs became clear for the tool to detect them.

The first step was to correct the effect of the instrument using the Point Spread Function (PSF) provided by Poduval et al. (2013). This consists in a deconvolution, which removes the degradation of the image, enhancing the contrast, followed by a normalisation between 0 and 1 using the min-max method.

Secondly, an 180 degrees rotation was performed because the image was upside down, followed by an horizontal flip, as well as the resampling to 4096x4096 pixels.

The resampling is performed to obtain more CBPs detections, since Pires (2018) pointed that the original image resolution achieved less than 50% of detected CBPs when comparing with the resampled image. The high resolution images were also not considered because they are only available 4 to 5 days after the capture and present less detections than the resampled image.

At this point, an *Active Regions mask* is achieved for future use (during the detection phase). This mask is the same as the one mentioned in Coelho (2017) and Dorotovič et al. (2018) and it consists of 15 erosions and dilations to clear small manifestations, followed by 5 dilations to highlight Active Regions and possibly dismiss CBPs on Active Regions borders. An example of a mask is displayed in figure 3.5.

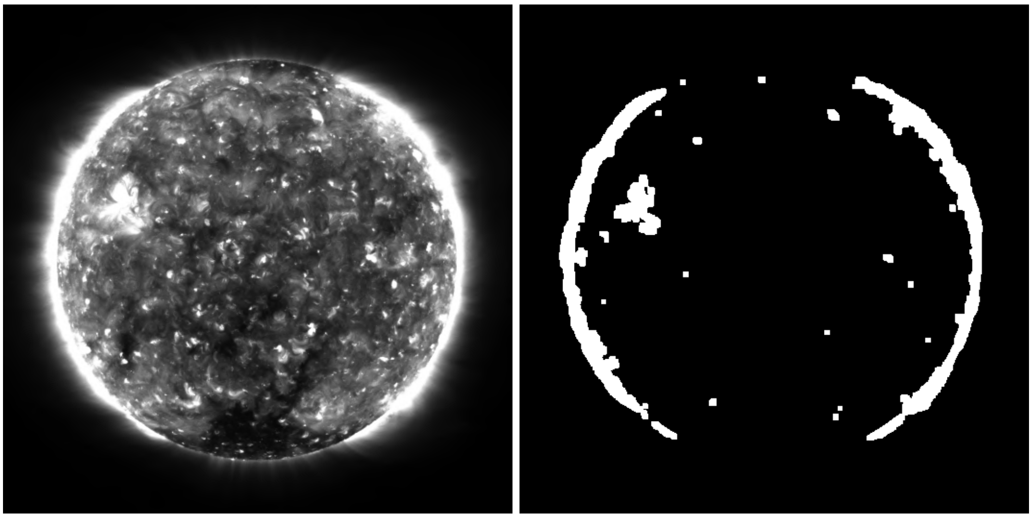

(a) Original image. (b) Active Regions mask.

Figure 3.5: Example of an Active Regions mask using a Sun image from 2019.

As the final preparation, it was taken into consideration the study performed by Carreira (2020) regarding the intensity normalisation on different images that present different stages of the Sun's cycle. This process consists in applying a multiplication factor to the image to enhance the contrast, meaning that bright colored pixels become brighter while darkest pixels remain dark.

Carreira (2020) pointed that, when using a constant multiplication factor of 10, while the Sun was very active the image would become very bright but, if the Sun was quiet, the image would be just as desired as it is shown on the top row of figure 3.6.

With that in mind, the multiplying factor is calculated in an adaptive way, using the weighted average of the image histogram between the intensity values of 50 and 200, in order to not consider the high amount of black pixels outside the solar disk. That translated by the following equation:

$$avg_w = \frac{\sum_{i=50}^{200}(i \times hist(i))}{\sum_{i=50}^{200} hist(i)}. \tag{3.1}$$

After the study of various weighted averages of 15 different images of the Sun, it was found a linear regression that ensures the best multiplying factor to achieve the desired contrast. The equation of that regression is presented as

$$mul_{value} = -0.21 \times avg_w + 23.33. \tag{3.2}$$

On the bottom row of figure 3.6, it is possible to see the result of the adaptive factor.

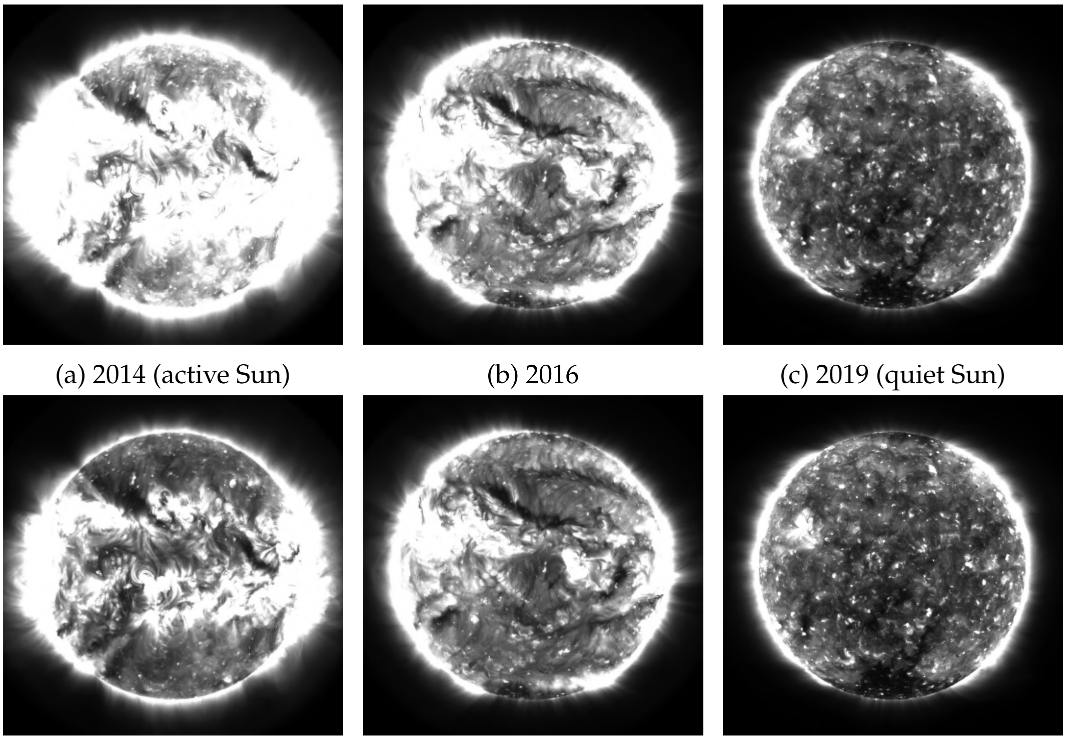

(a) 2014 (active Sun) (b) 2016 (c) 2019 (quiet Sun)

(d) 2014 (active Sun) (e) 2016 (f) 2019 (quiet Sun)

Figure 3.6: Image intensity normalisation. Top row presents the normalisation using a fixed value of 10, while the bottom row shows the normalisation done in the adaptive way.

With the images normalised in the adaptive way, it is possible to perform the detection of the CBPs as it was intended, since they are more evident.

3.2.3 Coronal Holes Mask

An interesting aspect concerning CBPs involves the potential study and comparison between those found within Coronal Holes and those located outside.

In order to provide this useful data, it is necessary to find the location of the Coronal holes present in the images. Carreira (2020) in her master thesis, developed a method for obtaining the Coronal Holes mask, which was possible to be replicated in this work.

The Coronal Hole mask is obtained by initially retrieving a mask of the area of the Sun (Sun mask) in white. This is important as the area of the Sun depicted in each image is different due to the orbit of the SDO. Secondly, a thresholding function with threshold equal to 30 is applied, and then a *bitwise AND* function between the Sun mask and the thresholded image, with the purpose of emphasizing the location of the Coronal Holes.

Finally, some post processing is done to eliminate imperfections when it comes to the Coronal Holes, caused by CBPs within them, ensuring the continuity in their area.

With this process, it is possible to obtain the Coronal Holes mask shown in image 3.7.

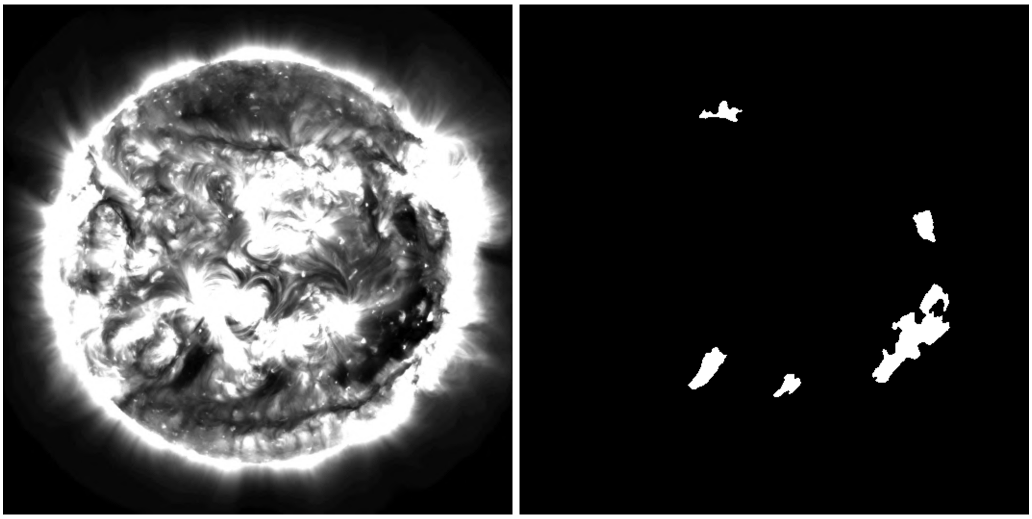

(a) Original image. (b) Coronal Holes mask.

Figure 3.7: Example of a Coronal Holes mask using a Sun image from 2023.

3.2.4 CBP Detection

For the detection step, a new specific image processing process was implemented. This proposed method uses the *matchTemplate* function from the *OpenCV* library as its main algorithm.

The *matchTemplate* function is a powerful tool for template matching in computer vision applications. It allows users to compare an input image with a given template and find the best matching region within the image. This method was chosen because it presents good results when searching for objects with a regular shape, in the sense that their shape and size do not suffer significant changes through time. CBPs are the perfect candidates for *matchTemplate* since they present a usually round shape and have known size.

To use this method, a python function called *findTemplate* was created which receives the defined template. For this, a CBP that is more or less round and bright was selected from a previously processed image. This template is 40x40 pixels originally and it is demonstrated in figure 3.8. The criteria for choosing this template will be further assessed in Chapter 4.

Having the template defined, the function will do a sliding window analysis through the Sun's full disk input image and compare the overlapped patches of the same template image size using a defined comparison process. OpenCV provides six comparison metrics: Sum of Square Differences (SSD), Cross Correlation (CC), Mean Shifted Cross Correlation (CCOEFF) and their normalised version.

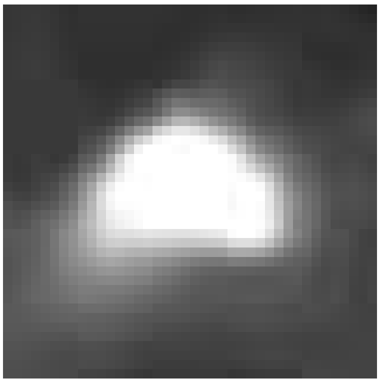

Figure 3.8: Template used for template matching.

SSD computes the sum of square differences where it penalises the values that are further way from the required so, if the data has values that are prone to be very distant, the values will be very high. However, when comparing two identical images, the value will be 0 or close to it. The CC mode simply multiplies the template with the patch together. It is possible to imagine that if the patch an the template are perfectly aligned, the result will be the square of the template. On the other hand, if they are not, then the product will be smaller than the square. This method is not ideal because changes in image overall intensity will have different CC results, even if the shape is the correct one. To solve the problem with the white patches of the last mode, CCOEFF simply subtracts the mean before comparing the images. This way, images that are a little bit shifted have the same correlation as those as perfectly aligned. The normalised versions, are normalised using the standard deviation (square root of the sum of squared differences from the mean).

Taking this into account, the best mode to be used was the CCOEFF normalised, since the images used contain a lot of bright patches and was proven to be reliable in numerous examples, such as the OpenCV documentation example in this matter. This method normalises the comparison results to a range between 0 and 1, with closer values to 1 indicating better matching results. In this work, after the application of the function, every pixel that has a value above 0.8 is counted as a correct matched CBP.

The selection of the threshold value was done empirically based on the number of detected CBPs from an image of 2019 and another from 2023. Table 3.1 demonstrates the values of the total objects detected, the correctly identified CBPs (True Positives, TP), the incorrectly identified CBPs (False Positives, FP), and the percentage error accuracy value.

The percentage error is computed using the following equation:

$$\frac{|TP - Total|}{Total} \times 100, \tag{3.3}$$

meaning that lower the error, better accuracy.

	2023			2019		
Threshold	0,75	0,8	0,85	0,75	0,8	0,85
False Positives	74	23	8	50	1	0
True Positives	141	101	41	129	118	42
Total Detected	215	124	49	179	119	42
Percentage Error (%)	34,4	18,5	16,3	27,9	0,8	0

Table 3.1: Comparison of the different thresholds performances on CBPs detection.

It is noticeable that the threshold of 0.85 did not meet the necessary criteria for being selected since it only detected low amounts of CBPs, even though its low error percentage. The threshold value of 0.75 presented high values of detected objects, however its accuracy shows values that are not ideal given the amount of False Positives detected. Finally, the threshold of 0.8 presents the better results of the three, managing to achieve a good accuracy and a good amount of detected CBPs.

The CBPs observed in the solar corona possess shapes that, while resembling circles, deviate from perfect circularity, meaning that they do not present infinite rotational symmetry. Consequently, it is likely to encounter CBPs with similar shapes but different orientations or sizes, in relation to the shape of the CBP in the template. As a result, applying the *findTemplate* function once did not yield the optimal precision in detecting the CBPs, therefore the original template undergoes three rotations (90, 180, and 270 degrees) at its original size (40x40 pixels). It was chosen three rotations because CBPs are often closer to a semi-circle and four different angles are enough to satisfy most of their irregularities. Subsequently, the same process is repeated after the resizing of the template by 1.5 and 2. In summary, this process is repeated 12 times in total (4 times for each size) to comprehensively detect all CBPs in the image.

Since the result of using this function is an array comprising the coordinates of the boxes where the CBPs were found, various boxes are originated regarding the same CBP. To tackle this problem, a technique called Non Maximum Suppression (NMS) was implemented.

NMS serves as a post-processing technique aimed at eliminating redundant and overlapping detections, ensuring a more concise and efficient output. This method assesses the overlap between each bounding box, discarding the previous if the shared area exceeds 40%. If the box sizes are different the biggest one will prevail. As a result, a single bounding box per CBP detection is retained. By integrating NMS into the function, it will enhance the accuracy of CBP identification and localisation while minimising redundancy.

The last stage of the detection process involves filtering out CBPs that were detected near the Solar limb, specifically those situated over 0.85 of the Sun radius, as they tend to be more imprecise (Sudar et al., 2015). Additionally, CBPs located in Active Regions are excluded using the mask obtained during the pre-processing phase (see 3.2.2). It is also determined whether the CBP is located inside or outside of a Coronal Hole.

The remaining valid CBPs have their brightest point and centroid coordinates in pixels stored in a database, as well as a Boolean value regarding their position, inside or outside Coronal Holes for later use. Ultimately, it is the brightest point that will be used as it presented less fluctuations in the values, however the centroid was also considered a possibility so it was stored for comparison.

3.2.5 Solar Rotation Calculations

The calculations that are used to determine the rotation velocity of each individual CBP when tracking them, are based on the relationship between the synodic and sidereal velocities using the research of Skokić et al. (2014) as a basis.

The synodic velocity refers to the relative motion between two celestial bodies, such as the Earth or a planet, while the sidereal velocity is the actual orbital velocity of a celestial body with respect to distant stars.

The equation of the synodic rotacional velocity is given by the following expression,

$$\omega_{syn} = \frac{N\sum_{i=1}^{N} l_i t_i - \sum_{i=1}^{N} l_i \sum_{i=1}^{N} t_i}{N\sum_{i=1}^{N} t_i^2 - (\sum_{i=1}^{N} t_i)^2}, \tag{3.4}$$

where N is number of detections, l_i is the longitude, also known as Central Meridian Distance (CMD), and t_i is the lifetime of each measurement for a single CBP (Sudar et al., 2015).

The sidereal velocity is the most important one to have available when conducting a solar rotation study. To transform the synodic velocity to the sidereal, the true value of velocity, it is necessary to use the Eq. (7) of Skokić et al. (2014). It is described as follows,

$$\omega_{sid} = \omega_{syn} + \omega_{Earth}\frac{\cos^2\Psi}{\cos i}, \tag{3.5}$$

where Ψ is angle between geocentric north and solar north as seen from Earth, i is the the true obliquity of the ecliptic and ω_{Earth} represents the instantaneous orbital angular velocity of Earth given by the following equation,

$$\omega_{Earth} = \frac{\overline{\omega}_{Earth}}{r^2}, \tag{3.6}$$

where r is the distance between Earth and the Sun and $\overline{\omega}_{Earth}$ is the average orbital angular velocity of Earth defined by the value of $0.9856°/day$.

It is important to mention that the values of Ψ, i and r are all obtained using the SunPy library (SunPy, 2024) directly through its available methods, considering that they change over the year due to the position of Earth relative to the Sun.

3.2.6 CBP Tracking

Concerning the tracking, it was necessary to create a function that could access the stored data regarding all the detected CBPs and create a relation between the newest detected and the ones detected in previous images. The result was a function based on the work performed by Pires (2018) where some of the calculations were improved by removing redundant steps, corrected the constraints for the detection on an active CBP, and updated the functions used to obtain the solar constant values.

Figure 3.9 presents a flowchart that depicts the tracking of CBPs work.

The method's initial phase is to retrieve data on newly found CBPs as well as those that are currently active, so two queries are executed, respectively. Using the output of the first query, the coordinates of the newly found CBPs are converted from pixels to heliographic coordinates, which is the Sun position coordinates system. The second query already returns the active CBPs location coordinates both in pixels and heliographic. This conversion will be useful in the next step.

In order to increase the accuracy of the tracking results, there is a two factor verification using two distance measures, pixels and heliographic degrees, to track the CBPs. The first method uses pixel coordinates to determine whether the CBP is new or one already active. It verifies if the distance, from the detected CBP to the active, is below 5 pixels in the Y coordinate and if it is below 20 pixels in the X coordinate.

The second factor is only used if the detected CBP is considered active, meaning that it passed the first verification. This second verification uses the heliographic coordinates. If the active CBP was last detected less than 30 minutes before, it is considered a maximum distance between the detected CBP and the active one of 0.4°, or, if it was last detected less than 60 minutes before, the maximum distance is 0.8°.

It is important to mention that all the tracked CBPs are limited to ±58° in latitude and longitude, meaning that only the ones inside 85% of the Solar radius are considered.

Anytime a new CBP has been identified, the database is updated with the new CBP's location in pixels and heliographic coordinates, along with the time and date of detection. On the other hand, if the CBP is active, its rotation speed, lifetime, number of detections, and last location values are updated.

Further filtering is carried out after iterating over each newly discovered CBP. Every CBP that has not been detected for more than an hour is updated to its not active state. CBPs that are not active and have less than ten detections are removed, as are those whose rotational velocities are greater than 19º per day or less than 8º per day.

All the constraints mentioned above are based on Sudar et al. (2015) work, where it was affirmed that the maximum travel of a CBP is approximately 19° per day, meaning 0.8° per hour, and that using CBPs from positions higher than ±58° would cause higher imprecision.

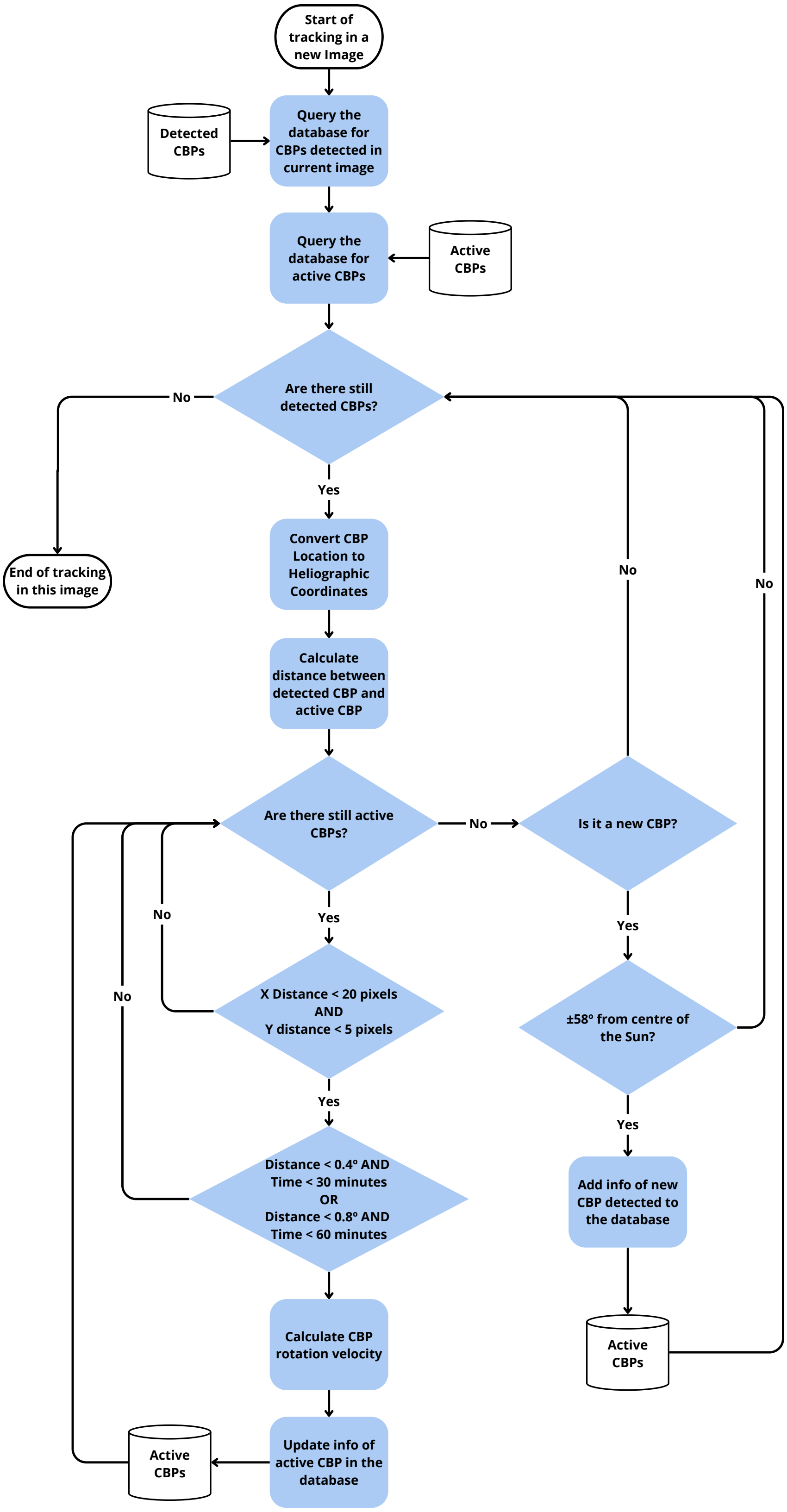

Figure 3.9: CBPs tracking flowchart.

3.2.7 Database Structure

The database created for use in this tool consists of three distinct tables. The tables can be seen in figure 3.10.

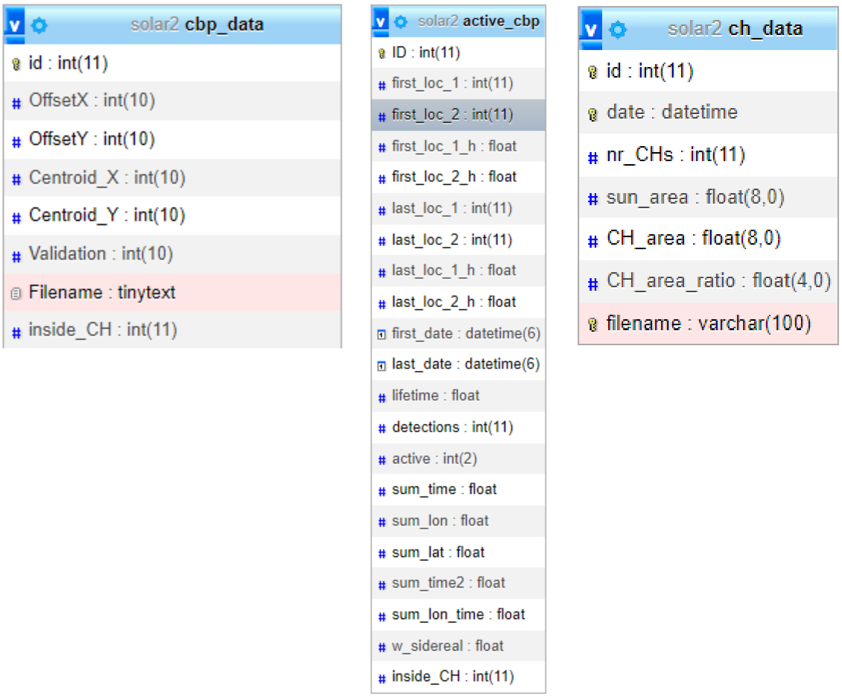

Figure 3.10: Structure of the Database.

The first table is the *cbp_data* table, where information about the detected CBPs in each image is stored. Whenever a new image is processed using the detection algorithm, this table records details such as the location of the CBP's centroid, its position inside or outside a Coronal Hole, and the filename from where it was found.

Then there is a table named *active_cbp*, which is where the data regarding the tracking of active CBPs is organised. Here each row presents information about a different active CBP. Every row provides the location (in pixels and heliographic coordinates) and the date from where it was first and last identified, as well as details about its lifetime, detections, and position inside or outside a Coronal Hole. Additionally, the table includes calculated values used for tracking, such as those required for determining the rotational speed along with the rotational speed value.

The last table is the *ch_data* table where it is stored information about the Coronal Holes. Each row consists of the date of the image, the number of Coronal Holes present, the ratio of area covered by Coronal Holes and the filename of the Coronal Holes mask.

3.2.8 Website Content and Development

The website produced is an extension to the website created in Pires (2018) and Pires et al. (2019), where some new features were added combining new information from works previously developed in NOVA University Lisbon (NOVA). Those works are the ones already mentioned such as Carreira (2020) and Pires (2018).

The web pages were developed using *HTML* in conjunction with *CSS* and *JavaScript* for the front-end and *PHP* for the back-end side, while being supported by a *MySQL* database where all the CBPs data is stored. The interface of the website is composed by four different pages: *Now*, *Archive*, *Coronal Holes* and *About*.

The website makes available nearly real time information about CBPs and Coronal Holes. It also provides data history, being possible to select the data intervals, and a section dedicated to the Coronal Holes analysis. The main addition and contribution to the website were: the upgraded layout, plots with a faster update rate and new best-fitting curves, as well as the new page related to the Coronal Holes information.

For the development of the *Now* page, the *Archive* and the *Coronal Holes* page, three pairs of files were created, each pair comprising a front-end file and a corresponding back-end file. These files are intentionally paired to establish a connection or interaction between the front-end and back-end components.

All the back-end files are mainly dedicated to perform queries to the database and store their result in dedicated variables, as a way to display the information in the website. Nevertheless, they were used for handling other requests that will be explained in this section.

Page *Now*

On the *Now* page, it is located the most recent and updated information about the tracked CBPs. Its layout can be observed from figure 3.11 to 3.13.

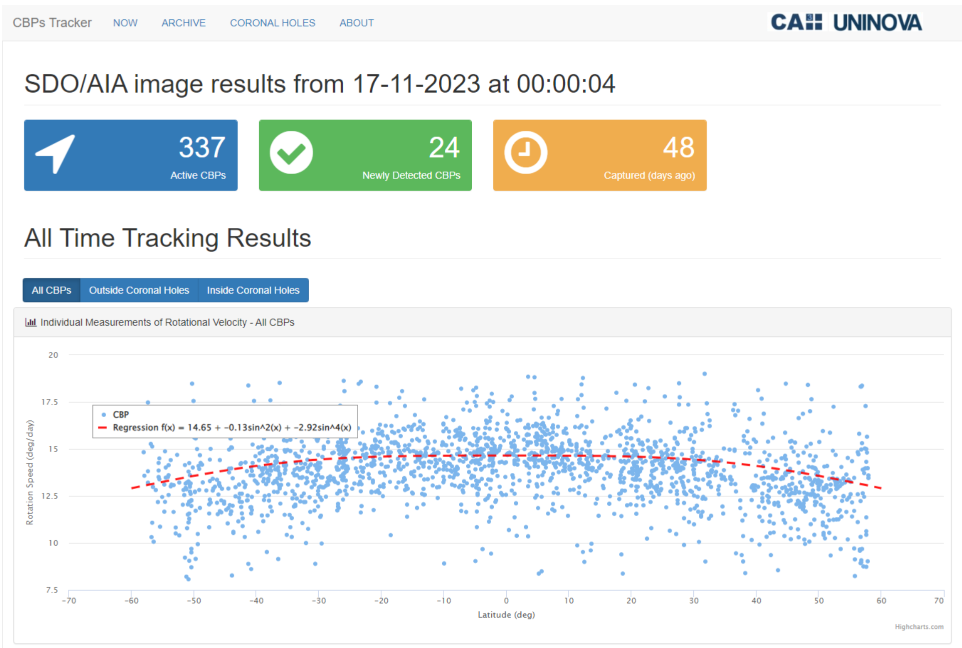

Figure 3.11: Last image results and scatter plot of the rotational speed over the latitude.

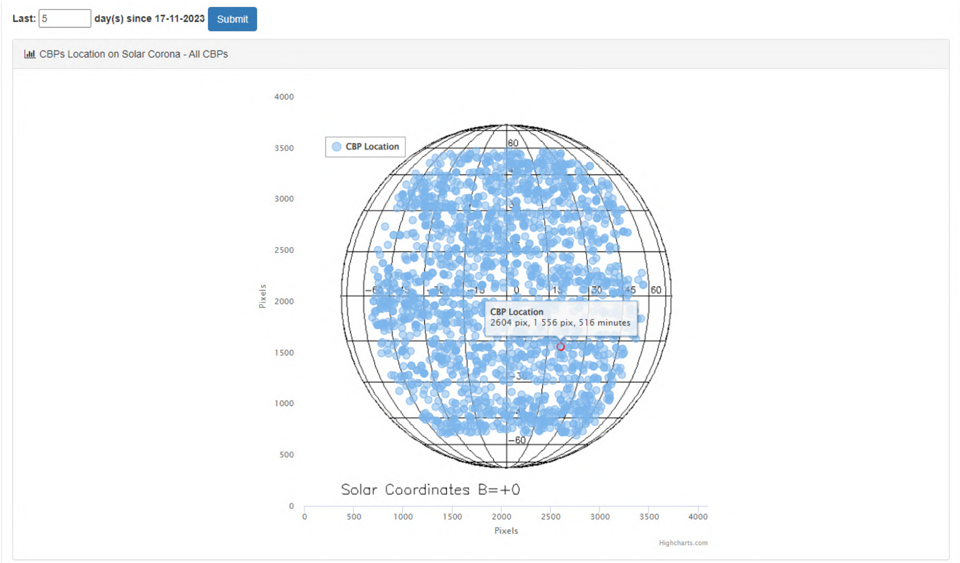

Figure 3.12: Scatter plot of the location of the CBPs on the solar corona.

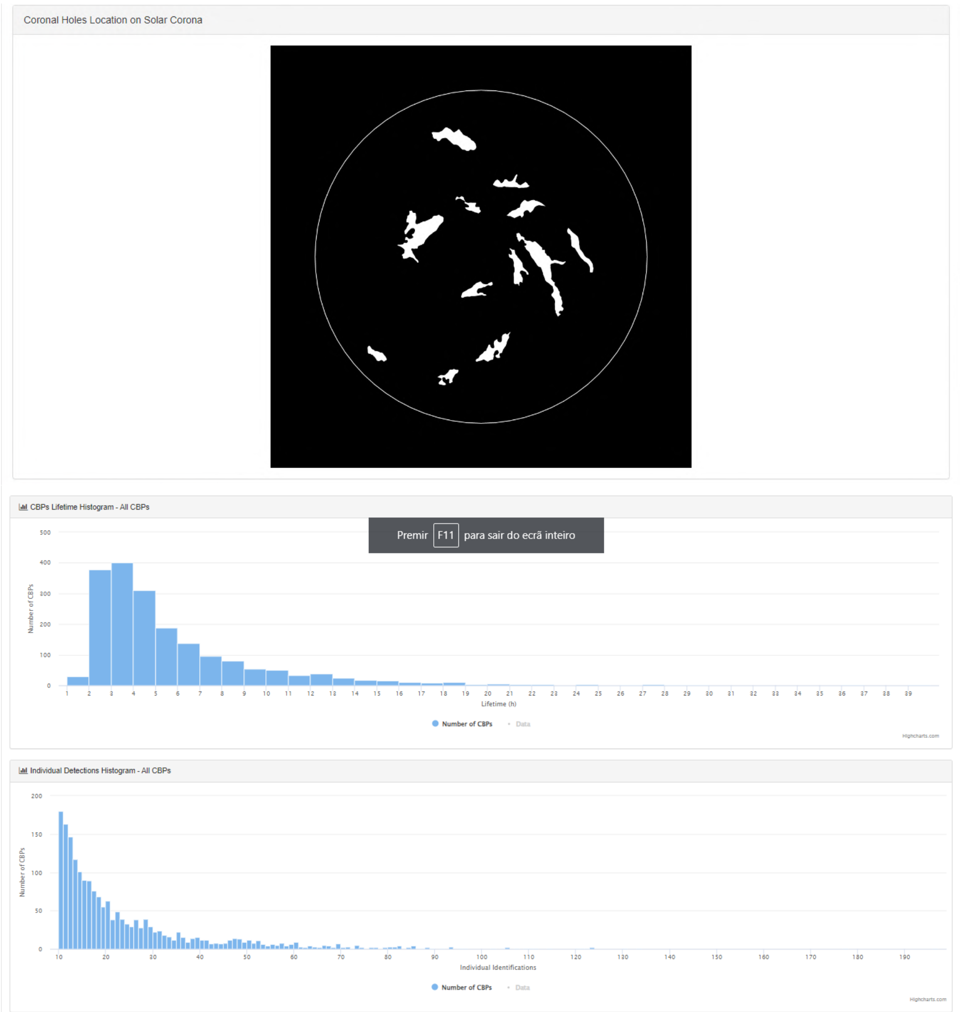

Figure 3.13: Coronal Holes image, lifetime and individual detections histograms.

At the top, the results of the last image received from detection and tracking are displayed. For that, three data panels are created. Each panel features an icon, a numerical value, and a description. The first panel communicates the number of active CBPs, the second panel reveals the count of newly detected CBPs and the third panel dynamically computes and exhibits the time difference since the last capture, presenting this information in terms of minutes, hours, or days. The data panels were created using Bootstrap's grid system (https://getbootstrap.com/). As they all provide different information, they all have respective queries allocated.

Below this dashboard, under the title "Updated Tracking Results" are the tracking results of all the CBPs in the database. There are also three buttons that control the exhibited data. These radio buttons, from the Bootstrap library, allow the user to select the information they want to see: all CBPs, those outside the Coronal Holes, or those inside them. When a button is selected, a button listener created in *Javascript* activates a function. This function updates all the charts with the selected information using the appropriate methods and the variables resulting from the back-end queries.

The page features four graphics and one image. Firstly, a scatter plot of the rotational speed versus the latitude is presented. Following that, there is a scatter plot of the location of the CBPs on the solar corona. Users have the option to customize the time range of this plot by selecting the number of days before the date of the last processed image. Next, an image of the Coronal Holes in the last processed solar image is displayed. At the bottom of the page, there are two histograms: one presenting the lifetime of the CBPs and the other displaying all the individual detections.

All the plots on the website use the *Highcharts* chart library for displaying results. When it comes to the lifetime histogram and the individual detection histogram, it was used the *Highcharts* function for histograms and the appropriate back-end variable corresponding to the intended data portrayal.

In the case of the scatter plot depicting rotation speed versus latitude, it was also employed the *Highcharts* chart function and correct data. However, an additional step was required to obtain the best-fitting curve for the plot in near real time. On the back-end, a specific query was executed to then obtain the trendline coefficients of the correlation between rotational speed and the sine of the latitude. This was achieved with the aid of a polynomial regression library (https://polynomialregression.drque.net/). Subsequently, the values of the curve were calculated, stored and displayed in the scatter plot made available to the user.

For the CBPs location plot, which has the option of deciding the time span of data visualisation, it was necessary to change the query for it dynamically, since the location information comes directly from the database. For that purpose, it was implemented a *Javascript* function that is triggered whenever the user decides to change the time interval. This latter performs a *POST* request to the back-end sending the range of days the user wants the data to be displayed. The back-end code handles this request by running a query with the new time range and sending back the new data to be displayed in the front-end.

Lastly, the image of the Coronal Holes on this page is obtained by querying the database for the filename of the image corresponding to the date of the last processed image.

Page *Archive*

The layout of the *Archive* page mirrors page *Now*, however, two new tables are introduced. The page particularities are shown in figure 3.14 and 3.15.

At the top of the page, there is an *HTML* form where users can input the initial and end dates of the time interval for displaying data. When the user submits these values, the back-end handles the request and adjusts all queries to match the specified time interval, ensuring the accurate display of data.

The first table provides information about the total number of CBPs within the specified interval and, at the bottom of the page, the other table offers details on their date of identification, position, lifetime, and rotational speed. Notably, with the aid of an *HTML* library (https://datatables.net/), the latter table provides the functionality to download its content in popular formats such as *PDF* or *Excel*.

All the plots and histograms in this page were coded in the same way as the first page, even though the location plot now has the time interval restricted by the form presented earlier. This means that the time span chosen is used as a parameter of the query for obtaining the location results.

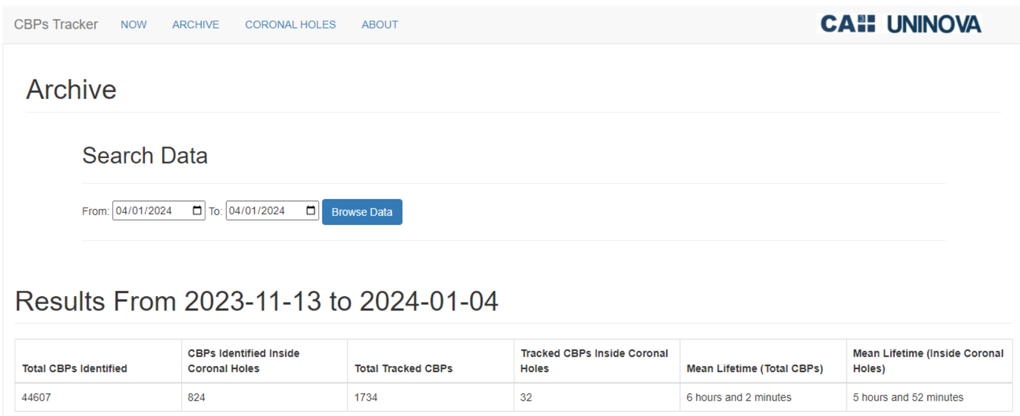

Figure 3.14: Date form to chose a time interval and first info table.

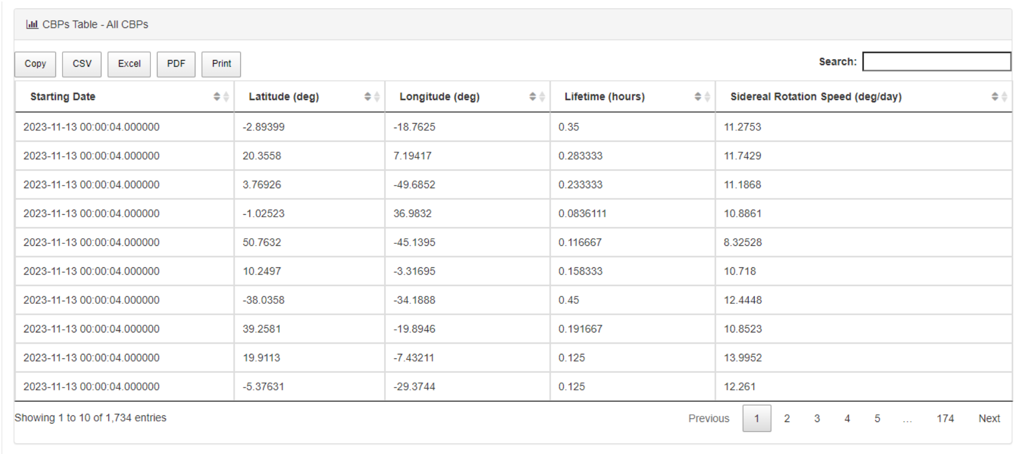

CBPs Table - All CBPs

Copy CSV Excel PDF Print

Search:

Starting Date	Latitude (deg)	Longitude (deg)	Lifetime (hours)	Sidereal Rotation Speed (deg/day)
2023-11-13 00:00:04.000000	-2.89399	-18.7625	0.35	11.2753
2023-11-13 00:00:04.000000	20.3558	7.19417	0.283333	11.7429
2023-11-13 00:00:04.000000	3.76926	-49.6852	0.233333	11.1868
2023-11-13 00:00:04.000000	-1.02523	36.9832	0.0836111	10.8861
2023-11-13 00:00:04.000000	50.7632	-45.1395	0.116667	8.32528
2023-11-13 00:00:04.000000	10.2497	-3.31695	0.158333	10.718
2023-11-13 00:00:04.000000	-38.0358	-34.1888	0.45	12.4448
2023-11-13 00:00:04.000000	39.2581	-19.8946	0.191667	10.8523
2023-11-13 00:00:04.000000	19.9113	-7.43211	0.125	13.9952
2023-11-13 00:00:04.000000	-5.37631	-29.3744	0.125	12.261

Showing 1 to 10 of 1,734 entries

Previous 1 2 3 4 5 ... 174 Next

Figure 3.15: Second info table that allows download.

Page *Coronal Holes*

The *Coronal Holes* page was designed to offer a comprehensive view of the Coronal Holes' evolution over the preceding full day, calculated from the date of the latest analysed image. This page provides users with an interactive slideshow featuring up to 120 images (spanning a 24-hour period), while being possible to access the closest original solar image to the one presented in the slideshow. The slideshow is demonstrated in figure 3.16 and the corresponding solar image in figure 3.17.

The slideshow consists of a container where the images are displayed. The *HTML* code for the slides is dynamically generated based on an array containing information about Coronal Holes images. This array is obtained from the back-end using a query that selects all the content from the last 120 rows of the *ch_data* table from the database.

The navigation process is achieved using *Javascript*. It consists in displaying the desired slide with the aid of an index that holds the value of the current image being displayed. When the 'next'/'previous' arrow icon is pressed, the function is called, the index is increased/decreased and the new image is displayed.

Above the slideshow, there is a clickable link with the phrase "Click to open the closest image to the original". To reduce server file storage space, the original images from which the masks are retrieved are not saved. Instead, an online directory provided by the NASA/SDO website is utilised to access older images. Since they do not store every image captured every minute, a script was developed to search the directory and find the closest image.

When the link is pressed, a *POST* is triggered request to the back-end sending the date of the image as parameter. In the back-end script, the request handler then navigates to the assets path of the SDO, retrieves all filenames, and stores them in an array. Applying a filter based on the known filename pattern (YYYYMMDD_HHMMSS_Resolution_Wavelength), the script refines the array by considering the date, resolution, and wavelength. The time in the filename is treated as a ' * ' to include all files from that date. The filtered results are stored in another array.

In the final step, the script iterates through the filtered array, focusing solely on the time part of each filename. It calculates which file has the nearest timestamp to the original, returning the corresponding filename in the *POST* response. After receiving the response, the front-end side will open a new tab on the browser displaying the image from the SDO assets directory.

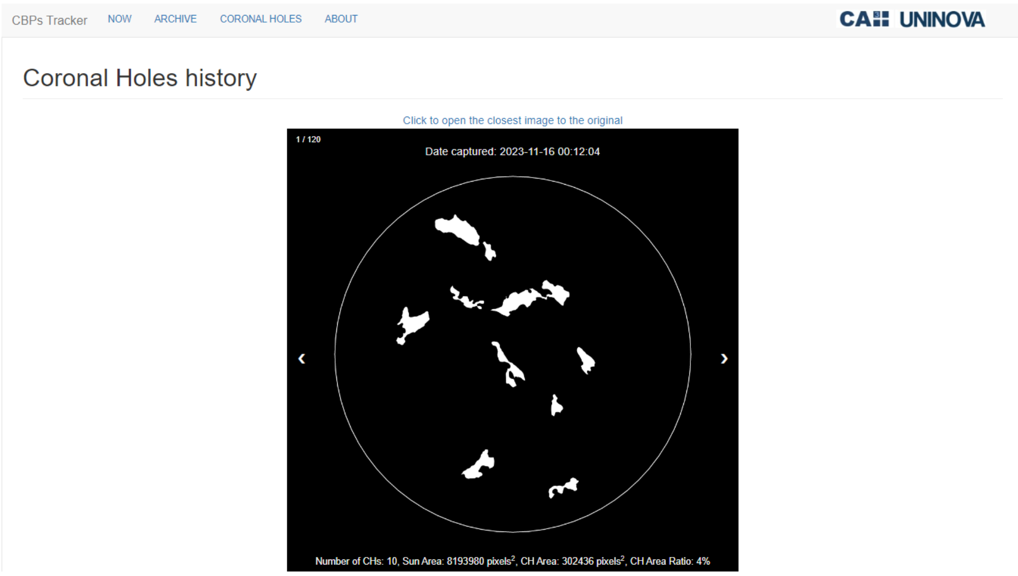

Figure 3.16: Coronal Holes page previewing the slideshow.

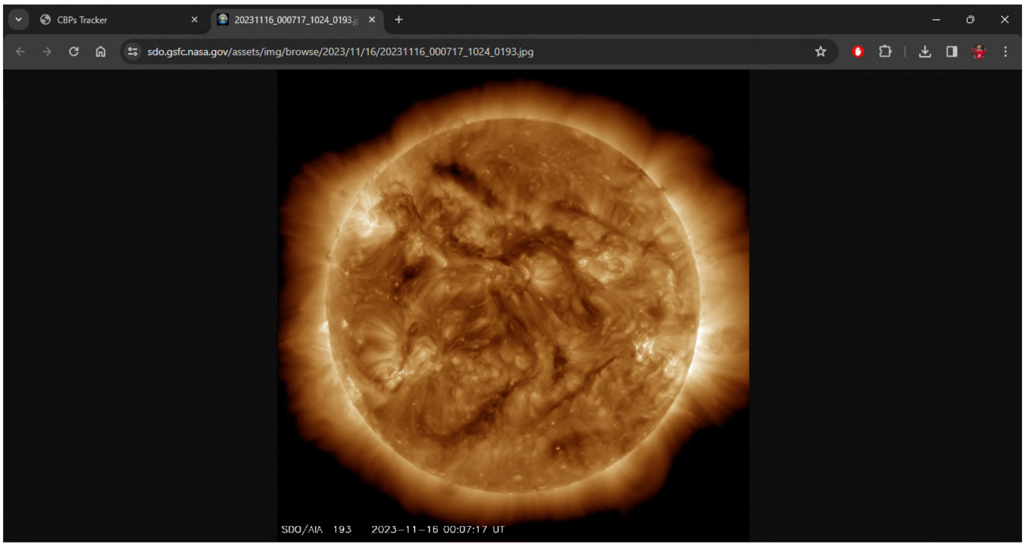

Figure 3.17: Solar image obtained using the clickable link (SDO, 2023c).

Page *About*

This page is where is written some information about where are the images used for tracking from, what does the website consist of and the contributors of the project. Its content is shown in figure 3.18.

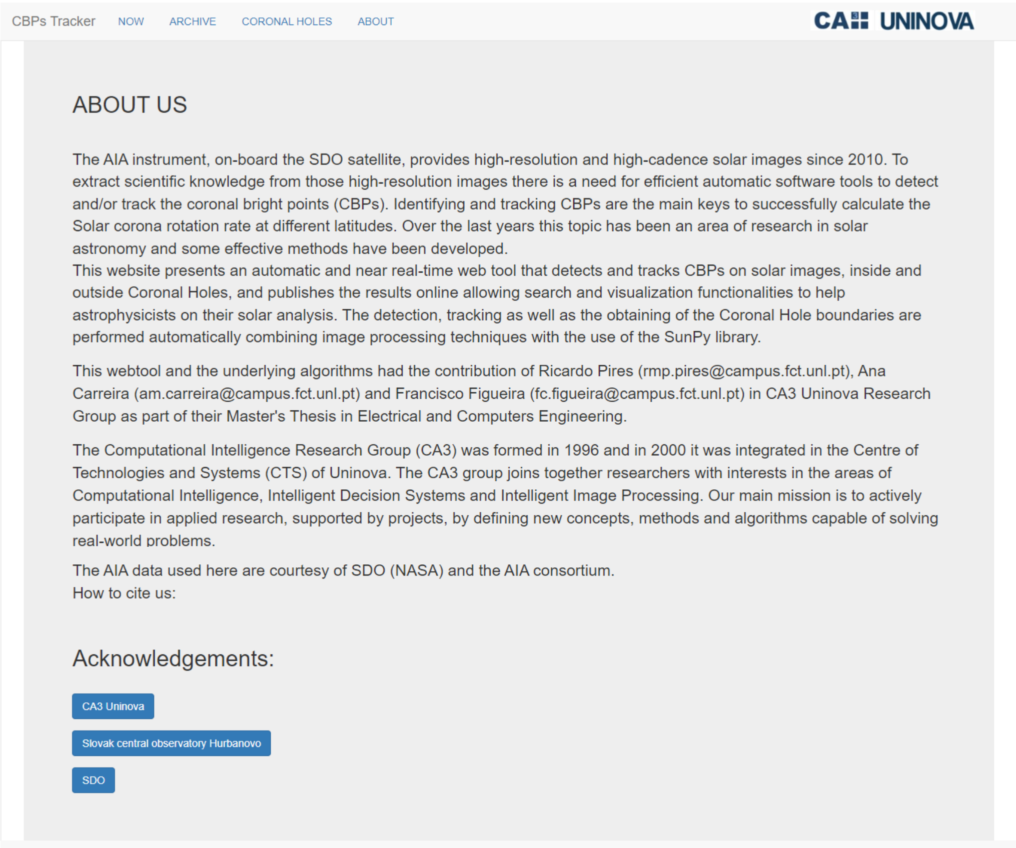

Figure 3.18: Contents of the *About* page.

4 Results Assessment

The chapter is split into two main sections. The initial part covers the findings related to the detection of CBPs, while the latter addresses tracking and solar calculations. In the section about tracking and solar rotation calculations, the results will be presented for the same two time intervals discussed in the previous section. This will include findings related to the number of tracked CBPs and their velocities. Additionally, a comparison will be provided between the results from the two time intervals using the Match Template approach, along with a comparison to other studies conducted on solar differential rotation and discussed the effect of the number of CBPs detections on the tracking results.

4.1 Detection Results

The detection results will first explore the reasons for selecting the template, followed by a comparison between the method utilised in this study, Match Template, and another method commonly employed in this domain, GPL. Finally, the outcomes obtained over two distinct time intervals, one in 2019 and the other in 2023, will be presented.

4.1.1 Template Selection

When using the *Match Template* function for the CBPs detection, it is necessary to choose the most adequate template in order to obtain the best possible results. Therefore, three different templates were tested and compared.

Two of these templates were retrieved directly from an already processed image and the third one was artificially made in a computer design program. Figure 4.1 illustrates them.

With the aid of figure 4.2, it is possible to see the performance of each template in a solar image that portrays very high solar activity. It is noticeable that the first and third templates consider less valid CBPs when comparing with the second template. When

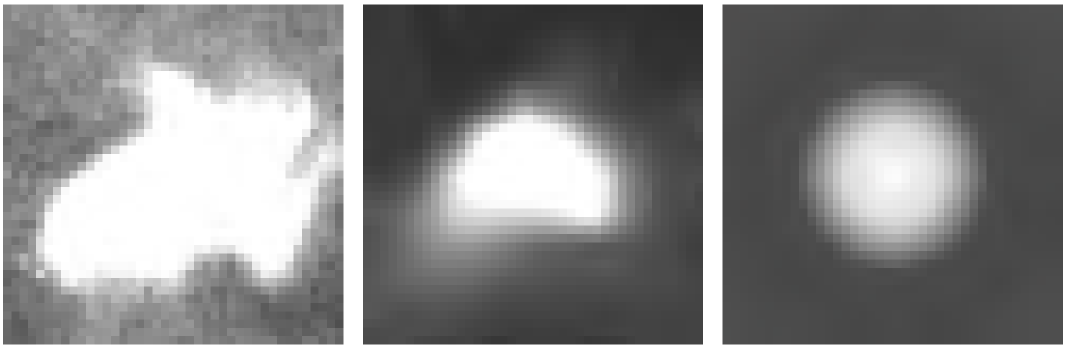

(a) Template 1. (b) Template 2. (c) Template 3.

Figure 4.1: Templates used for CBPs detection (Not in scale, actual size 40x40 pixels).

taking a closer look into the results, template 1 and 3 show similar outputs with 46 and 55 valid CBPs, respectively, and the second template 154.

With this in mind another result was obtained using an image from a year that the Sun was on a low solar activity state. Those results are shown in figure 4.3

Considering the results of both images, it becomes clear that, although template 1 performs adequately in a high solar activity image, it does not meet the expectations in a low activity setting, so, for that reason, this was not chosen as the definitive template.

Template 2 achieves good results in both images, nonetheless, it marks some false positives as valid CBPs mainly in the high solar activity image. It is important to note that the rotation applied on this template can help with the results obtained, meaning that it adjusts better to the various kinds of CBPs.

When it comes to the third template, it can be said that performs well on both occasions, however, the second template achieves better results. The most probable reason for the third template not achieving better results is that its form is too regular and, as it can be perceived, CBPs come in all forms and shapes.

With the arguments presented, the template chosen to be the one used was template 2 because, even though it may classify some false positives as CBPs, it can validate more true positives out of all templates.

Concerning the matter of false positives in CBPs, tracking will prove to be a valuable tool in addressing this issue. The false positives will most probably not be detected in the following images, therefore rejected by the tracking if the number of detections is lower than a threshold.

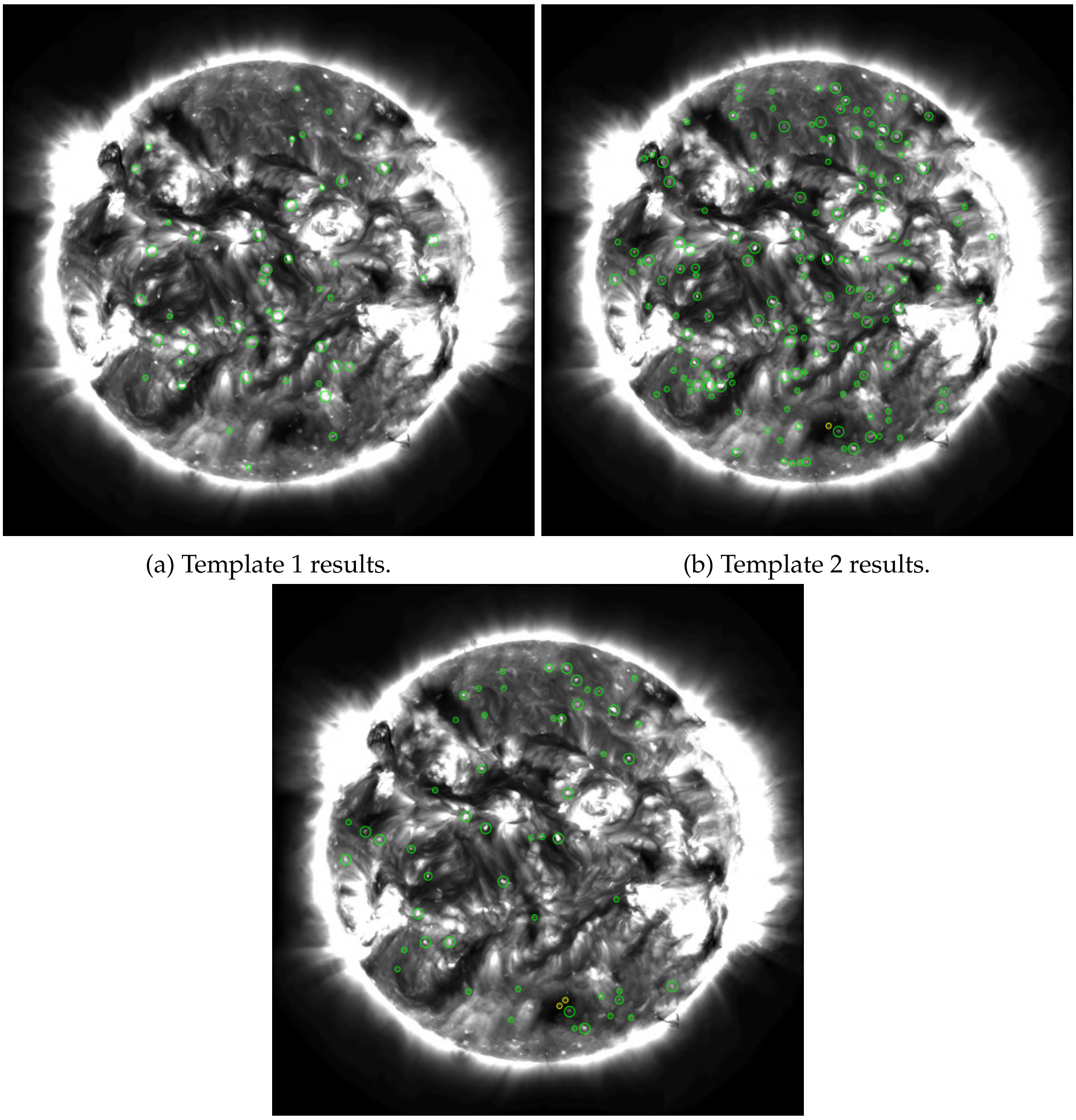

(a) Template 1 results.

(b) Template 2 results.

(c) Template 3 results.

Figure 4.2: Results of the different templates in a high solar activity image.

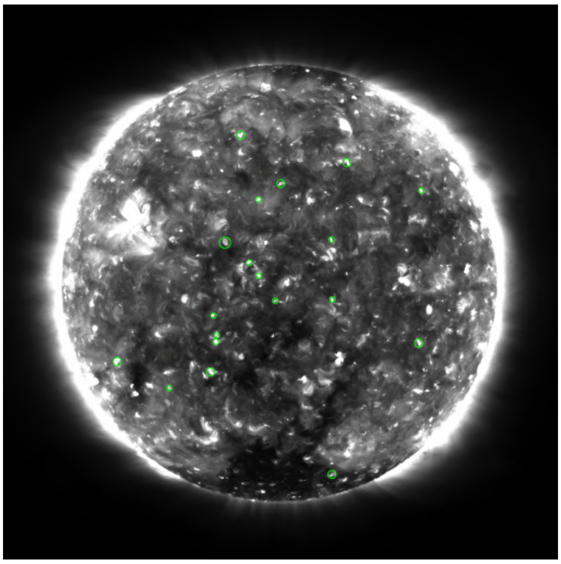

(a) Template 1 results.

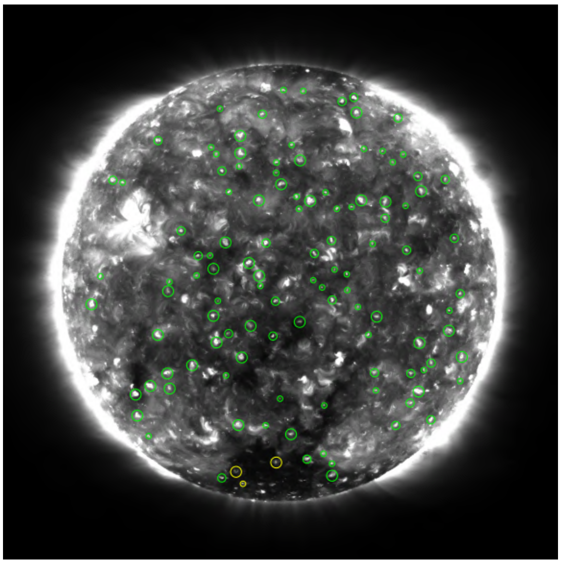

(b) Template 2 results.

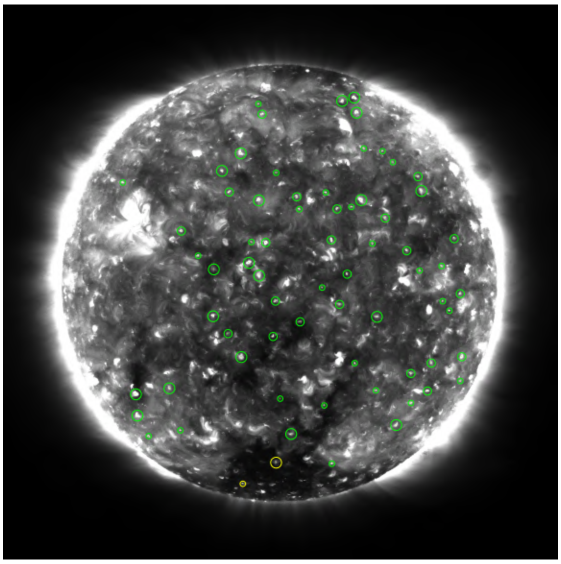

(c) Template 3 results.

Figure 4.3: Results of the different templates in a high low activity image.

4.1.2 Comparison between Match Template and GPL

To evaluate the performance of Match Template and GPL approaches, a total of 20 photos were selected, 10 from each of the two years: 2019 and 2023, when the Sun was observed to be in low and high activity, respectively.

The parameters used for this comparison were the processing time as well as the number of number of CBPs detected.

Table 4.1 suggests that the average processing time of the Match Template algorithm, about 10 seconds per image, is significantly lower than the one of GPL. It is possible to see that the average processing time does not change significantly in the Match Template even when the images are more complex and have more sun activity involved. This is due to the lower algorithm complexity in comparison to the higher complexity of GPL.

As it was explained in 2.4.2, GPL is an algorithm that is based on the labelling of gradient paths, which include various steps such as splitting the original image in different images to calculate the gradients and label all similar groups of pixels, repeating this for every sub image. Then, to compensate the over-segmentation, the merging of the labels costs a significant amount of processing time. On the other hand, the Match Template algorithm only uses a convolution method of sliding a template throughout the image giving a classification from 0 to 1 for every pixel.

	Average detection Time (seconds)		Individual Detections (10 image sequence)	
	Match Template	GPL	Match Template	GPL
High solar activity (2023)	9,517	186,961	1451	367
Low solar activity (2019)	9,758	116,349	1203	857

Table 4.1: Average detection time and individual detections: Match Template vs. GPL

When it comes to the total amount of CBP detections, the GPL was able to identify 367 points that resemble CBPs and the Match Template 1451, in a sequence of 10 images from 2023. In the sequence of 2019, the GPL detected 857 whereas the Match Template found 1203. Some of the points that were considered CBPs can be false positives, in either methods.

Figures 4.4 and 4.5, highlight the differences between both methods. It is clear that the Match Template validates more correct CBPs, as highlighted in orange boxes. However in figure 4.4 a pink box surrounds a place where the Match Template erroneously validates a group of solar flares, just as the GPL does in both figures(highlighted in blue). It is also noticeable that both algorithms perform better with low solar activity, nevertheless that issue is more evident with the GPL method.

Considering the lower processing time of the Match Template, its lower complexity and the amount of CBPs correctly validated, it is the most adequate CBP detection method when compared with GPL. Nevertheless, it is crucial to note that the step described in 4.1.1 plays an important role when it comes to the performance for identifying the CBPs, if the template is not adequate it will not perform as well as it should.

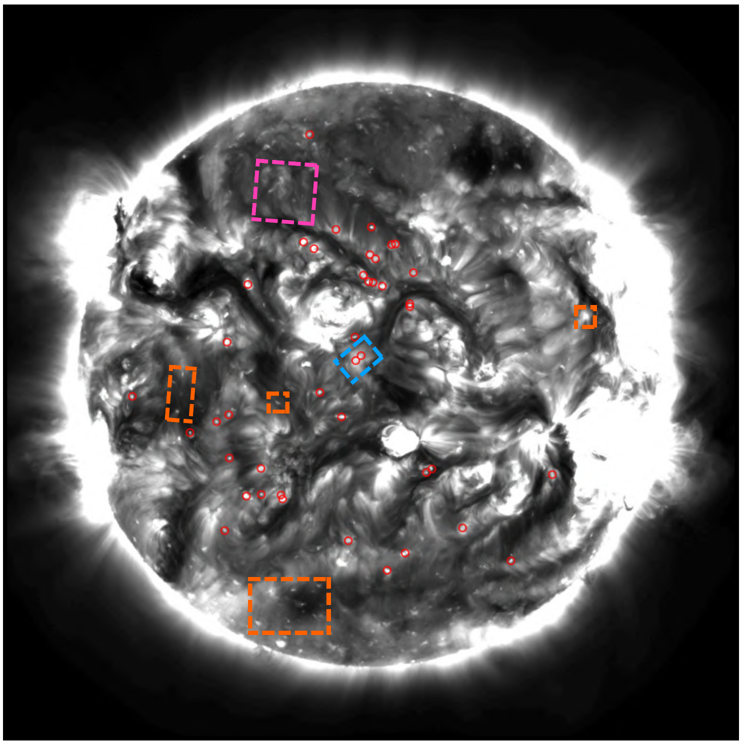

(a) GPL results.

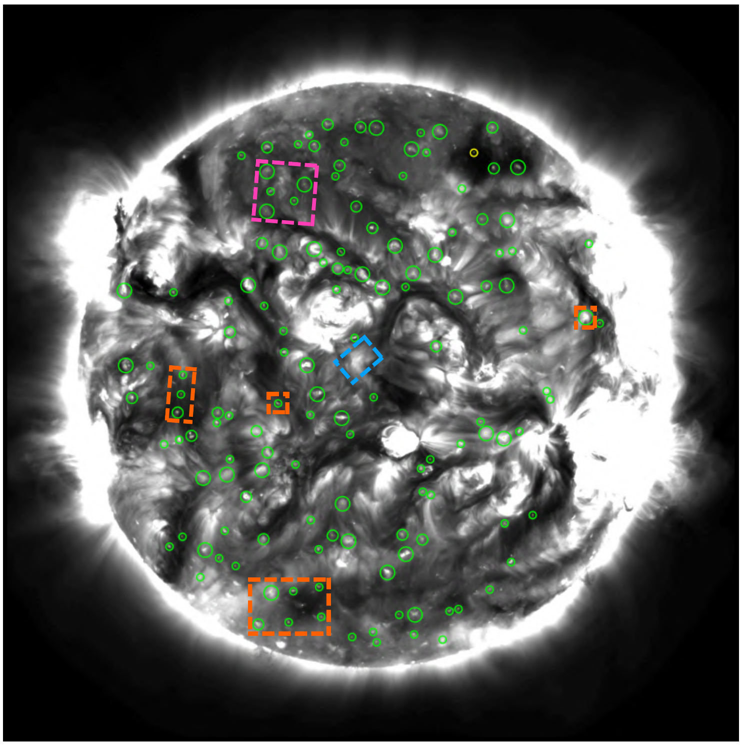

(b) Match template results.

Figure 4.4: Comparison between GPL and Match Template in a 2023 image.Boxes in orange represent CBPs not detected by GPL but detected by Match Template, boxes in pink represent solar flares detected as CBPs by Match Template and boxes in blue represent solar flare detected as CBPs by the GPL

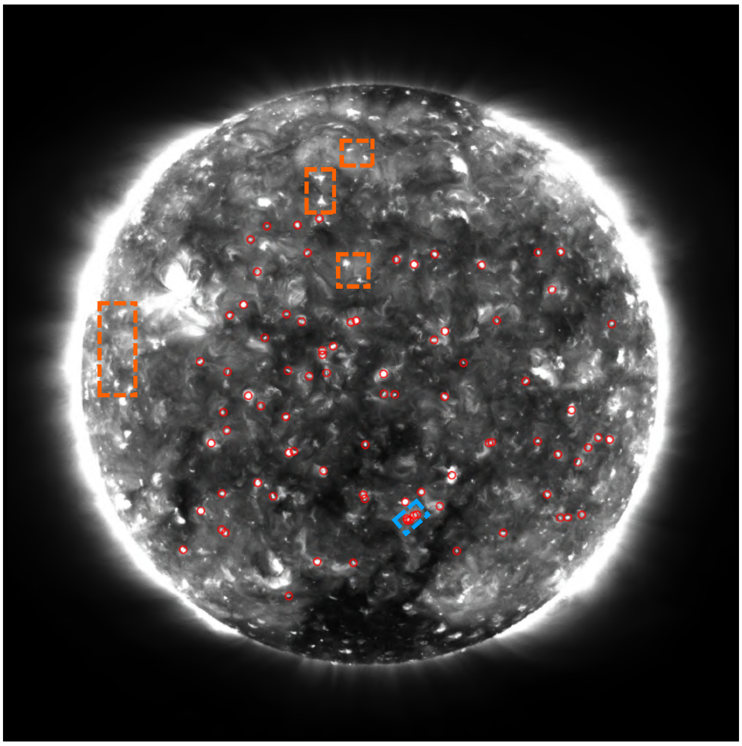

(a) GPL results.

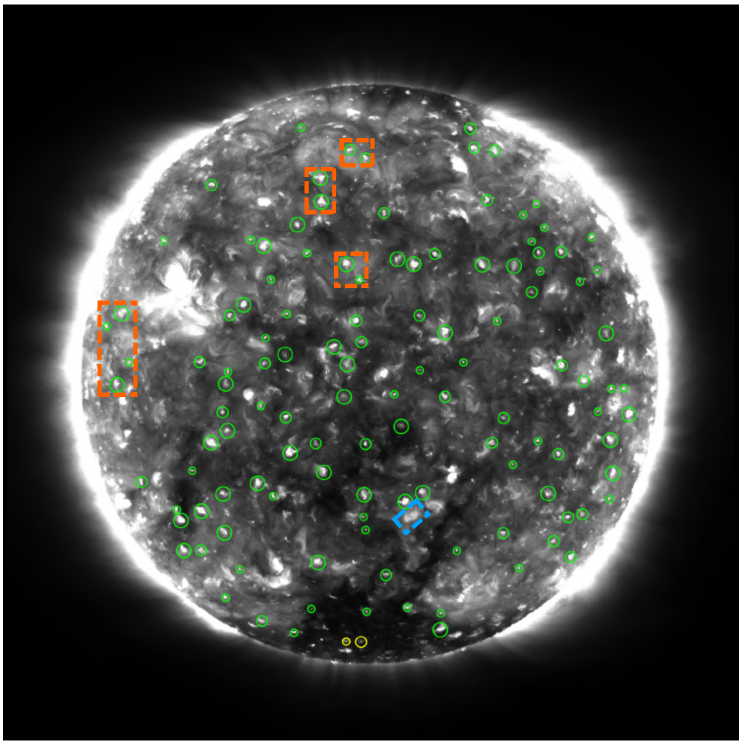

(b) Match template results.

Figure 4.5: Comparison between GPL and Match Template in a 2019 image.Boxes in orange represent CBPs not detected by GPL but detected by Match Template and boxes in blue represent solar flare detected as CBPs by the GPL

4.1.3 Results in a solar cycle

To evaluate the performance of this tool, it was tested along 8 days. The initial testing phase occurred from December 1, 2019, starting at 00:00:00, to December 5, 2019, at 00:00:00. Subsequently, additional testing took place from November 13, 2023, at 00:00:00, through November 17, 2023, at 00:00:00.

In the first phase, 2019, the tool was able to detect 63384 individual CBP identifications while, in 2023, the tool detected 69635 total individual identifications of CBPs. The locations of those measurements can be observed in figure 4.6.

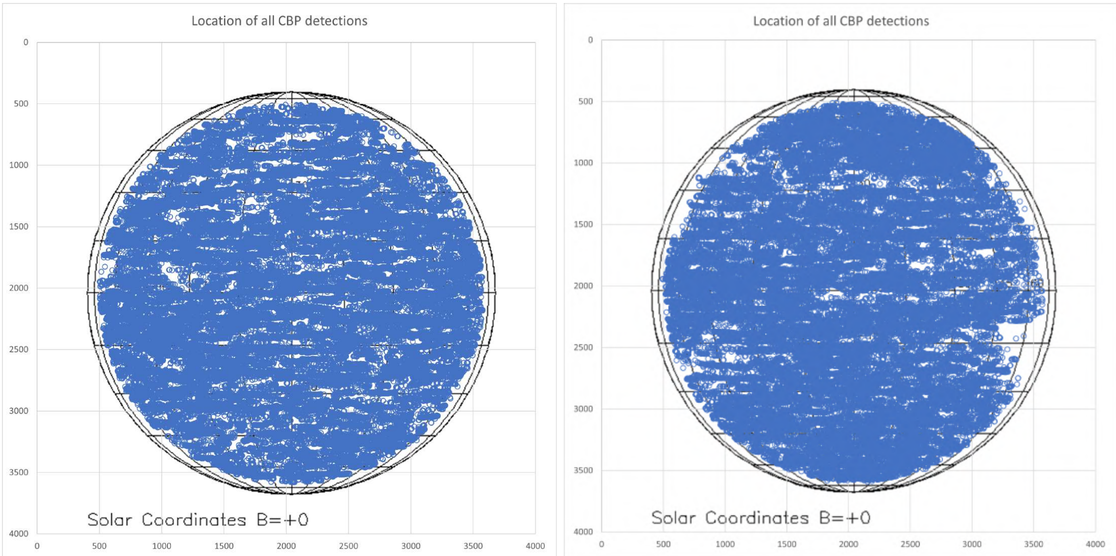

(a) 2019 detections

(b) 2023 detections

Figure 4.6: Total individual identifications location on the Suns corona.

It is possible to observe that it detected CBPs all over the solar corona only with the gap imposed of detecting only inside 85% of the Sun's radius.

4.2 Tracking and Solar Rotation Results

To obtain the tracking and solar rotation results, the same time interval for detection was applied. The testing periods were from December 1, 2019, at 00:00:00, to December 5, 2019, at 00:00:00, and from November 13, 2023, at 00:00:00, to November 17, 2023, at 00:00:00.

4.2.1 Tracking results in a solar cycle

For a comprehensive depiction of the tracking results, a graphical representation will be provided. This will include a plot illustrating the spatial location of the tracked CBPs, offering insights into their geographical distribution on the solar corona. Additionally, a histogram showcasing the lifetime distribution of the CBPs will be presented. This histogram serves as valuable information, shedding light on the behaviour patterns of CBPs over time. Together, these visualisations aim to provide a more nuanced understanding of the characteristics and dynamics of the tracked coronal bright points.

First Time Interval - 2019 Low Solar Activity

During this period, the developed tool successfully tracked 1992 CBPs. A CBP was considered trackable if it was detected at least 10 times, indicating a minimum lifetime of at least 2 hours.

The initial and final positions of the tracked CBPs can be seen in figure 4.7.

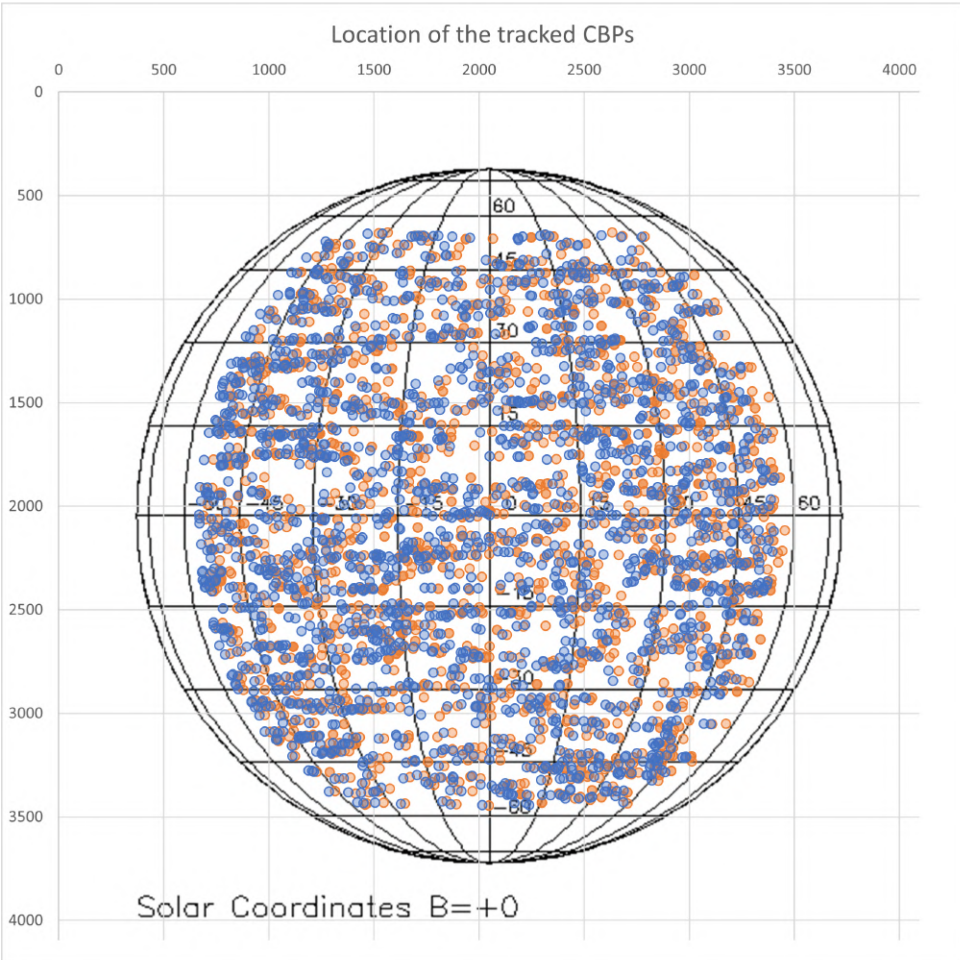

Figure 4.7: Initial (blue) and final (orange) location of tracked CBPs on the Suns corona, in 2019.

Figure 4.8 depicts the lifetime histogram of the CBPs tracked in this period of time. The average lifetime of a CBP is 5.5 hours, with only 17% of them above the expected 8 hour average value.

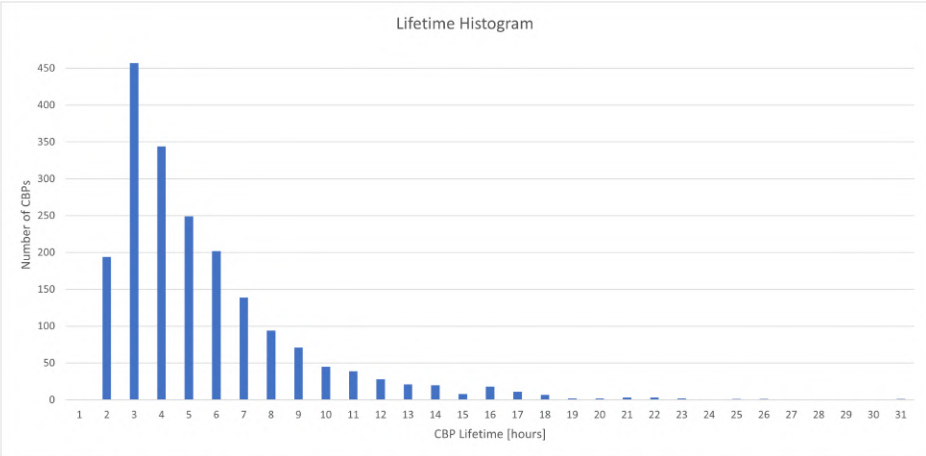

Figure 4.8: Lifetime histogram of the tracked CBPs, in 2019.

Second Time Interval - 2023 High Solar Activity

In this time frame, a total of 1959 CBPs were tracked. Figure 4.9 displays the initial positions of all tracked CBPs in blue and their final positions in orange.

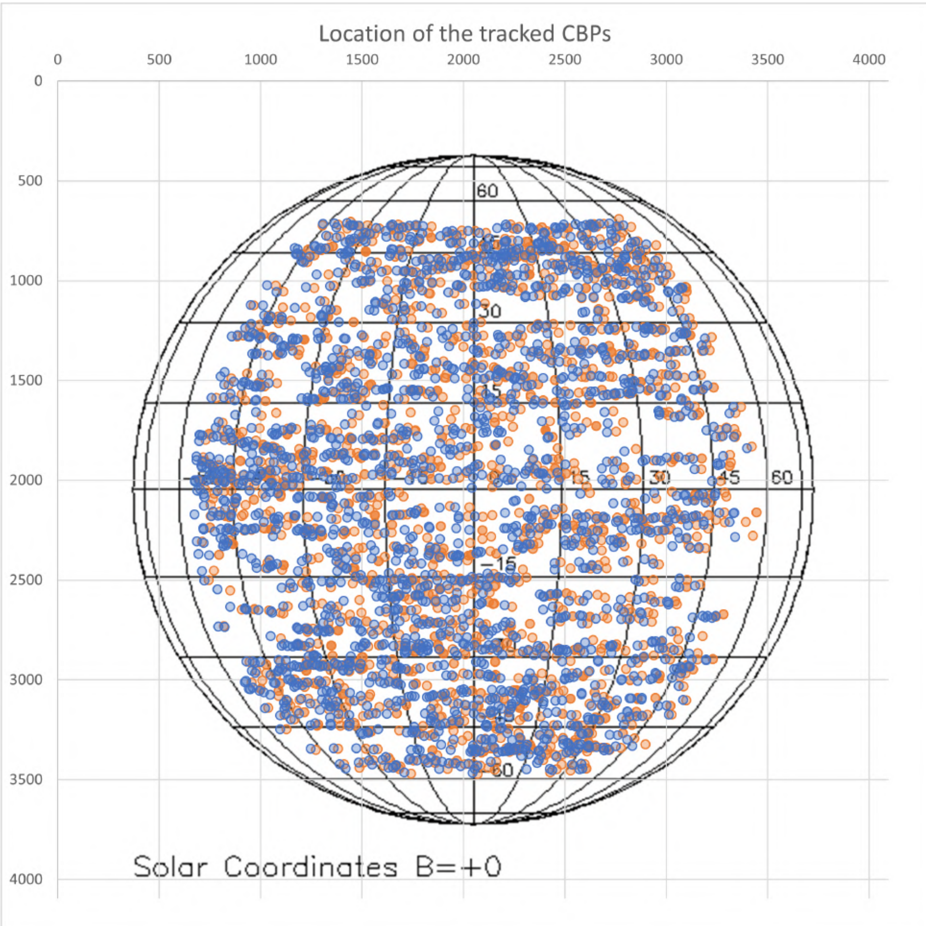

Figure 4.9: Initial (blue) and final (orange) location of tracked CBPs on the Suns corona, in 2023.

In figure 4.10, it can be seen an histogram of the lifetime of the CBPs, giving an average of 5,7 hours of lifetime. Only approximately 20% of the CBPs were tracked for more than 8 hours, that is commonly their average.

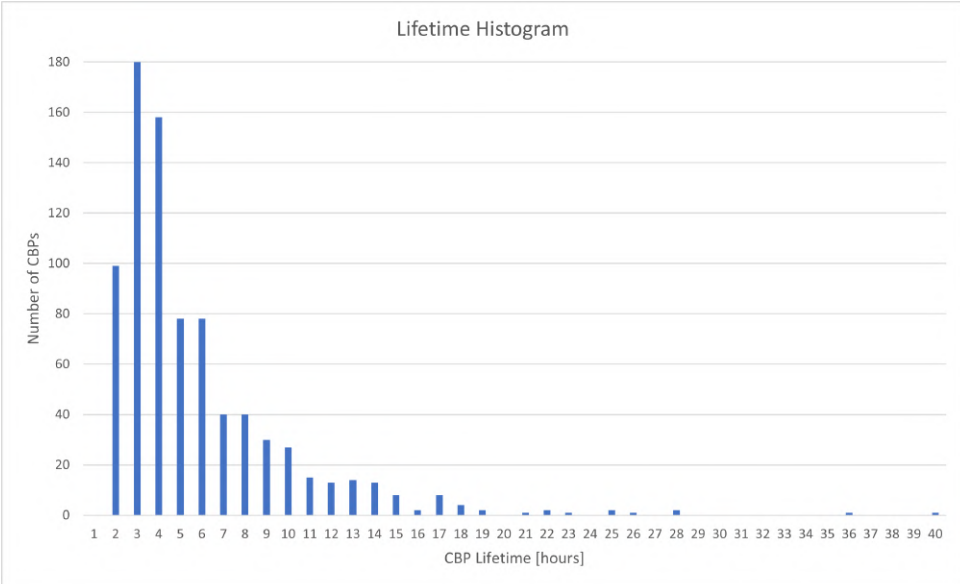

Figure 4.10: Lifetime histogram of the tracked CBPs, in 2023.

4.2.2 Solar Rotation profile in a solar cycle

For the solar rotation profile, it was used the most common fitting relation that is known for this matter, represented as (Howard & Harvey, 1970; Schroeter, 1985):

$$\omega(b) = A + B\sin^2(b) + C\sin^4(b), \tag{4.1}$$

where b is the latitude and A, B and C are constants determined by the observations and results obtained.

First Time Interval - 2019 Low Solar Activity

The coefficients A, B, and C were determined by analysing the trend line depicting the sidereal velocity against the sine of the latitude of the CBPs. Figure 4.11 visually represents this relationship.

In Figure 4.12, the scatter plot illustrates the relationship between sidereal rotation speed and latitude, featuring a predetermined best-fitting curve derived from Equation 4.1. The curve's coefficients, namely $A = 14.508$, $B = -0.2048$, and $C = -2.1828$, were established based on the trend line coefficients from Figure 4.11.

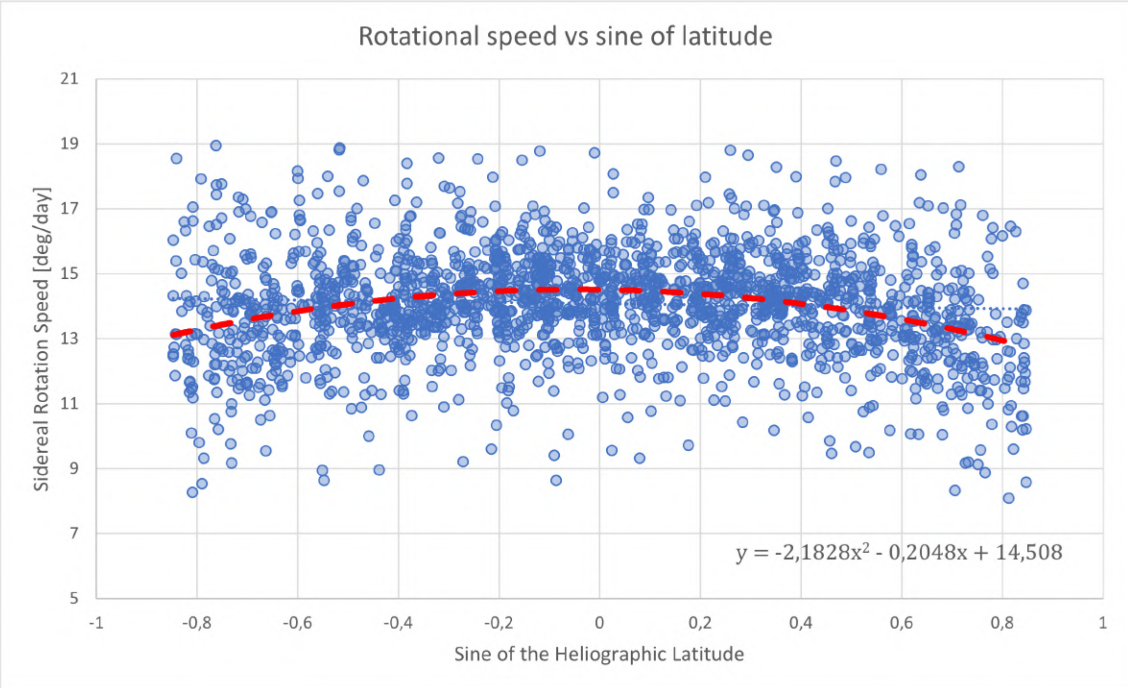

Figure 4.11: Scatter plot depicting the correlation between rotational speed and the sine of latitude for 2019 CBPs. The trend line of the data is presented in red.

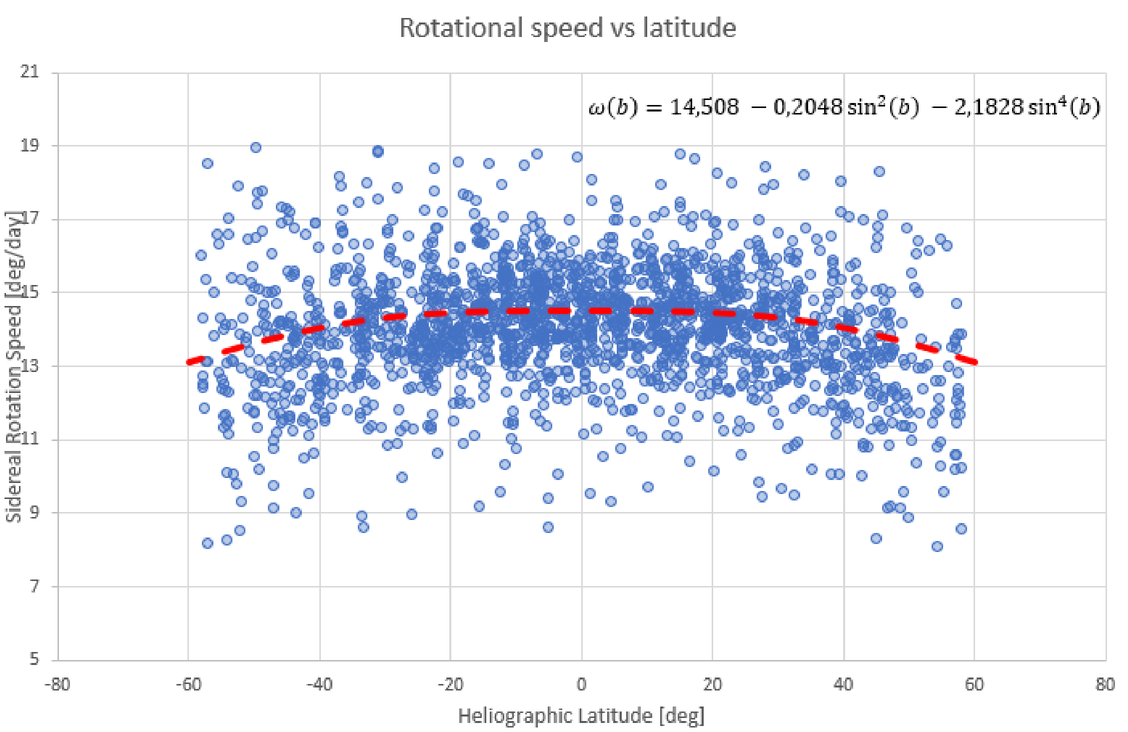

Figure 4.12: Scatter plot illustrating the association between rotational speed and latitude for 2019 CBPs, complemented by the best-fitting curve presented in red.

Second Time Interval - 2023 High Solar Activity

A parallel analysis with 2019 was conducted, resulting in the determination of coefficients A, B, and C from the trend line representing the sidereal velocity relative to the sine of the latitude of the CBPs. Figure 4.13 provides a visual representation of the acquisition of the coefficients.

Figure 4.14, shows the scatter plot of the sidereal rotation speed versus the latitude, along with the best-fitting curve already determined from equation 4.1, with the parameters $A = 14.649$, $B = -0.1327$ and $C = -2.9121$ established from the coefficients of figure's 4.13 trend line.

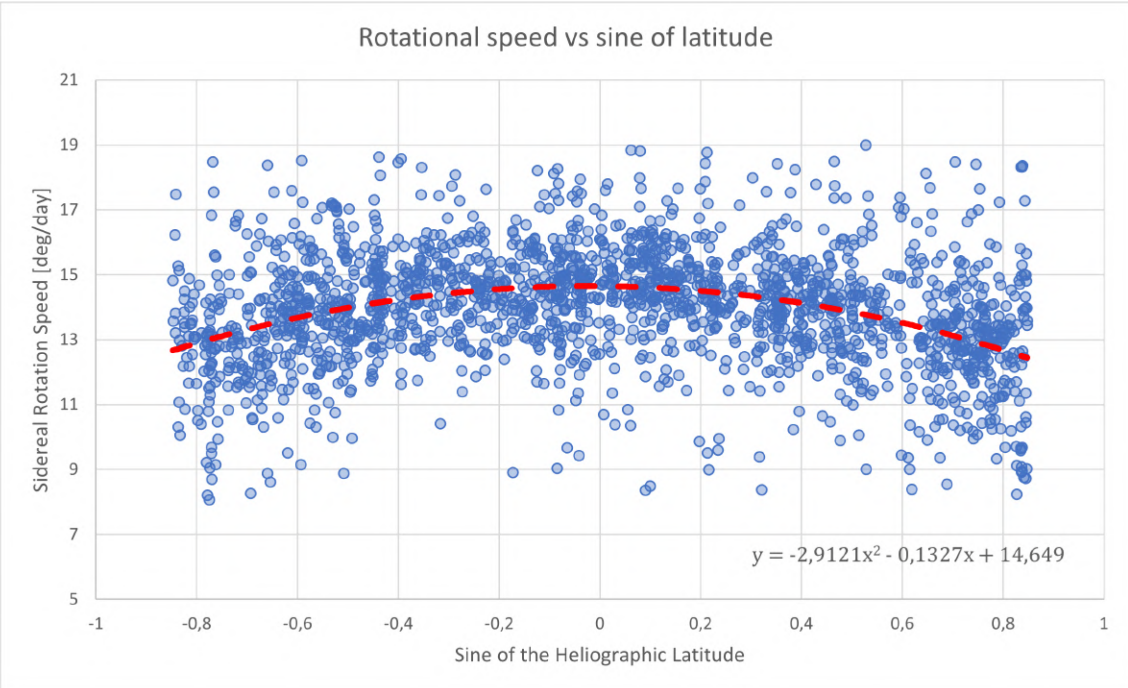

Figure 4.13: Scatter plot illustrating the relationship between rotation speed and the sine of latitude for 2023 CBPs. The trend line of the data is presented in red.

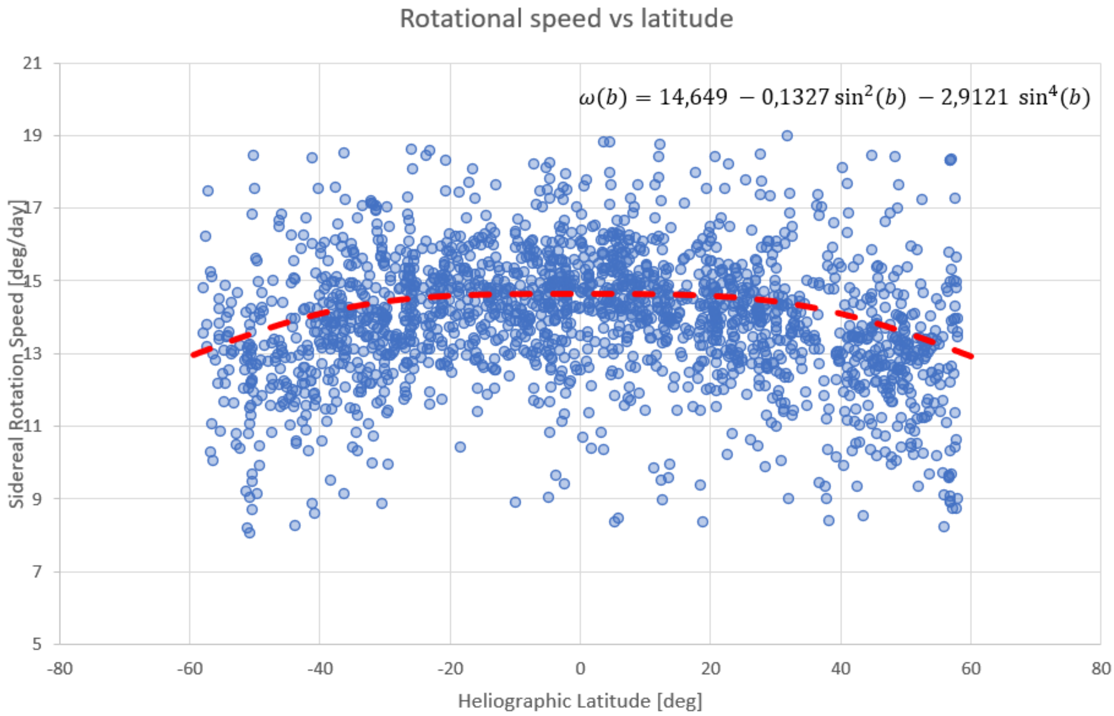

Figure 4.14: Scatter plot depicting the relationship between rotation speed and latitude for 2023 CBPs, accompanied by the best-fitting curve presented in red.

4.2.3 Impact of detection results on the tracking process

It is understood that detection results can significantly influence tracking. Therefore, it is crucial to clarify the manner in which they impact it.

For this matter, it was questioned the consequences of the number of individual detections for each CBP in the rotational speed values. Looking at figure 4.15a, it is possible to understand that when the number of detections is less than 20 times (4 hours of lifetime) the speed values are dispersed, not showing a clear consistency. However, figure 4.15b demonstrates that, when the number of detections is higher than 20, the speed values tend to be closer to the best-fitting curve.

Another analysis regarding the speed of each CBP given their position was performed. It was possible to notice that some CBPs presented speed either to fast or too slow for their latitude. Figure 4.16 present the scatter plot of the location of the CBPs defined by a colour coded circle based on their speed value.

So to understand this event better, a few CBPs were chosen to examine if the number of detections affected the speed value. One example CBP is the one in figure 4.16, situated between the Y value of 3000 and 3500 and within the X values of 2500 to 3000, highlighted in blue. This CBP should exhibit a speed of less than 13 deg/day, in line with expectations. However, upon analysis, it was found that this CBP did not meet this criterion. It was observed that it only had 13 individual detections. In contrast, neighboring CBP at a similar latitude near a X value of 2500, such as the one highlighted in yellow, had more

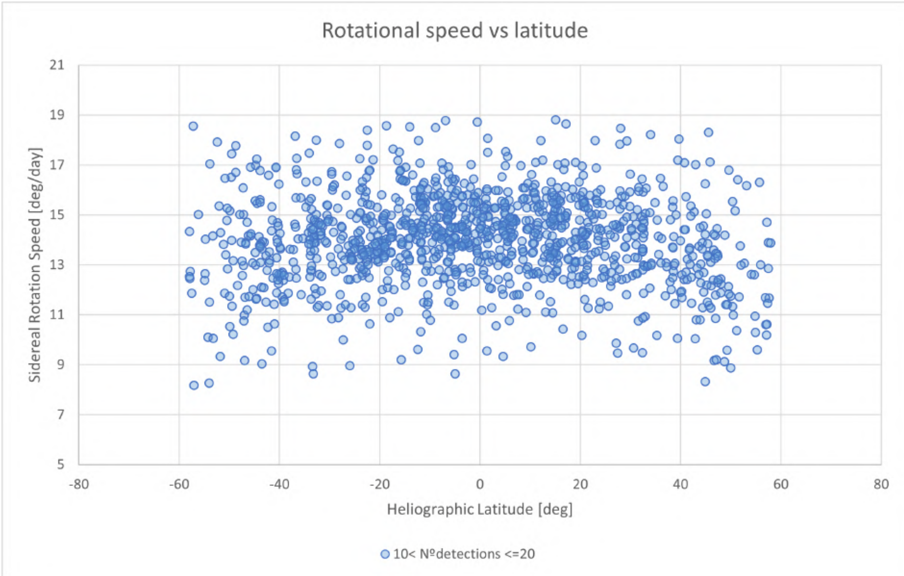

(a)

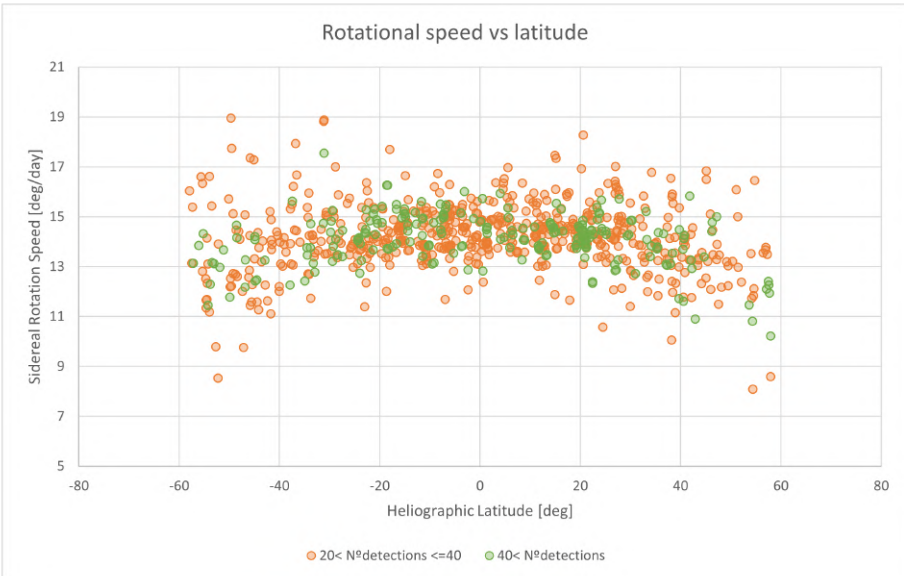

(b)

Figure 4.15: Colour-coded plot illustrating the correlation between individual detection count and the relationship between rotation speed and latitude. Data from the 2019 time interval.

than 40 individual detections and exhibited the expected rotation speed.

Figure 4.17 depicts the same scatter plot as 4.16, with the particularity that it is also color coded for the number of individual detections. This way it is possible to better understand how the number of detections influence the values of speed, such as the example mentioned in the last paragraph.

These type of occurrences, regarding the number of individual detections, happened in both years of 2019 and 2023. This reinforces the assertion that a higher number of individual detections for a CBP leads to better results in terms of rotational speed.

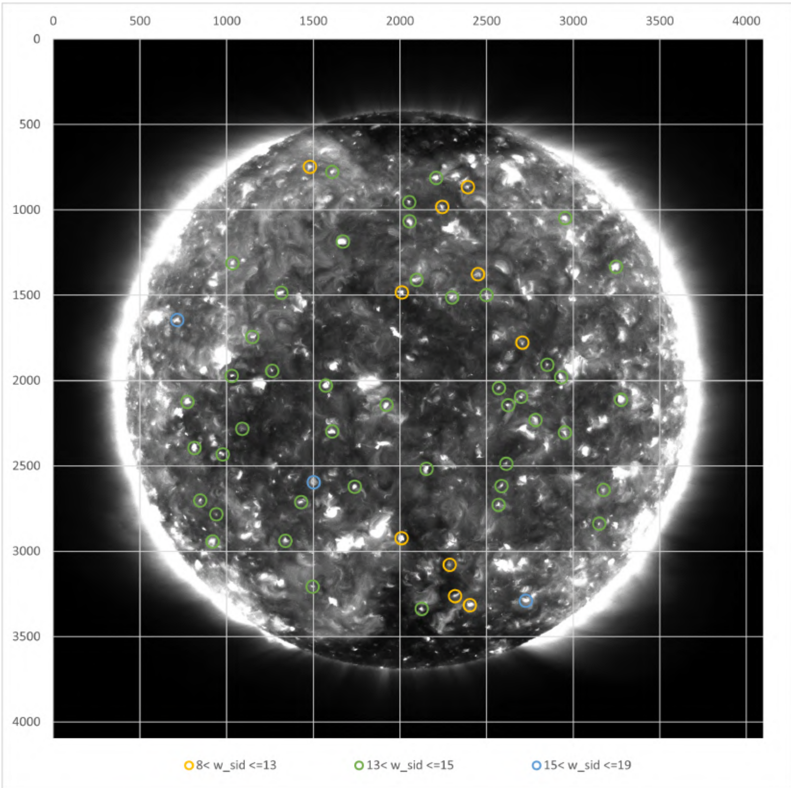

Figure 4.16: Colour coded scatter plot illustrating the position of the tracked CBPs in one image, based on their speed.

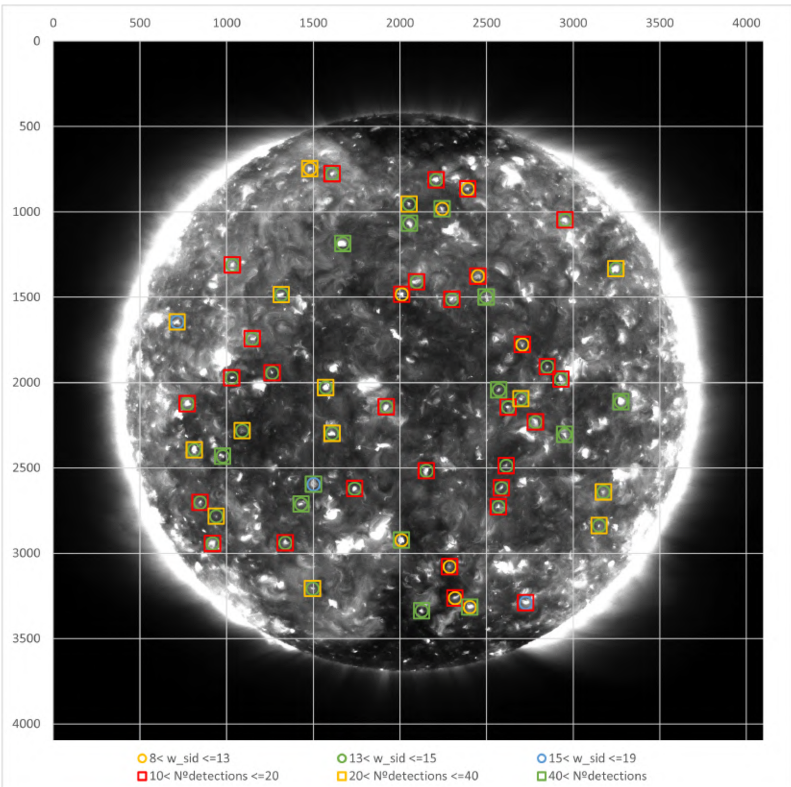

Figure 4.17: Colour coded scatter plot illustrating the position of the tracked CBPs in one image, based on their speed and number of detections.

4.2.4 Analysis of the results in a solar cycle

The investigation into the solar rotation profile across two distinct time intervals, characterized by low and high solar activity in 2019 and 2023, respectively, yields valuable insights into the dynamic Coronal Bright Points (CBPs).

A noteworthy observation is the distribution of the monitored CBPs in both time intervals. In the 2019 representation, CBPs are evenly spread across the entire spatial range, constrained within ±60° in latitude and longitude. However, in the 2023 depiction, visible gaps emerge. These voids are attributed to ongoing solar activities, including flares and possibly coronal holes, influencing the distribution pattern.

The derived coefficients A, B, and C from the fitting relation in Equation 4.1 offer a quantitative representation of the solar rotation characteristics.

Comparing the results from the first time interval (2019 Low Solar Activity) to the second time interval (2023 High Solar Activity), noticeable variations in the coefficients indicate a temporal evolution in the solar rotation profile. The change in A, B, and C suggests alterations in the overall rotational dynamics of CBPs over the solar cycle.

Figure 4.18 provides a side-by-side comparison of the best-fitting curves for the two time intervals, elucidating the nuanced changes in the solar rotation profile.

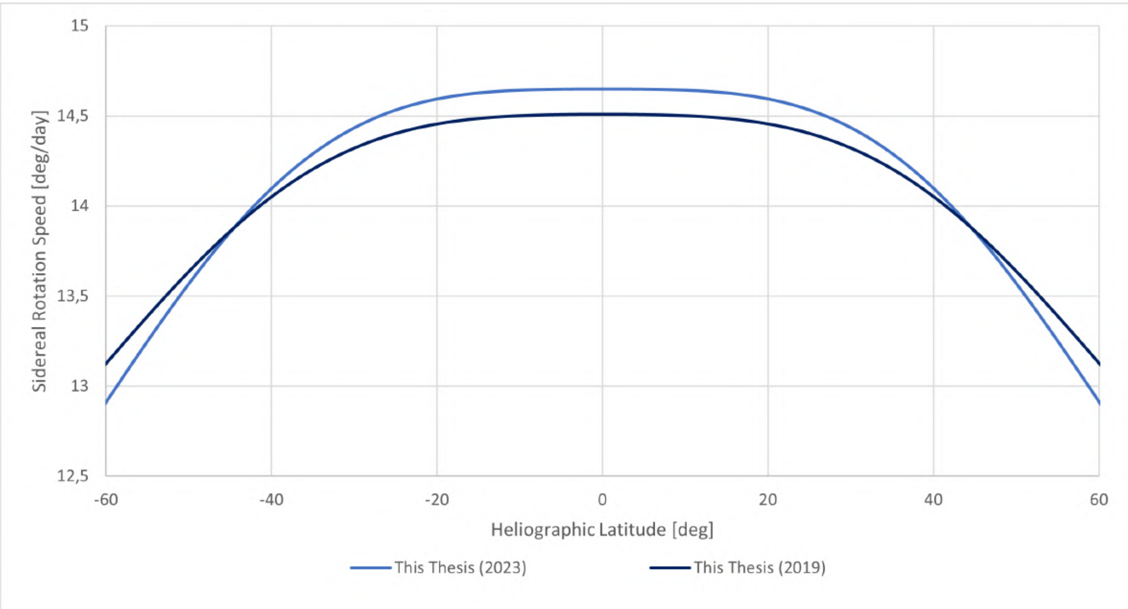

Figure 4.18: Comparison of solar rotation profiles between 2019 and 2023 by the representation of the best-fitting curves.

Notably, the analysis reveals a tendency for CBPs located closer to the poles to exhibit lower rotational speeds compared to those near the equator. This event is consistent with previous solar cycle observations as it was noted in the State of the Art in section 2.1.

4.2.5 Comparison with other works

While direct comparisons of measurements may be challenging due to variations in time and imaging conditions, key fitting parameters are presented in Table 4.2 and the corresponding fitting curves are illustrated in Figure 4.19.

The notable disparities observed among the curves in different studies can be attributed to three significant factors: the time frame of the utilised images and the employed CBP detection algorithm. As previously demonstrated in Section 4.2.4, the year of origin for the images plays a pivotal role in shaping the best-fitting curve, influenced by the prevailing solar activity at that specific time. Additionally, the efficacy and precision of the detection algorithm can significantly impact the tracking algorithm's behaviour, consequently influencing the curve's derivation. Finally, the number of days of testing can also influence the obtained results in the curve derivation process.

Despite the known disparities, it is still evident that the curves exhibit a consistent structure, reinforcing the observed pattern of reduced speed near the poles.

A noteworthy observation is the difference in the offset. For instance, consider the curve from the work of Dorotovič et al. (2018), depicted in red. Given the images are from 2010, a year with similar solar activity as 2023, and despite presenting a similar concavity, there exists an offset difference of nearly 0.5 deg/day when comparing with this work's test during 2023. This variation could be attributed to a previously mentioned factor, the detection algorithm employed, as it is known that the GPL, the method explained in 2.4.2, was the method chosen by Dorotovič et al. (2018). Another factor that could influence the results is the method that Dorotovič et al. (2018) used to obtain the synodical velocity, which was different than the one utilised in this work.

Article/work	Year	Number of days	Total Measurements	A [°/day]	B [°/day]	C [°/day]
This Thesis	2023	4	69635	14,649	-0,1327	-2,9121
This Thesis	2019	4	63384	14,508	-0,2048	-2,1828
Pires (2018)	2018	4	173666	13,836	-0,2487	-2,4142
Dorotovič et al.(2018)	2010	3	31183	14,187	-0,43	-5,09
Sudar et al. (2016)	2011	138	80966	14,406	-1,662	-2,742
Sudar et al. (2015)	2011	2	13646	14,47	0,6	−4,7

Table 4.2: Results of this work's fitting parameters in comparison to other authors' works.

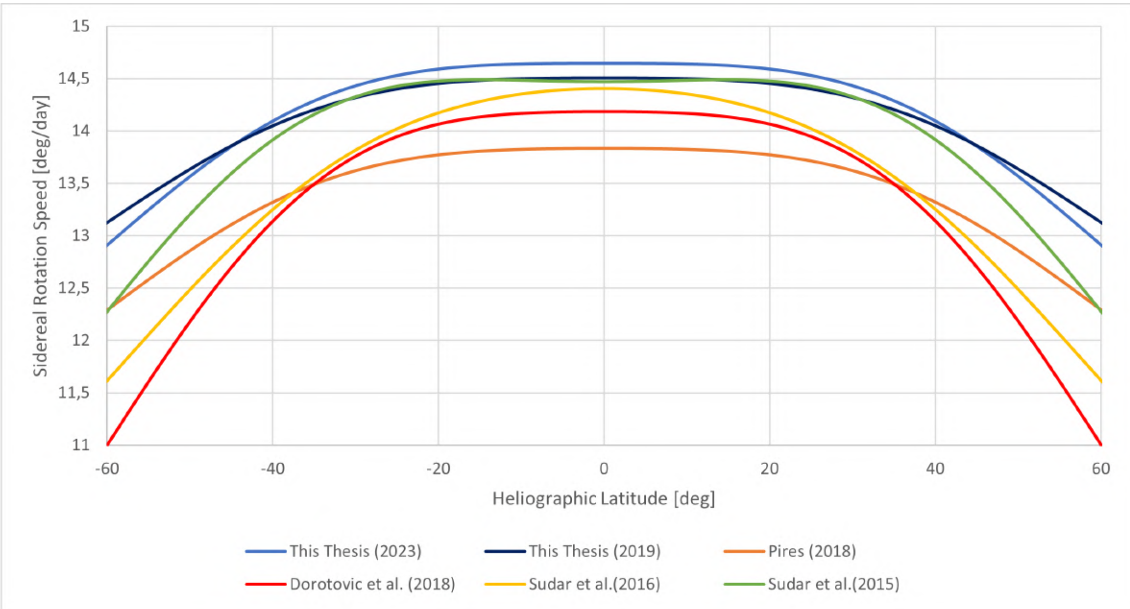

Figure 4.19: Comparison of the best-fitting curves of this and previous works.

5 Conclusions and Future Work

5.1 Conclusions

The main objective of this dissertation was to develop a tool that could offer more precise results about the solar rotation speeds and a website that could provide a user-friendly interface for anyone curious about this topic.

The image dataset used was from the SDO/AIA instrument since it provides a good cadence between images as well as high resolution. The selected EUV channel was the 193 Å where it can be seen the Sun's corona and hot flare plasma.

The proposed CBPs detection method was able to detect the majority of the CBPs in the most important time frames of a solar cycle, during the solar minimum and during the solar maximum, obtaining good results that were able to lay solid grounds for the tracking method. Throughout the 8 days of testing, it was possible to obtain 63384 individual detections in the 2019 interval and 69635 in the 2023 interval. This traduced in a total of 3951 tracked CBPs. These results were considered valuable because they did not deviate significantly in comparison to the results form other authors and, despite some false positive detections, the tool was able to identify numerous CBPs, even some of the most difficult. This tool has also a big advantage, when comparing with other similar ones that had the same objective, that is its low algorithmic complexity meaning a lower execution time.

The method employed for the tracking task played a crucial role in eliminating false positives and calculating the differential rotation speed of the solar corona. When it comes to the differential solar rotation profile, the CBPs tracking and the inherent speed calculations yielded the expected results, revealing a slower rotation speed at the poles contrasting with the higher speed near the equator. The expected speed values of close to 14 deg/day were achieved at 0 degrees latitude position and 13 deg/day at 60 degrees, indicating a solar period of approximately 25 days and 28 days, respectively. When comparing time frames of high solar activity to those of low activity, the best-fitting curves exhibited a similar shape. However, a noticeable offset was observed, indicating a higher overall rotation speed during periods of solar activity.

Finally, a website has been successfully developed to present the results of solar rotation. The website offers information about the latest detected CBPs and the differential rotation over time, all accessible from the front page. Users can select a specific time interval to observe data from that period on a page named *Archive*. Additionally, there is a dedicated page that displays information about the Coronal Holes detected in the processed images.

5.2 Future Work

In studies like this, there is always room for improvement. This includes improving both the methods used for detection and tracking, as well as refining the content and interface of the website to enhance user experience and research outcomes.

Despite the positive results achieved by the suggested approach, there are other paths for detecting and tracking CBPs. One such path involves incorporating Artificial Intelligence, which, given its recent advancements, shows promise as a valuable tool in this field.

Considering the latter suggestion, there is an opportunity to improve the detection and tracking process throughout the entire solar corona, going beyond current spatial constraints. This expansion could provide new insights into the differential rotation in regions such as the poles and limbs.

Additionally, there is room for improvement in identifying additional solar activities detectable through the image modalities used, thereby enhancing the content on the website. This goal could be achieved by utilising the various image wavelengths accessible via the NASA/SDO website.

Bibliography

Abdulateef, S. K., & Salman, M. D. (2021). A Comprehensive Review of Image Segmentation Techniques. *Al-mağalla al-irāqiyya al-handasa al-kahrabāiyya wa-al-iliktrūniyya*, *17*(2), 166–175. https://doi.org/10.37917/ijeee.17.2.18 (cit. on p. 13).

Addison, K. M. (2023). SDO | Solar Dynamics Observatory [Accessed: 29-05-2023]. https://sdo.gsfc.nasa.gov/gallery/main/item/420 (cit. on p. 10).

Balthasar, H., Vazquez, M., & Woehl, H. (1986). Differential rotation of sunspot groups in the period from 1874 through 1976 and changes of the rotation velocity within the solar cycle., *155*(1), 87–98 (cit. on p. 11).

Bo, J., Lei, L., Sheng, Z., Shan-Shan, Y., Shu-Guang, Z., Yao, H., & Xiao-Yu, L. (2022). An Automatic Detection for Solar Active Regions Based on Scale-Invariant Feature Transform and Clustering by Fast Search and Find of Density Peaks. *Chinese Astronomy and Astrophysics*, *46*(3), 264–276. https://doi.org/10.1016/j.chinastron.2022.09.007 (cit. on p. 21).

Bose, S., Nóbrega-Siverio, D., De Pontieu, B., & Van Der Voort, L. R. (2023). The Chromosphere Underneath a Coronal Bright Point. *The Astrophysical Journal*, *944*(2), 171. https://doi.org/10.3847/1538-4357/acb544 (cit. on p. 11).

Brajša, R., Wöhl, H., Vršnak, B., Ruždjak, V., Clette, F., & Hochedez, J.-F. (2001). Solar differential rotation determined by tracing coronal bright points in SOHO-EIT images. *Astronomy and Astrophysics*, *374*(1), 309–315. https://doi.org/10.1051/0004-6361:20010694 (cit. on p. 2).

Carreira, A. (2020, October). *Detection and tracking of coronal holes in solar images* [Master's thesis]. FCT-UNL. http://hdl.handle.net/10362/106550 (cit. on pp. 3, 29, 30, 38).

Coelho, A. (2017, July). *Solar rotation speed by detecting and tracking of Coronal Bright Points* [Master's thesis]. FCT-UNL. http://hdl.handle.net/10362/34371 (cit. on p. 29).

Curiale, A. H., Vegas-Sánchez-Ferrero, G., & Aja-Fernández, S. (2018, January). Techniques for tracking: image registration. In *Institution of engineering and technology ebooks* (pp. 321–351). https://doi.org/10.1049/pbhe013e_ch15 (cit. on p. 19).

DeRosa, M., & Slater, G. (2010, December). Guide to SDO Data Analysis [Accessed: 28-09-2023]. https://helio.cfa.harvard.edu/trace/SSXG/ynsu/Ji/SDO_Data_Analysis_guide.pdf (cit. on p. 27).

Dobrijevic, D. (2022, May). Sunspots: What are they, and why do they occur? https://www.space.com/sunspots-formation-discovery-observations#section-sunspots-and-the-solar-cycle (cit. on p. 11).

Dorotovič, I., Coelho, A., Rybák, J., Mora, A., & Ribeiro, R. (2018). Gradient path labelling method and tracking method for calculation of solar differential rotation using coronal bright points. *Astronomy and Computing*, *25*, 168–175. https://doi.org/https://doi.org/10.1016/j.ascom.2018.09.008 (cit. on pp. 2, 15, 19, 29, 62).

Dorotovič, I., Fernandes, J., Fonseca, J. M., Mora, A., Moreira, C., & Ribiero, R. A. (2007, May). COSIS: Coimbra Observatory Solar Information System. In P. Heinzel, I. Dorotovič, & R. J. Rutten (Eds.), *The physics of chromospheric plasmas* (p. 523, Vol. 368). (Cit. on p. 13).

BBSO. (2023a). BBSO Full Disk Halpha Telescope [Accessed: 09-05-2023]. http://www.bbso.njit.edu/Research/FDHA/ (cit. on p. 7).

BBSO. (2023b). Big Bear Solar Observatory [Accessed: 09-05-2023]. http://www.bbso.njit.edu/ (cit. on p. 7).

ESA. (2023). The Sun in high resolution [Accessed: 13-05-2023]. https://www.esa.int/ESA_Multimedia/Images/2022/03/The_Sun_in_high_resolution (cit. on p. 9).

NSO. (2020, April). Virtual Solar Observatory [Accessed: 27-09-2023]. https://nso.edu/data/vso (cit. on p. 25).

NSO. (2022, May). Daniel K. Inouye Solar Telescope - NSO - National Solar Observatory [Accessed: 09-05-2023]. https://nso.edu/telescopes/dki-solar-telescope/ (cit. on p. 7).

NSO. (2023, February). Gallery Images from the Inouye - NSO - National Solar Observatory [Accessed: 09-05-2023]. https://nso.edu/gallery/gallery-images-from-the-inouye (cit. on p. 7).

SDO. (2023a). SDO | Solar Dynamics Observatory [Accessed: 11-05-2023]. https://sdo.gsfc.nasa.gov/mission/ (cit. on p. 8).

SDO. (2023b). SDO | Solar Dynamics Observatory [Accessed: 13-05-2023]. https://sdo.gsfc.nasa.gov/data/ (cit. on p. 9).

SDO. (2023c). SDO | Solar Dynamics Observatory [Accessed: 04-01-2024]. https://sdo.gsfc.nasa.gov/assets/img/browse/2023/11/16/20231116_000717_1024_0193.jpg (cit. on p. 43).

SOHO. (2023). The Very Latest SOHO Images [Accessed: 13-05-2023]. https://soho.nascom.nasa.gov/data/realtime-images.html (cit. on p. 9).

Gopalswamy, N. (2016). History and development of coronal mass ejections as a key player in solar terrestrial relationship. *Geoscience Letters*, *3*(1). https://doi.org/10.1186/s40562-016-0039-2 (cit. on p. 9).

GREGOR Solar Telescope [Accessed: 09-05-2023]. (2023). https://www.iac.es/en/observatorios-de-canarias/telescopes-and-experiments/gregor-solar-telescope (cit. on p. 7).

Hill, F., Martens, P., Yoshimura, K., Gurman, J., Hourclé, J., Dimitoglou, G., Suárez-Solá, I., Wampler, S., Reardon, K., Davey, A., Richard, B., & Tian, K. (2009). The virtual solar observatory—a resource for international heliophysics research. *Earth, Moon, and Planets*, *104*, 315–330. https://doi.org/10.1007/s11038-008-9274-7 (cit. on p. 26).

Howard, R., & Harvey, J. (1970). Spectroscopic Determinations of Solar Rotation. *Solar Physics*, *12*(1), 23–51. https://doi.org/10.1007/BF02276562 (cit. on p. 55).

Imada, S., & Fujiyama, M. (2018). Effect of Magnetic Field Strength on Solar Differential Rotation and Meridional Circulation. *The astrophysical journal*, *864*(1), L5. https://doi.org/10.3847/2041-8213/aad904 (cit. on p. 6).

Jones, C., Thompson, M., & Tobias, S. M. (2009). The Solar Dynamo. *Space Science Reviews*, *152*(1-4), 591–616. https://doi.org/10.1007/s11214-009-9579-5 (cit. on p. 11).

Kambry, M. A., & Nishikawa, J. (1990). Solar differential rotation derived from sunspot observations., *126*, 89–100. https://doi.org/10.1007/BF00158300 (cit. on p. 11).

Lorenc, M., Rybanský, M., & Dorotovič, I. (2012). On Rotation of the Solar Corona. *Solar Physics*. https://doi.org/10.1007/s11207-012-0105-7 (cit. on p. 13).

Lourenço, J. M. (2021). *The NOVAthesis LaTeX Template User's Manual*. NOVA University Lisbon. https://github.com/joaomlourenco/novathesis/raw/main/template.pdf (cit. on p. ii).

Mackay, D. S., Karpen, J. T., Ballester, J. L., Schmieder, B., & Aulanier, G. (2010). Physics of Solar Prominences: II—Magnetic Structure and Dynamics. *Space Science Reviews*, *151*(4), 333–399. https://doi.org/10.1007/s11214-010-9628-0 (cit. on p. 10).

Mackay, D. H. (2021). Solar Prominences. *Oxford Research Encyclopedia of Physics*. https://doi.org/10.1093/acrefore/9780190871994.013.17 (cit. on pp. 10, 11).

Madjarska, M. S. (2019). Coronal bright points. *Living Reviews in Solar Physics*, *16*(1). https://doi.org/10.1007/s41116-019-0018-8 (cit. on p. 12).

Martens, P. C., Attrill, G. D. R., Davey, A. R., Engell, A., Farid, S., Grigis, P. C., Kasper, J. C., Korreck, K. E., Saar, S. H., Savcheva, A., Su, Y.-K., Testa, P., Wills-Davey, M. J., Bernasconi, P., Raouafi, N.-e., Delouille, V., Hochedez, J.-F., Cirtain, J., DeForest, C., . . . Timmons, R. (2012). Computer Vision for the Solar Dynamics Observatory (SDO). *Solar Physics*, *275*(1-2), 79–113. https://doi.org/10.1007/s11207-010-9697-y (cit. on pp. 14, 15).

McIntosh, P. S. (1990). The classification of sunspot groups. *Solar Physics*, *125*, 251–267 (cit. on p. 11).

Mcintosh, S., & Gurman, J. (2004). Eit euv brightpoints over the soho mission so far. *European Space Agency, (Special Publication) ESA SP*, *575*, 235 (cit. on p. 14).

McIntosh, S. W., & Gurman, J. B. (2005). Nine Years Of Euv Bright Points. *Solar Physics*, *228*(1-2), 285–299. https://doi.org/10.1007/s11207-005-4725-z (cit. on pp. 14, 15).

McIntosh, S. W., Wang, X., Leamon, R. J., & Scherrer, P. H. (2014). IDENTIFYING POTENTIAL MARKERS OF THE SUN'S GIANT CONVECTIVE SCALE. *The* *astrophysical journal*, *784*(2), L32. https://doi.org/10.1088/2041-8205/784/2/l32 (cit. on p. 15).

Mora, A. (2010, December). *Advanced image processing techniques for detection and quantification of drusen* [Doctoral dissertation]. https://www.researchgate.net/publication/239526727_Advanced_image_processing_techniques_for_detection_and_quantification_of_drusen (cit. on pp. 15–17).

NASA. (2006). NASA - Sun-Earth Day - Technology Through Time. https://sunearthday.nasa.gov/2006/locations/firstphoto.php (cit. on p. 6).

NASA. (2014, October). FITS primer. https://fits.gsfc.nasa.gov/fits_primer.html (cit. on p. 26).

NASA. (2017). Solar Rotation Varies by Latitude [Accessed: 29-05-2023]. https://www.nasa.gov/mission_pages/sunearth/science/solar-rotation.html (cit. on p. 6).

NASA. (2019). In Depth | SOHO – NASA Solar System Exploration [Accessed: 12-05-2023]. https://solarsystem.nasa.gov/missions/soho/in-depth/ (cit. on p. 8).

NASA. (2021). In depth | sun [Accessed: 05-05-2023]. *NASA Solar System Exploration*. https://solarsystem.nasa.gov/solar-system/sun/in-depth (cit. on p. 2).

NASA. (2023). Solar Orbiter Science [Accessed: 12-05-2023]. https://www.nasa.gov/content/solar-orbiter-science (cit. on p. 9).

Pires, R. (2018, November). *A web tool to detect and track solar features from sdo images* [Master's thesis]. FCT-UNL. http://hdl.handle.net/10362/82461 (cit. on pp. 3, 22, 24, 28, 35, 37, 38).

Pires, R., Dorotovic, I., Ribeiro, R., Fonseca, J. M., Rybák, J., & Mora, A. (2019). Cbptracker - a web tool to detect and track solar features from sdo/ aia images. *2019 International Young Engineers Forum (YEF-ECE)*, 72–76. https://doi.org/10.1109/YEF-ECE.2019.8740819 (cit. on p. 37).

Poduval, B., DeForest, C. E., Schmelz, J. T., & Pathak, S. (2013). POINT-SPREAD FUNCTIONS FOR THE EXTREME-ULTRAVIOLET CHANNELS OF<i>SDO</i>/AIA TELESCOPES. *The Astrophysical Journal*, *765*(2), 144. https://doi.org/10.1088/0004-637x/765/2/144 (cit. on p. 28).

Scheiner, C. (1630, January). *Rosa ursina sive sol ex admirando facularvm macularum suarum phaenomeno varius*. (Cit. on p. 5).

Schroeter, E. H. (1985). The Solar Differential Rotation - Present Status of Observations., *100*, 141. https://doi.org/10.1007/BF00158426 (cit. on p. 55).

Shahamatnia, E., Dorotovič, I., Ribeiro, R. C., & Fonseca, J. F. (2013). A PSO/Snake Hybrid Algorithm for Determining Differential Rotation of Coronal Bright Points. https://doi.org/10.5220/0004576100560063 (cit. on pp. 13, 18, 20).

Shahamatnia, E., & Ebadzadeh, M. M. (2011). Application of particle swarm optimization and snake model hybrid on medical imaging. https://doi.org/10.1109/cimi.2011.5952043 (cit. on p. 18).

Shahamatnia, E., Mora, A., Dorotoviăź, I., Ribeiro, R. A., & Fonseca, J. (2016, July). *Evaluative Study of PSO/Snake Hybrid Algorithm and Gradient Path Labeling for Calculating*

Solar Differential Rotation. Springer Science+Business Media. https://doi.org/10.1007/978-3-662-53525-7_2 (cit. on pp. 15, 18–20).

Skokić, I., Brajša, R., Roša, D., Hržina, D., & Wöhl, H. (2014). Validity of the relations between the synodic and sidereal rotation velocities of the sun. *Solar Physics*, *289*(5), 1471–1476. https://doi.org/10.1007/s11207-013-0426-1 (cit. on p. 34).

Solar Orbiter [Accessed: 12-05-2023]. (2023). https://www.esa.int/Science_Exploration/Space_Science/Solar_Orbiter (cit. on p. 8).

Sudar, D., Skokić, I., Brajša, R., & Saar, S. H. (2015). Steps towards a high precision solar rotation profile: Results from SDO/AIA coronal bright point data. *Astronomy and Astrophysics*, *575*, A63. https://doi.org/10.1051/0004-6361/201424929 (cit. on pp. 12, 14, 15, 33–35).

Sun diagram - Wikimedia Commons [Accessed: 05-05-2023]. (2008, October). https://commons.wikimedia.org/wiki/File:Sun_diagram.svg (cit. on p. 2).

SunPy. (2024). Sunpy. https://sunpy.org/ (cit. on pp. 25, 27, 34).

Thompson, M. M., Toomre, J., Anderson, E. W., Antia, H. M., Berthomieu, G., Burtonclay, D., Chitre, S. M., Christensen-Dalsgaard, J., Corbard, T., DeRosa, M. L., Genovese, C. R., Gough, D., Haber, D. A., Harvey, J. T., Hill, F., Howe, R. T., Korzennik, S. G., Kosovichev, A. G., Leibacher, J., . . . Wilson, P. (1996). Differential Rotation and Dynamics of the Solar Interior. *Science*, *272*(5266), 1300–1305. https://doi.org/10.1126/science.272.5266.1300 (cit. on p. 5).

Webb, D. J., & Howard, T. D. (2012). Coronal Mass Ejections: Observations. *Living Reviews in Solar Physics*, *9*. https://doi.org/10.12942/lrsp-2012-3 (cit. on p. 9).

Wojke, N., Bewley, A., & Paulus, D. (2017). Simple online and realtime tracking with a deep association metric. https://doi.org/10.1109/icip.2017.8296962 (cit. on p. 21).

2024 Use of computer vision and machine learning for the analysis of solar rotation profile: Francisco Figueira

NOVA SCHOOL OF SCIENCE & TECHNOLOGY